Università degli Studi di Ferrara

DOCTORAL COURSE IN PHYSICS

CYCLE **XXXIV**

Coordinator: Prof. Elenora Luppi

Development of a Personalized Dosimetry System for PRRT

Scientific/Disciplinary Sector (SDS) FIS/07

Candidate:

Dott. Longo Lorenzo

Tutor:

Prof. Gambaccini Mauro

Supervisor:

Prof. Di Domenico Giovanni

Dott. Turra Alessandro

Year 2018-2021

Abstract

This thesis focuses on the use of Monte Carlo codes in nuclear medicine for both imaging purpose and absorbed dose calculation with the aim of a personalized dosimetry evaluation for patients undergoing Peptide Receptor Radionuclide Therapy (PRRT).
The research project rises from a co-founding by the European Union and the Regione Emilia-Romagna and has been developed by the cooperation of the University of Ferrara with the Azienda Ospedaliera Universitaria of the Arcispedale S.Anna.

Traditional approaches to cancer therapy, such as conventional chemotherapy and external radiotherapy, consist in killing the cells that show uncontrolled growth. The non-specific targeting of cells implies that these treatments are often non-selective.
In the last years a growing emphasis has arisen on targeted therapies designed to damage only the cancerous cells bringing to the birth of several clinical trials. Among the various targeting treatments, Molecular RadioTherapy (MRT) exploits tumor-specific radiopharmaceuticals. MRT is a systemic treatment and uses molecules labeled with a radionuclide to deliver radiation to malignant tumors. In this therapy, a cell-targeting pharmaceutical is combined with a small amount of radioactive material and, when injected into the patient's blood, it binds to tumor cells and delivers a targeted dose. In particular, PRRT is a specific type of MRT in which the pharmaceutical vector for the radionuclide is a somatostatin analog peptide.

In order to monitor the efficacy of a cancer therapy in dealing damage to tumors while preserving healthy tissues, a procedure called *dosimetric evaluation* is required. This procedure consists in evaluating the absorbed dose imparted to the tissues of interest (tumors or organs) by the administered radiation.
For external radiation therapy, such as conventional radiotherapy, the dosimetric evaluation is relatively simple once the energy and intensity of the radiation delivered from the operator to the patient are determined.
In MRT, in order to perform a correct dosimetric evaluation the first problem is a precise measurement of the radionuclide activity in the sites of interest. In MRT the radiation sources are not localized,

but are distributed in the various organs and tissues involved both in the chemical processes and in the physiological pathway of the molecule that constitutes the radiopharmaceutical. Furthermore, the distribution of the radiopharmaceutical is not fixed over time, but varies according to the chemical and physiological processes typical of each patient. Thus, the radionuclide activity distribution assessment can not be performed directly but requires the quantification of functional images deriving from two-dimensional scintigraphies or three-dimensional tomographies. The morphological and functional data deriving from the quantification of the patient's images are then elaborated in order to obtain an estimate of the damage dealt to the patient's tissues of interest. Absorbed dose (Gy) is a first order approximation for the estimation of this damage and is the physical quantity to be determined in the dosimetric evaluation.
For the case of MRT, the dosimetric procedure is cumbersome and the physical quantities involved are ofter associated to high relative uncertainties. In this frame of work, Monte Carlo (MC) simulations can thus be a useful tool.

Monte Carlo techniques have become popular in different areas of medical physics with advantage of powerful computing systems. In particular, they have been extensively applied to simulate processes involving random behavior and to quantify physical parameters that are difficult or even impossible to calculate by experimental measurements. Recent nuclear medical imaging innovations, such as single-photon emission computed tomography (SPECT), are ideal for Monte Carlo modeling techniques because of the stochastic nature of radiation emission, transport and detection processes.
Similarly to the imaging process, the following dosimetric evaluation consists in procedures involving the stochastic nature of radiation interaction and a practical impossibility to perform a direct measure inside the patient's body. Factors which have contributed to the wider use of MC techniques in nuclear medicine include improved models of radiation transport processes, the practicality of application with the development of acceleration schemes and the improved speed of computers.

The Council Directive 2013/59/Euratom of the European Union fixes safety protection standards for avoiding dangers caused by exposure to ionizing radiation and fixes the need for individual and personalized dosimetry for patients treated with radionuclides. In this perspective, the need for a patient-tailored treatment and dosimetry arises: a correct activity estimation is the base for correct absorbed dose evaluation. In order to do so, it is necessary to develop a methodical capable of granting different steps, such as:

- Measurement of the administered activity;
- Quantitative SPECT or PET scans in order to determine the activity distribution inside the patient's body;

- Calculation of the absorbed dose to organs;
- Evaluation of the uncertainties.

The thesis will proceed along the forementioned path. The introductory chapters present the basics of Nuclear Medicine Physics and Radiobiology [Chapter 1], necessary to understand the use of radionuclides in tumor treatment. Since absorbed dose calculations require the knowledge of the radiopharmaceuticals' distribution inside the patient body, the theoretical and experimental elements of Nuclear Medicine imaging and the imaging reconstruction methods are presented in Chapter 2 and Chapter 3, respectively. Finally, the procedures and corrections for absolute activity quantification from the acquired images and the different approaches for the calculation of absorbed dose to organs and tumor lesions are introduced in Chapter 4 and Chapter 5.
After these introductory chapters, the original work will be presented in the successive part.

Chapter 6 shows a study for the validation of SIMIND Monte Carlo code to model a Siemens Symbia Intevo Excel SPECT-CT gamma camera for ^{99m}Tc and ^{177}Lu radioisotopes. Phantom experiments using ^{99m}Tc and ^{177}Lu have been performed with the purpose of measuring spatial resolution, sensitivity and to evaluate the calibration factor (CF) and recovery coefficients (RC) from acquired data. The experimental results have been compared with the results obtained from Monte Carlo simulations performed in the same geometries. The final aim of this first part of the work is to have a tool able to accurately simulate the activity distribution inside the patient body. This will be useful for future works in order to calculate the dose imparted to each organ from the reconstructed activity distribution and finally to compare the imparted dose with the dose calculated from the true distribution so as to implement patient-specific dosimetry.

A significant part of the PhD project was developed in cooperation with the U.O.C. Fisica Medica (Complex Operative Unit of Medical Physics). During the internship, the morphological and functional data of patients undergoing PRRT were used for the dosimetry evaluation exploiting the OLINDA/EXM software. Chapter 7 presents the workflow and the absorbed dose results of the FENET 2016, a phase II study routinely applied at University Hospital S. Anna (Ferrara, Italy). Treatment protocol relies on either five PRRT cycles with ^{177}Lu-DOTATOC (MONO) or a sequence of ^{177}Lu followed by 90Y-DOTATOC (DUO) spaced two months apart. Tumors and organ-at-risk (OAR) dosimetry were performed on patients treated with PRRT using a simplified but patient-tailored dosimetric approach.

Chapter 8 shows the results of absorbed dose calculation for 10 patients enrolled in the FENET 2016 study with the use of GATE Monte Carlo code. The code was validated by using the ICRP 110

standard male and female phantoms to calculate specific absorbed fractions (SAFs) for monoenergetic photons and electrons and S-values for ^{177}Lu. By using the validated code, absorbed dose to kidneys and tumors was then calculated using the SPECT and CT images of the patients.

Finally, in Chapter 9 the image data of the same 10 patients were used for the absorbed dose calculation to kidneys and tumors with the voxel S values method. For this purpose, two softwares were taken into account for the calculation: PLANET®Dose from DOSIsoft company and MIM SurePlan^{TM} MRT from MIM Software company.

Final aim of the work is the use of Monte Carlo codes for a dual objective. First, to have a tool able to simulate accurately the activity distribution inside the patient body. Second, to perform a precise dose evaluation on the patient using image-based calculations, that is by exploiting the acquired SPECT and CT images.

Contents

List of Figures

List of Tables

Chapter 1

Nuclear Medicine Physics and Radiobiology

Living organisms are continuously exposed to ionizing radiations both from natural sources and from human activities ([1], [2]).The former is due to cosmic rays, crust radionuclides, air, water and human body itself, whose amount represents a reference factor that can be compared with artifical activities. The latter are man-made sources: examples are medical purposes radiations, nuclear power reactors, or, also, nuclear weapons.

Ionizing radiation is divided into direct and indirect. Charged particles, with a certain kinetic energy, are the direct ionizing radiation: when interacting with the medium, they produce chemical and biological damage to cells and molecules. The passage of α, β particles, proton, neutrons and ions causes intense damage to molecules along the path.
On the other side, X and gamma rays are indirectly ionizing radiation: they don't cause directly a biological damage but produce secondary electrons, which are then capable of ionizing the medium atoms, by removing one or more electrons from atoms. Resulting electrons and positively charged ions are the cause for the subsequent significant biological effect in the irradiated material. Radiobiology is the study of the action of ionizing radiation on biological tissues, for reasearch purposes, radioprotection and radiotherapy.

In Molecular RadioTherapy (MRT), ionizing radiations deriving from the radiopharmaceuticals (cell-targeting peptides combined with radioactive material) are the source of the damage dealt to the patient's tissues. In this chapter, the biological properties of ionizing radiation and the main physical quantities used for their description are presented.

1.1 Biological properties of ionizing radiation

The interaction of ionizing radiation with biological tissues is a transversal field of study for several scientific branches such as radiology, radiotherapy, radioprotection and radiobiology. The series of physical, chemical and biological processes develops on a large temporal scale (see Figure 1.1) and starts with the physical interaction of the ionizing radiation with biological targets having dimensions in the range of the DNA's ($2nm$, see Figure 1.2).

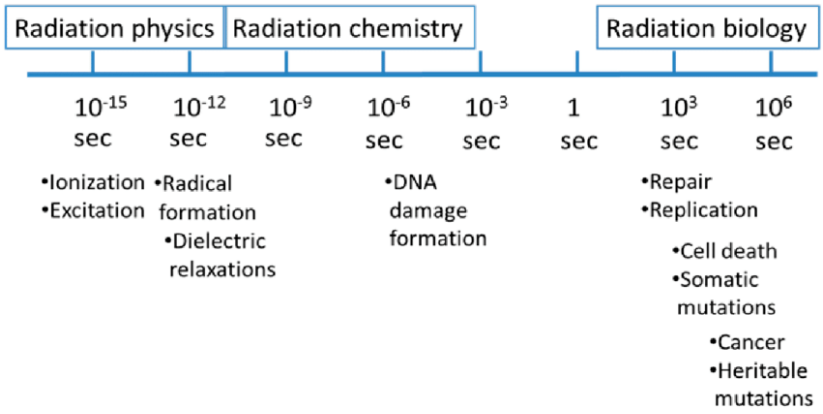

Figure 1.1: Time scales of major events that lead to biological effects of ionizing radiation. Above the scale bar are shown the corresponding research fields that investigate the events [[3]].

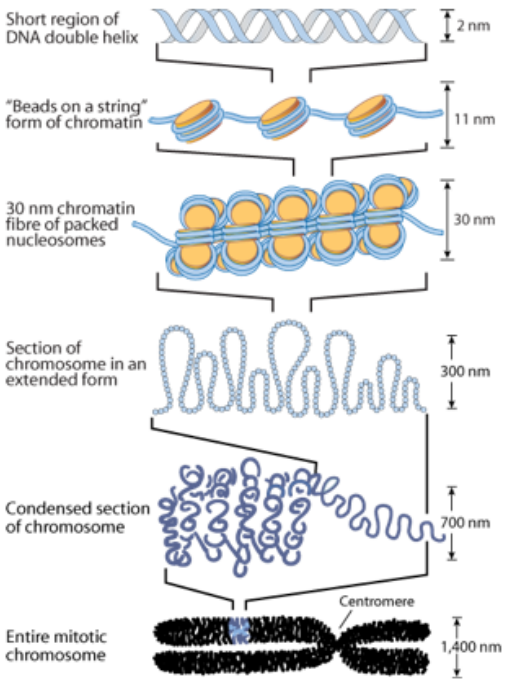

Figure 1.2: Sketch of typical dimensions of biological targets [[4]].

At a microscopical level, the impinging radiation interacts with the atoms of the medium via

excitation or ionization of the atomic electrons. If the impinging radiation has enough energy to extract an atomic electron, the radiation is called ionizing, and may launch a cascade of secondary electrons (δ rays). These are the responsibles for the biological damage induced by the primary radiation (α, β, γ) which instead determines the range in the tissue and the spatial distribution of δ production. As already mentioned, the radiations concerning nuclear medicine are γ, $\beta\pm$, α and δ. These interact with the medium via several processes, which determine the different biological efficacy when the target is a living tissue.

γ radiation interacts with the medium via photoelectric effect, Compton scattering or pair production. These are competing processes each having a probability p(E) dependent on the photon energy E of taking place. The events occurring through these interactions radically change the history of the photon. Since the characteristic energies of the photons exploited in nuclear medicine are in the range $10^1 - 10^2\, keV$, the processes of interest are the photoelectric effect and the Compton scatter. In Figure 1.3, a scheme of the relative probability for the photoelectric, Compton and pair production effects as a function of the medium Z number and the photon energy and the linear attenuation coefficient μ as a function of the energy for photons impinging on water.

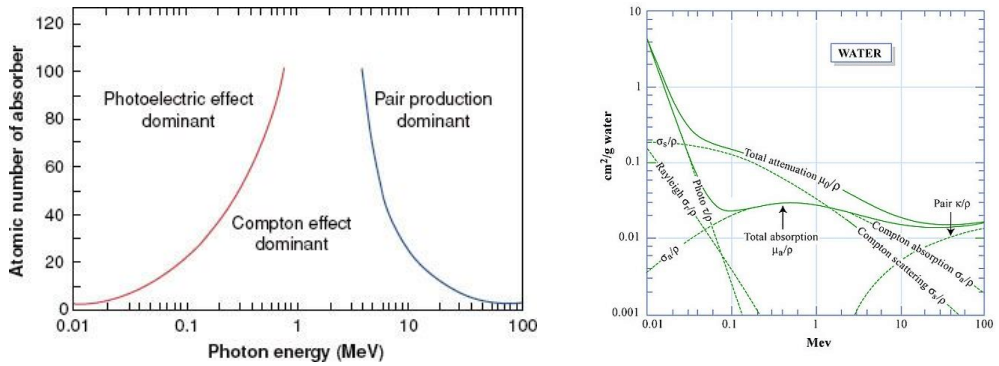

Figure 1.3: Scheme of the relative probability for the photoelectric, Compton and pair production effects as a function of the medium Z number and the photon energy (left) [[5]]. Plot of the linear attenuation coefficient μ as a function of the energy for photons impinging on water (right) [[6]].

These interactions can cause the excitation or the ionization of the atomic electrons. The electrons interact with the medium via electron-electron coulomb interactions or via deceleration radiation (Bremsstrahlung) when they pass close to the atomic nuclei. The average energy loss of the electron depends on the electron Energy and the atomic number of the medium, and the ratio between the two interactions' contributions is given by the relation:

$$\frac{\left(\frac{dE}{dx}\right)_b}{\left(\frac{dE}{dx}\right)_c} \cong \frac{E \cdot Z}{700} \tag{1.1}$$

Heavy ions, such as protons and alphas, interact with the medium continuously. The ion progressively loses energy through electromagnetic interaction with the atomic electrons and causes a cascade of ionization and excitation events. The high spatial density of these events allows them to induce a more incisive damage in the biological tissue, especially at the end of their path.

The radiation characteristic of being sparsely or densely ionizing is described in terms of the Linear Energy Transfer (LET), defined as:

$$LET = \frac{d\overline{E}}{dl} \tag{1.2}$$

where is the mean energy locally deposited from a particle of defined energy in a distance in the medium.

The damage induced from the radiation is either direct or indirect:

- Direct damage involves the excitation and ionization events in the biological target that may cause an observable damage over time and is prevalent for high LET radiations such as heavy ions;
- Indirect damage derives from the effects of the radiation on the atoms or molecules that are not part of the biological targets directly impinged by the radiation and is mainly due to creation of free radicals. Free radicals are atoms, molecules or ions that have an unpaired valence electron which, as a result of the ionization of the water molecules, may migrate and damage the target. This sort of damage is dominant for low LET radiations such as electrons and gammas.

For what concerns the direct damage, lesions to the DNA are one of the main causes of cellular death. Since the DNA is made of two strands, isolated damages to the DNA structure, also known as Single Strand Break (SSB), have a high probability of being repaired since the second strand is intact. On the contrary, Double Strand Breaks (DSB) are more difficult to be repaired and lead more easily to the cell death. Clustered damages, composed as multiple

DSB close to each other, have a higher probability of leading to the cell death. Figure 1.4 shows a scheme of the possible damages previously described.

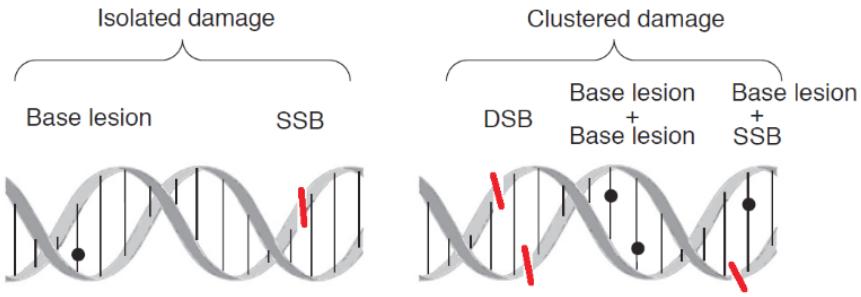

Figure 1.4: Sketch of the possible damages to the DNA [[7]].

Cells lethally hit by radiations can continue functioning after the damage has been inflicted and die only when trying to effectuate mitosis. Damages administered to the different body constituents manifest over a large temporal scale depending on the proliferation rate of the specific nature of the cell. Damages clinically observed as a consequence of the exposure to ionizing radiation are classified as early or acute damages and late damages. The first ones appear within some days or weeks after the irradiation and are associated to epithelial tissues characterized by a fast proliferation such as the bone marrow. The latter ones may appear after months or years after the exposure to radiations and appear in biological structures with a slow proliferation such as kidneys. In most radiotherapy applications the late damage effects are considered the most critical and are those that usually limit the total amount of dose to be imparted.

1.2 Basic quantities in radiation-matter interactions

Medical use of radiation accounts for 98% of the population dose contribution from all artificial sources, and represents 20% of the total population exposure. Annually worldwide, more than 3600 million diagnostic radiology examinations are performed, 37 million nuclear medicine procedures are carried out, and 7.5 million radiotherapy treatments are given (World Health Organization data). Since ionizing radiation induce damages to living tissue, it is fundamental to define the safety standards regarding the use of machineries that contemplate the emission of radiations. The principles of radioprotection based on the safety standards of the International Atomic Energy Agency (IAEA) are developed by the International Commission on

Radiobiological Protection (ICRP).

The effects of radiation exposure are grouped into two categories by the ICRP:

- Deterministic Effects: effects that only appear at relatively high doses. No deterministic effects would be expected below an absorbed dose of 100 mGy (above the natural background exposure), and thresholds for most effects are much higher. Because of this, deterministic effects are rare, although they can occur as a result of sophisticated medical procedures, or accidents. In extremely rare cases, such as in severe accidents, very high doses received in a very short time can lead to acute radiation syndrome and even death;

- Stochastic Effects: effects that are assumed to pose some risk even at low doses. There is reliable scientific evidence that doses above 100 mSv can increase the risk of cancer. Below this dose the evidence is less clear, but for purposes of radiological protection it is assumed that even small doses might result in small increased risk.

In this work, where radiation is exploited in order to assess damage to tumors, the focus is on the deterministic effects of radiation.

The fundamental physical quantities of radioprotection are the dosimetric quantities that describe qualitatively and quantitatively the entity of the possible biological damage as a consequence of the exposure to radiation [[9], [10]]. The basic quantity is the average Dose D absorbed by a site of mass m crossed by a radiation that deposits an amount E of energy, and is defined as [[10]]:

$$D = \frac{E}{m} \tag{1.3}$$

and measured in the International System of Units with gray ($1Gy = \frac{J}{Kg}$).
Figure 1.5 shows the relative dose for different radiations as a function of the radiations' range in water.

A simple information of the average energy deposited per mass unit, though, is not sufficient for the description of the induced biological damage. Other quantities are defined to describe the biological efficacy of the deposed energy as a function of the different radiations and the involved tissue.

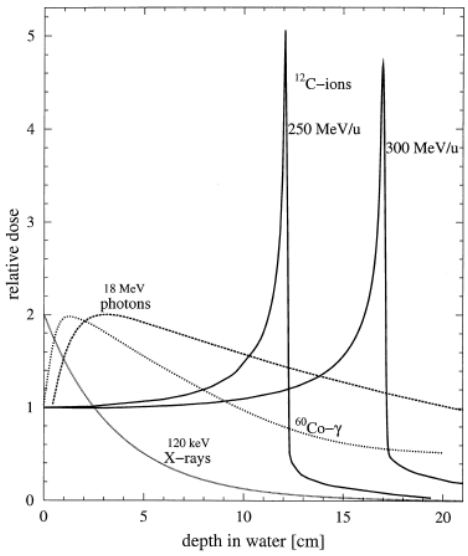

Figure 1.5: Relative dose of the different radiation types as a function of the range in water [[8]].

Weight coefficients w_R are introduced in order to account for the higher probability of a densely ionizing radiation to induce irreversible damages to the subcellular structures. When w_R coefficients are multiplied for the average Dose one obtains the Equivalent Dose [[10]]:

$$H = w_R \cdot D_R \tag{1.4}$$

that is measured in the International System of Units with the sievert (Sv). The weight coefficient is $w_R = 1$ for X rays, gammas and electrons and $w_R = 20$ for α particles.

The relation between the probability of a stochastic effect outbreak and the Equivalent Dose depends on the irradiated organ or tissue. To consider for this relation, weight factors w_T that represent the contribution of the tissue T to the total damage induced from a total body irradiation. The dosimetric quantity resulting is the Effective Dose E, defined as [[10]]:

$$\begin{aligned} E &= \sum_T w_T \cdot H_T \\ \sum_T w_T &= 1 \end{aligned} \tag{1.5}$$

where H_T is the Equivalent Dose in the tissue T.

When a radionuclide is administered to the patient, the resulting Dose is delivered over the total residence time in the patient. The cumulative imparted Dose is calculated as the

integral:

$$H_T(\tau) = \int_{t_0}^{t_0+\tau} \cdot \overline{H}_T(t)dt \tag{1.6}$$

where t_0 is the administration time and τ is the total integration time.

The ICRP recommends a radiological protection system that covers all the possible exposures and divides them in three types: programmed exposures, emergency exposures (such as those caused by a nuclear accident) and exposures to natural sources of radiations called existing exposures. The use of radiations in nuclear medicine is a programmed exposure circumstance, thus requires to be monitored and a proper authorization.

ICRP divides individual exposure in three categories:

- medical exposure, concerning the exposure to patients as a consequence of diagnosis or treatment;
- working exposure, concerning subjects in charge of the manipulation and administration of radiation sources;
- public exposure.

All three these categories of individual exposure are contemplated in a nuclear medicine center.

ICRP has three fundamental principles for the radiological protection:

- the justification principle: each decision that modifies the exposure to radiation has to cause a benefit higher than the damage;
- the principle of the protection optimization: the possibility of incurring exposition, the number of involved people and the individual dose have to be maintained the lowest as possible (ALARA principle: As Low As Reasonably Achievable);
- the principle of the dose limitation: the total imparted Dose

1.3 Cellular Response to Radiation

Following radiation exposure, cellular response may vary depending on several biological variables, such as cell type, oxygen tension and cell cycle at time of exposure, as well as physical factors related to the impinging radiation, such as dose, dose rate and LET. Potential responses could be delayed cell division, apoptosis, reproductive failure, genomic instability (delay expression of radiation damage), DNA mutations, phenotypic (including potentially oncogenic) transformations, bystander effects (damage to neighboring unirradiated cells), and adaptive responses (irradiated cells become more radioresistant). Among these effects, the study of radiation-induced reproductive failure (also referred to as clonogenic cell death or loss of reproductive integrity) is particularly useful in assessing the relative biologic impact of various types of radiation and exposure conditions.

The most direct method of evaluating the ability of a single cell to proliferate is to wait until enough cell divisions have occurred to form a visible colony. Counting the number of colonies that arise from a known number of individual cells irradiated in vitro and cultured provides a way to easily determine the relative radiosensitivity of particular cell lines, the effectiveness of different types of radiation, or the effect of various environmental conditions. The loss of the ability to form colonies as a function of radiation exposure can be described by cell survival curves.

As shown in Figure 1.6, Survival curves are usually presented with the radiation dose plotted on a linear scale on the x-axis and the surviving fraction (SF) of cells plotted on a logarithmic scale on the y-axis. In the case of low-LET radiation, the survival curve is characterized by an initial "shoulder" before the linear portion of the semilogarithmic plot. The presence of the shoulder in a cell survival curve is taken to indicate that more than one ionizing event "hit", on average, is required to kill a cell and the reappearance of the shoulder when a large dose is delivered in fractions indicates that the cells are capable of repairing sublethal damage between fractions.

Cell survival curves are described with the linear quadratic (LQ), and the SF is expressed as:

$$SF(D) = e^{-\alpha D + \beta D^2} \tag{1.7}$$

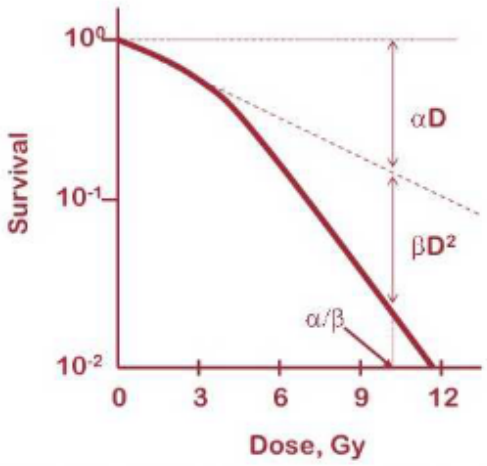

Figure 1.6: The curve reflects radiosensitivity of cells; it is defined as survival curve [adapted from [11]].

where D is the dose in Gy, α is the coefficient of cell killing that is proportional to dose (i.e., the initial linear component on a log-linear plot) and β is the coefficient of cell killing that is proportional to the square of the dose (i.e., the quadratic component of the survival curve). The two constants α and β can be determined for specific tissues and cancers to predict dose response, and they represent the damage caused by individual radiation particle and the probability of cell death after more than two temporally separated hits, respectively. Increasing the β value, that means increasing the plot curvature, shows how important the time interval between two hits is since cellular repair may happen. Thus, increasing the quadratic component in the exponential of the LQ model means both increasing the dose rate but also letting a tissue repair, to tumor cells disadvantage. Indeed, tumor cells have a worse efficient repair mechanism, despite being classified as early responding tissues as other normal tissues.

Early and late responding tissues are defined by the α/β ratio. It is the dose at which cell survival fraction is equal for both components. In general, early responding tissues (like skin, bone marrow) and tumors have a high α/β (8 to 12 Gy), although tumor's ratio spreads from 5 to 25 Gy; while late responding tissues (like lung or spinal cord) have lower value of α/β ratio (3 to 4 Gy). This difference in the tissues leads also to the previously explained early and late observable effects. Furthermore, the linear damage predominates at lower α/β ratios, while quadratic damage al higher α/β ratios.

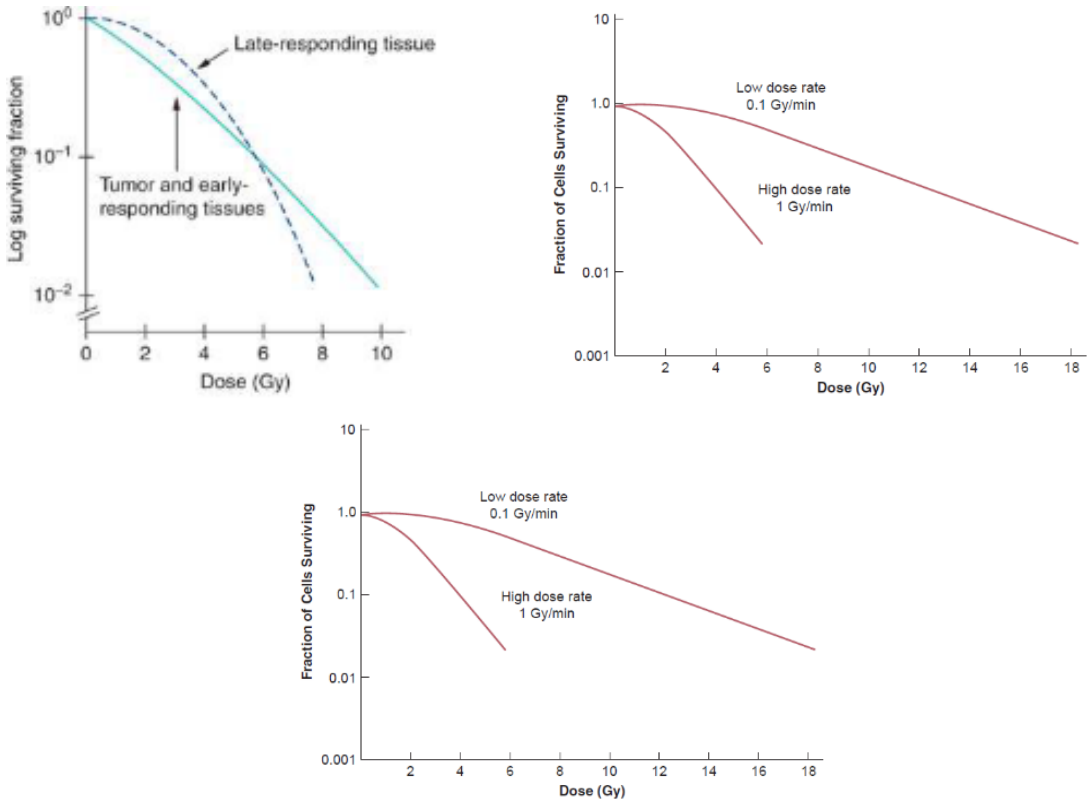

Figure 1.7: In (a), in a Log survival fraction- Dose graph, early and tumor responding tissue versus late responding tissues [[22]]. In (b) comparison between low LET and high LET. It's clear the difference in the dose need to cause the same cell damage [[2]]. In (c) Low dose rate versus high dose rate. [[22]]

1.3.1 Molecular RadioTherapy and Radiopharmaceuticals

Conventional radiotherapy consists in the irradiation of a specified and limited target volume with photons or electrons. This is achieved, though, at the cost of damaging the external tissue in correspondence of the inner tumor lesion: radiation beams are not target-specific, and the damage follows the energy deposition given by the stopping power curve.

In contrast, Molecular RadioTherapy (MRT) results in a whole-body dose: the radiopharmaceutical is injected into the patient's body, and it can be carried to different organs other than the tumor lesion, in particular to the kidneys, the liver and the bone marrow. Radiopharmaceuticals have a high variability in terms of pharmacokinetics and biodistribution, but they are altered when the radionuclide is conjugated with a targeting molecule. Pharmacokinetics may be defined as the study of the dynamic movements of foreign chemicals (xenobiotics) during their passage through the body, including the kinetics of absorption, distribution, metabolism and excretion (ADME) [[12]]. Pharmacokinetics uses mathematical models to

describe the time course of ADME of xenobiotics in the body enabling us to better understand, interpret and even predict the nature and the extent of the biological effects (therapeutic or toxic) of xenobiotics.
Studying a new radiopharmaceutical means performing study on its distribution in the body, to avoid its concentration in potentially sensitive tissues and to improve the affinity with the tumor lesions' receptors.

The choice of the radionuclide is crucial for MRT, and it has to meet several factors. The emitted particle range in biological tissue needs to be limited to localize the damage at best. The half life needs to be long enough to allow the radiopharmaceutical to arrive at the desired site, thus avoiding most of the nuclear decays to take place right after the injection, and it needs to be short enough to limit the patients' radioactivity over time, thus preventing undesired damages to the patient and to other people.
For what concerns the radioisotopes interested in the treatments, ^{177}Lu is an attractive radionuclide for several reasons: the possibility of labelling of biomolecules (used for tumor targeting), its favorable decay characteristics, its concentrated energy deposition, low energy beta emissions, its half-life and its two main gamma rays emitted (whose energies lead to imaging). Its characteristics are listed inTable 1.1 and its decay scheme is shown in Figure 1.8.

Table 1.1: ^{177}Lu decay characteristics [[13]]

Isotope	Half-life	Main γ emission $E_\gamma[keV](I_\gamma[\%])$	Max β energy $E_{max}[keV]$
^{177} Lu	6.65 d	112.9 (6.2) 208.4 (10.4)	498.3

As well as the radionuclides, the pharmaceutical used in MRT is crucial, and its choice depends on the tumor to be treated. Neuroendocrine tumors (NETs) are relatively rare and heterogeneous tumor type arising from the diffuse neuroendocrine system [[15], [16]], whose incidence has increased in the last years also thanks to the improvement of diagnostic techniques and to the deep knowledge of the pathology [[17], [18], [19]]. Peptide Receptor Radionuclide Therapy (PRRT), introduced more than 20 years ago, represents an important option approach that have expanded considerably. Since the majority of NETs show an abundance of the somatostatin receptors, PRRT uses radiolabeled somatostatin analogues to target the somatostatin receptors on neuroendocrine tumor cell surfaces [[20]]. Recent advances in

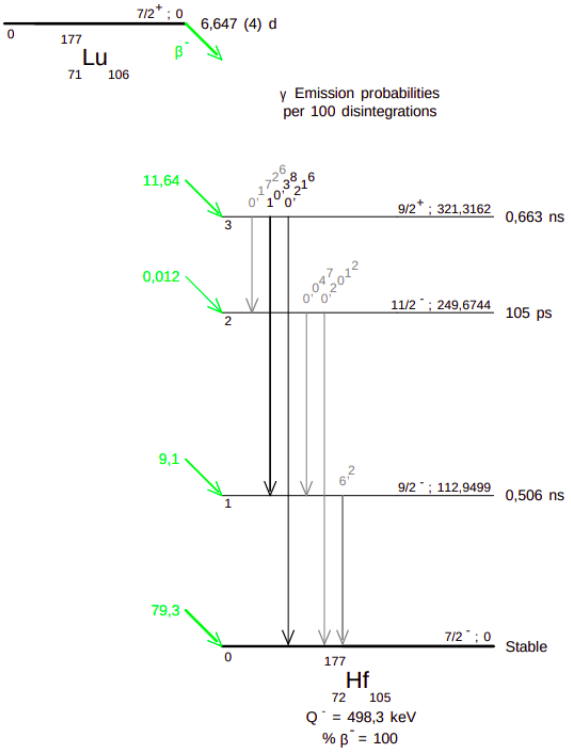

Figure 1.8: ^{177}Lu decay scheme [[14]].

MRT have led to a new somatostatin analogue, the DOTA-DPhe1-Tyr3 - octreotide, better known as DOTATOC, which has shown to have high affinity for somatostatin receptors.

1.4 Conclusions

This brief and simplified description of the different radiations and their effect on biological matter is a necessary introduction for the work.

As discussed, the more complex the damage, the more difficult will be for the cell to repair it. Thus, in order to assess a critical damage to tumor tissues, the objective will be that of imparting the more damage as possible to the tumor cells. Since MRT is a systemic treatment, though, one can not control where the radionuclides will deposit but by conveying them with pharmaceuticals that will more likely bond to tumor cells.

In MRT, ionizing radiations deriving from the radiopharmaceuticals are the source of the damage dealt to the patient's tissues and the damage they assess to both the tumors and the healthy tissues is the quantity to be monitored during the treatment. The dosimetric procedure to evaluate this damage is, though, a cumbersome process.

As mentioned in the abstract, in order to perform a dosimetric evaluation on the tissues of interest after the radiopharmaceutical administration, the first and necessary step is the acquisition of morphological and functional data of the patient via scintigraphic or tomographic imaging. In the next chapter, the fundamentals of the imaging method adopted in this work (i.e. three-dimensional tomographic imaging, SPECT and CT) are presented.

Chapter 2

Nuclear Medicine Imaging

In this chapter, the imaging instruments exploited for the determination of morphological and functional data of the patient after the radiopharmaceutical administration are presented. Specifically, single photon emission computed tomography (SPECT) and computed tomography (CT) are the instruments investigated in this part.

In SPECT, a nuclear camera records x- or gamma-ray emissions from the patient from a series of different angles around the patient. These projection data are used to reconstruct a series of tomographic emission images. SPECT images provide diagnostic functional information, and their tomographic nature allows to better understand the precise distribution of the radioactive agent.
CT is the first medical imaging modality made possible by the computer. CT images are produced by passing x-rays through the body at a large number of angles, by rotating the x-ray tube around the body. A detector array, opposite the x-ray source, collects the transmission projection data. The numerous data points collected in this manner are synthesized by a computer into tomographic images of the patient. CT is a transmission technique that results in images of individual slabs of tissue in the patient.

Gamma cameras, or Anger gamma scintillation camera, was developed by Hal O. Anger at the Donner Laboratory in Berkeley, California, in the 1950s [[21]] are the instruments exploited to perform SPECT studies. They consist of one or more flat crystal planes (or detectors) optically coupled to an array of photomultiplier tubes in an assembly known as a "head", mounted on a gantry. The gantry is connected to a computer system that both

controls the operation of the camera and acquires and stores images. Today's gamma cameras offer the advantage to couple SPECT and CT systems in one single device.

Because charged particles from radioactivity in a patient are almost entirely absorbed within the patient, nuclear imaging uses gamma rays, characteristic x-rays (usually from radionuclides that decay by electron capture), or annihilation photons (from positron-emitting radionuclides) to form images. Specifically, SPECT images in MRT are performed in order to locate and, later, quantify the injected radionuclide inside the patient and are produced by exploiting the gamma rays emitted in the radionuclide decay (for ^{177}Lu in PRRT being the two main gamma peaks at 113 keV and 208 keV, see Section 1.3.1). CT images are needed in order to obtain morphological informations about the tissues of interest, meaning volume and mass of the tumor or the organs, their density etc.

2.1 SPECT

Positron Emission Tomography (PET) and Single Emission Computed Tomography (SPECT) are the main methods to perform both qualitative and quantitative imaging of radionuclides in nuclear medicine. The purpose of qualitative imaging is to locate the biological sites characterized by a high affinity to the injected vector molecule. The purpose of quantitative imaging is the assessment of the amount of activity located in the patient. Here since we will focus only on SPECT, which is the imaging technique studied in this work.

SPECT generates images reproducing the distribution of X- or γ-ray emitting nuclides in patients, thus obtaining a functional image. Computed tomography requires the acquisition of a set of images from at least a 180-degree arc about the patient. These image information is then mathematically processed by a computer to form images depicting cross sections of the patient.

Standard planar images are acquired from an arc of 180 degrees (most cardiac SPECT) or 360 degrees (most noncardiac SPECT) about the patient. Although these images could be obtained by any collimated imaging device, the vast majority of SPECT systems use one or more scintillation camera heads that revolve about the patient. The SPECT system's digital

computer then reconstructs the transverse images using a specific reconstruction method.

2.1.1 Image Acquisition

The camera head or heads of a SPECT system revolve about the patient, acquiring projection images. The head or heads may acquire the images while moving (continuous acquisition) or may stop at predefined evenly spaced angles to acquire the images ("step and shoot" acquisition). If the camera heads of a SPECT system produced ideal projection images (i.e., no attenuation by the patient and no degradation of spatial resolution with distance from the camera), projection images from opposite sides of the patient would be mirror images and projection images over a 180-degree arc would be sufficient for transverse image reconstruction. However, in SPECT, attenuation greatly reduces the number of photons from activity in the half of the patient opposite the camera head and this information is greatly blurred by the distance from the collimator. Therefore, for most noncardiac studies, such as bone SPECT, the projection images are acquired over a complete revolution (360 degrees) about the patient.

The camera heads on older SPECT systems followed circular orbits around the patient while acquiring images. Circular orbits are satisfactory for SPECT imaging of the brain but cause a loss of spatial resolution in body imaging because the circular orbit causes the camera head to be many centimeters away from the surface of the body during the anterior and perhaps the posterior portions of its orbit (Fig. 19-3). Modern SPECT systems provide noncircular orbits (also called "body contouring") that keep the camera heads in close proximity to the surface of the body throughout the orbit. For some systems, the technologist specifies the noncircular orbit by placing the camera head as close as possible to the patient at several angles, from which the camera's computer determines the orbit. Other systems perform automatic body contouring, using sensors on the camera heads to determine their proximity to the patient at each angle.

The gamma camera head is composed of several parts and is represented in Figure 2.1. Following the path of the gamma rays coming out of the patient body, the first component is the collimator that consists in a metallic or alloy plate with some holes. The next component is the NaI(Tl) crystal, that is coupled to the photomultipliers (PMTs) by a light guide. The

signal resulting from the PMTs is then amplified and analyzed by the position logic circuits which allow the reconstruction of the event position.

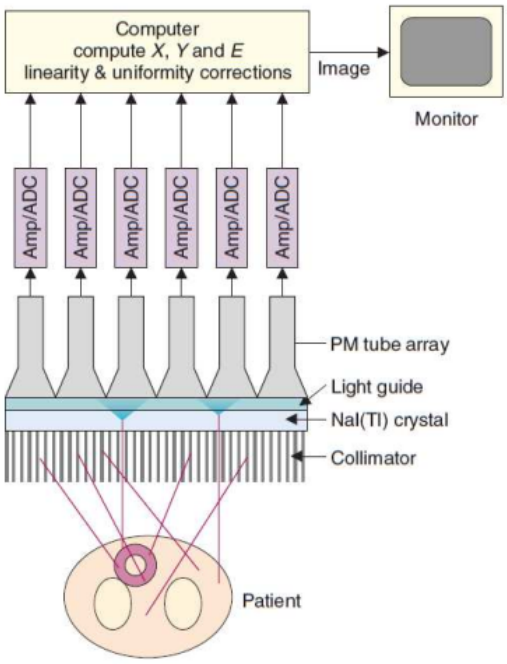

Figure 2.1: Scheme of a gamma-camera head with its main components [[22]].

Single events are defined with their energy by summing all the signals coming from the PMTs. If the final amplitude is within the set energy windows, the signal is accepted and contributes to the image formation. The image is a histogram of the number of events collected for each X and Y position.

2.1.2 Detector system and electronics

The NaI(Tl) crystal is one of the main components of the gamma camera. It is commonly from 6 mm to 12.5 mm thick and is surrounded by a thin aluminum case, except for the side in contact with the PMTs, that has the function of hermetically sealing the crystal.

PMTs are commonly rectangular parallelepipeds with circular or hexagonal shaped bases, and in order to cover the entire area of the crystal 30 to 100 PMTs are generally used. Between the detector crystal and PMTs a light guide may be placed to increase light collection efficiency and uniformity, and all these components are enclosed in a light lead housing.

The electronic component chains, consisting of the preamplifiers, the pulse-height analyzer and the ADCs, are placed directly on the PMTs' bases so as to reduce signal distortions as much as possible.

Event localization is improved by the introduction of a signal threshold. This is useful for two reasons: firstly, it is necessary to remove the noise produced by PMTs with a too low signal. Secondly, it makes so that only a reduced number of PMTs are involved in the position determination of a specific event, so that multiple events can be simultaneously detected thus improving the count rate performance of the camera.

2.1.3 Collimator

The collimator is another fundamental component of the gamma camera. In fact, in order to obtain an image of the radioactive source distribution a selection of the γ-rays impinging on the crystal is necessary.

Collimators are pierced metallic slabs and operate as absorbers: only photons impinging on the detector surface from a certain direction can overcome the collimator and reach the crystal. Photons coming from different directions are absorbed from the collimator septa, provided that the energy is small enough that the γ is fully stopped.

Collimators are distinguished for the holes' type and shape and for the energy range they are used for. Based on hole types, collimators are divided into parallel holes, pinholes, diverging and converging holes and are represented in Figure 2.2. Parallel holes collimators are the most commonly used and they project the impinging γ-rays into images of the same size as the source distributions'. In this work only parallel holes collimators have been used, and a picture is shown in Figure 2.3.

Collimators are classified on the base of the energy range they are employed for, specifically on the maximum γ-ray energy for which the septa thickness is adequate. This leads to a classification into Low Energy (LE), Medium Energy (ME) and High Energy (HE) collimators.

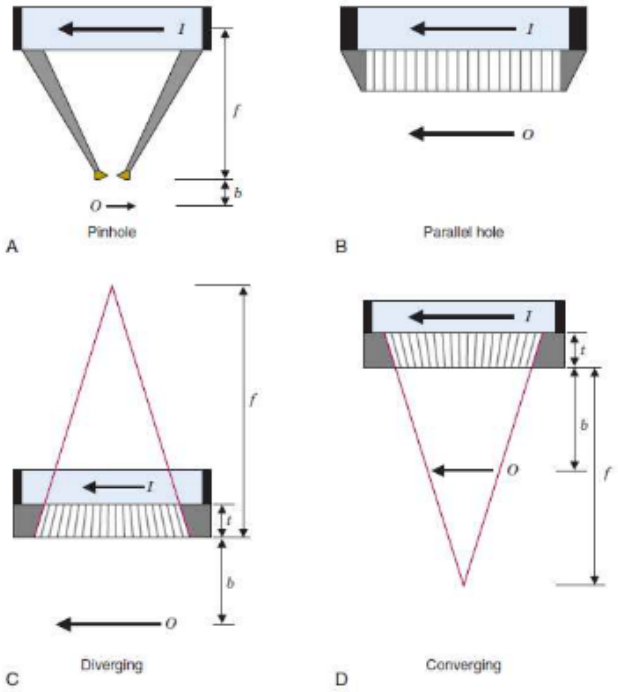

Figure 2.2: Pinhole, parallel hole, diverging and converging collimators [[22]].

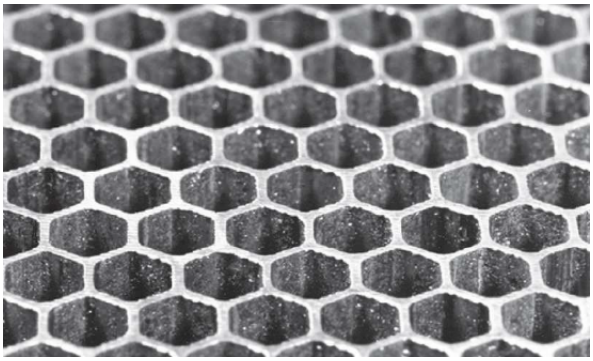

Figure 2.3: Hexagonal based parallel hole collimator [[22]].

As we mentioned, the choice of the collimator depends on the main γ-ray energy of the source we want to investigate; specifically, in this work the sources used are the ^{99m}Tc and the ^{177}Lu. For the former, whose main γ peak has a 140.5 keV energy, a Low Energy collimator was used. For the latter, whose β^- decay has a Q-value of 498.3 keV leading to a main 208 keV peak and a secondary 113 keV peak, a Medium Energy collimator was used.

Septal thickness and holes' length are calibrated depending on the energy range the collimator is used for. Larger septa and longer holes lead to an improve of the image quality, but also to a considerable reduction in the detector efficiency since they increase the detector's area

obstruction. Septal thickness can be defined as:

$$t \approx \frac{2dw}{l-w} \tag{2.1}$$

where w is the minimum path length for a photon crossing the septa, l is the hole length and d its diameter (see Figure 2.4). The maximum septal penetration allowed in order to achieve an acceptable image quality is about 5% [ref. S. R. Cherry, J. A. Sorenson, M. E. Phelps, Physics in nuclear medicine, Elsevier Health Sciences, 2012]. Since the aim is to achieve minimal septal penetration with a minimal detector area obstruction, materials with a high linear attenuation coefficient μ, meaning with a high Z and density values, are preferred. Typically, collimators are made of lead ($Z = 74$, $\rho = 19.3\frac{g}{cm^3}$) since it fits the required characteristics together with a low cost and high availability.

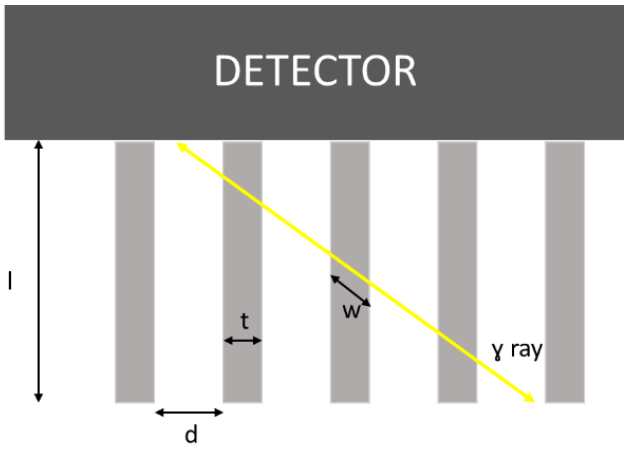

Figure 2.4: Detector, collimator with details of holes and septa.

Collimators' resolution and efficiency are the main features to evaluate their performance when coupled to a definite radioactive source.

Collimator resolution is defined as the full width at half maximum (FWHM) of the radiation profile from a point- or line-like source of radiation projected onto the detector, profile that is also called point- or line-spread function (PSF or LSF, respectively). The profile drawn perpendicular to the image detail used for the evaluation ([[25]]).
An estimation of collimator resolution could be done by the formula:

$$R_{coll} \approx \frac{d}{l_{eff}} \cdot (l_{eff} + z) \tag{2.2}$$

where z is the distance from the radiation source to the collimator, d is the hole diameter

and $l_{eff} = l - 2\mu^{-1}$ is the effective length of the collimator holes. As one can see from the formula, the collimator resolution strongly depends on the source-to-collimator distance.

Collimator efficiency g is defined as the fraction of photons passing through the collimator per photon emitted by the source towards the collimator, and is given by the formula:

$$g \approx K^2 \left(\frac{d}{l_{eff}}\right)^2 \frac{d^2}{(d+t)^2} \tag{2.3}$$

where t is the septal thickness and K is a constant that depends on the holes' shape. Because of the dependence of R_{coll} and g on $\frac{d}{l_{eff}}$ and $\left(\frac{d}{l_{eff}}\right)^2$ respectively, one can write that:

$$g \propto R_{coll}^2 \tag{2.4}$$

Since R_{coll} is defined as the FWHM of the radiation profile, meaning that the smaller R_{coll} the better the resolution, given a certain septal thickness the collimator resolution can be increased at the expense of decreasing the collimator efficiency and vice versa.

Moreover, one can see from Equations 2.2 and 2.3 that while the collimator resolution defined as the FWHM of the PSF increases with the increasing distance from the source to the collimator, meaning it becomes poorer, the collimator efficiency is not dependent on the source-to-collimator distance. In fact, given one is considering the whole detector area, this can be explained with the inverse-square law ruling the radiation transmitted to a single collimator hole together with the increasing number of collimator holes involved in the detection. This results in the fact that the total counting rate, and thus the collimator efficiency, does not change with the source-to-collimator distance.

Given the previous definitions and relations, we can state some further differences between the previously mentioned LE, ME and HE collimators. In particular they can also be divided into High Resolution (HR) having a good resolution but a bad efficiency, High Sensitivity (HS) having a good efficiency but a bad resolution, Low Penetration (LP) and General Purpose (GP) having intermediate characteristics.

In particular, the ^{99m}Tc detection was performed with a LEHR collimator while the ^{177}Lu with a MELP collimator. The characteristics of the two collimators exploited are listed in Table 2.1 .

Table 2.1: Main characteristics of the LEHR and MELP collimator exploited for measurements and Monte Carlo simulations.

Collimator	Hole diameter (cm)	Hole septa (cm)	Hole length (cm)	Hole shape	System resolution	Septal penetration
LEHR	0.111	0.016	2.405	Hexagonal	7.5 mm	1.5%
MELP	0.390	0.114	4.096	Hexagonal	12.5 mm	1.2 %

2.1.4 Event detection

Photons impinging on the detector surface after crossing a parallel hole collimator can lead to different type of events, that can be classified into four categories as illustrated in Figure 2.5.

Valid events are labelled with A on the figure. They occur when the γ ray is emitted parallel to the collimator holes, thus passing through a hole and interacting with the NaI(Tl) crystal by depositing all of its energy at a single location.

Detector scatter events are labelled with B on the figure. They take place when the γ ray is emitted parallel to the collimator holes, passes through a hole and interacts with the NaI(Tl) crystal via Compton scattering. The scattered γ ray may then interact again with the crystal and deposit its full energy in the detector (as illustrated in figure), or it may escape the detector thus depositing only a fraction of its total energy. In the former case the event cannot be rejected because of energy discrimination, and it will be misplaced. In the latter case it is likely that the event will be rejected since the deposit energy will probably be outside of the windows set for the energy discrimination.

Object scatter events are labelled with C on the figure. They happen when the γ ray is not emitted towards the gamma camera head but it is scattered by the patient's body and then passes through a collimator hole. The event is then detected but with a smaller energy than its original one, thus producing a signal that may be either accepted or rejected by the

detector because of energy discrimination. Accepted signals, occurring when the energy loss is small due to a small scatter angle (≤ 45 degrees), lead to a significant spatial mispositioning of the event. This generates a low-spatial-frequency background causing a loss of contrast. Similar effects may also be induced from scatter events with the collimator.

Septal penetration events are labelled with D on the figure. In this case the γ ray is emitted towards the detector but not parallel to the collimator hole. Because of incomplete attenuation by the holes' septa, the γ ray may reach the NaI(Tl) crystal and release a detectable signal. These events lead to a blurring of the image since all the photons reaching the detector after a parallel hole collimator are considered to have come from a direction perpendicular to the gamma camera head. This effect becomes more important when using high-energy γ emitters and/or high-resolution collimators with thin septa.

In addition to these four event categories, combinations of them can occur. Gamma camera heads and collimators for specific energy ranges are designed in order to reduce as much as possible the detection of events B, C and D.

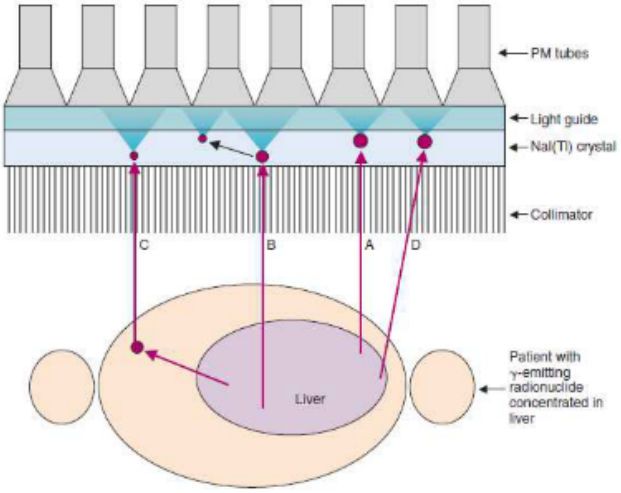

Figure 2.5: Different events occurring on a gamma camera detector. From Physics in Nuclear Medicine [[23]].

2.2 X-ray CT

X-ray CT is a transmission computed tomography, whose main component is the X-rays tube. This instrument, that produces bremsstrahlung radiation and characteristic X-rays in a

vacuum tube, has fundamental constituents the anode, the cathode the rotor/stator and a glass or metal casing.

A substantial potential difference going from 20 kV to 150 kV is applied between the heated cathode and the anode. The electrons generated via thermionic effect and accelerated by the potential difference interact with the anodic terminal and produce bremsstrahlung and characteristic X-rays. Varying the anode material, the applied current and potential difference and the additional filter, the energy spectrum of the radiation emitted from the tube may be modified. This variation allows to reach the best compromise between a good image quality and the least imparted dose to the patient during irradiation.

Traditional radiography is a two-dimensional representation of a three-dimensional object implying a superposition of data from the body structures. This fact is overcomed by Computed Tomography (CT) that allows a three-dimensional reconstruction by acquiring a large number of views around the patient. The process of CT image acquisition involves the measurement of the transmission profiles through the patient while rotating the X-ray tube and the detector around the patient. As a result, the voxels in the reconstructed three-dimensional CT image have a value corresponding to the linear attenuation value μ of the biological tissue.

The formula that describes the photon attenuation in the material is:

$$I(x) = I_0 \dot{e}^{-\mu x} \tag{2.5}$$

where x is the thickness of the crossed material, I_0 is the initial intensity of the beam and $I(x)$ is the final intensity after the bremsstrahlung and characteristic X photons have passed through the material. Since the beam passes through different materials, the beam impinging the detector after it passed through the material can be written as:

$$I(x) = I_0 \dot{e}^{-\sum_i -\mu_i \Delta x} \tag{2.6}$$

The summation can be written as integral:

$$\log \frac{I_0}{I} = \int \mu(x) dx \tag{2.7}$$

2.3 Siemens Symbia Intevo

The gamma camera used for the measurements and whose characteristics were reproduced for the Monte Carlo simulations is a Siemens Symbia Intevo Excel. The machine is a SPECT/CT system and was provided by Arcispedale di Cona (FE, Italy). A picture of the gamma camera is presented in Figure 2.6

Symbia Intevo Excel is equipped with two heads that acquire 2D projection images. Having two heads makes it possible to reduce the acquisition time by half, thus significantly shortening the exam duration. Symbia Intevo Excel acquires images for 180 degrees around the patient with two different modalities: either through a circular orbit, where the patient-to-detector distance is chosen by the operator, or through a non-circular orbit, also known as Body Contour modality. The latter technique provides a better resolution since the camera head can be closer to the patient thanks to an initial scout scan that determines the patient's contour as a function of the angle. SPECT and CT images are acquired sequentially with the so called "step-and-shoot" technique. The main characteristics of the exploited system are listed in Table 2.2.

Figure 2.6: A picture of Siemens Symbia Intevo SPECT/CT from https://www.healthcare.siemens.com/molecular-imaging/xspect/symbiaintevoexcel [[24]].

2.4 Performances and limitations

The gamma camera has finite performances in detecting photons. This leads to some errors in the reproduction of the radionuclide distribution inside the patient body. In the following

Table 2.2: Main characteristics of the Siemens Symbia Intevo SPECT/CT

FOV	53.3×38.7
Crystal size	59.1×44.5
Crystal thickness	$9.5\,mm$
PMT total number	59
PMT array	Hexagonal
System resolution at $10\,cm$, $140\,keV$	$7.5\,mm$
Energy resolution at $140\,keV$	9.9%
Sensitivity at $10\,cm$, $140\,keV$	$202\,cpm/\mu Ci$
SPECT reconstruction matrix	128×128
Tube current	$30 - 240\,mAs$
Tube voltage	80, 110, $130\,keV$
Focal spot size	$0.08 \times 0.7\,mm$
Number of detector elements	1344

paragraphs, the main limitations to the gamma camera performances are listed and briefly described.

2.4.1 Detection Efficiency

The detection efficiency is the detector ability of converting the gamma rays emitted from the source into a detectable signal. The maximization of the detection efficiency leads to the maximization of the count rate, meaning a minimization in the loss of information about the activity distribution.

The system efficiency is composed of a geometrical and an intrinsic factor. The former is the capability of the detector of intercepting the radiation and depends on the size of the detector and on the source-detector distance. The latter is the ratio between the radiation interacting with the detector and the radiation impinging on it. This factor depends on detector composition and thickness, on the radiation type and energy and so, also, on the attenuation coefficient.

In general, the detection efficiency can be expressed as:

$$D = g \cdot \epsilon \cdot f \cdot F \tag{2.8}$$

where g is the geometric efficiency, ϵ is the intrinsic efficiency, f is the fraction of the output signal that enters the pulse-height analyzer window and F is a factor that considers scatter and absorption contributions.

The aim is to find the best compromise between a good detection efficiency, that increases with increasing detector thickness, and a good spatial resolution, that decreases with increasing detector thickness.

2.4.2 Spatial Resolution

Spatial resolution is a measure of the gamma camera ability to detect details, meaning in the ability to resolve separated radioactive sources. Part of the image blurring is caused from the collimator characteristics and part from the NaI(Tl) crystal and the positioning electronics. The limit of the spatial resolution achievable with only the detector and electronics and without the blurring contribution of the collimator is called intrinsic spatial resolution. When also considering the contribution of the collimator, one talks about system resolution.

The resolution is calculated as the full width at half maximum (FWHM) of a profile drawn perpendicular to the image detail used for the evaluation at various locations in the field of view.

Intrinsic resolution is limited by two main factors: the multiple scattering of photons within the detector and the statistical fluctuation in the distribution of light photons among the PMTs from one scintillation event to the other. The former takes place when a photon is subject to Compton scattering within the detector crystal and both the interaction and the residual scattered photon are detected. The two are recorder together as a single event that is though mispositioned. This effect leads to a relatively small loss of resolution, especially for low-energy photons that are unlikely to undergo Compton scatter. The latter is the primary cause of the limited intrinsic resolution. It arises because of the Poissonian nature of the photons emitted from the scintillator: considering N light photons from scintillation events recorded from a PMT, the actual number of recorded photons will vary with a standard deviation of .

As suggested by NEMA NU 1, “Performance measurements of Gamma Cameras", the evaluation of the intrinsic spatial resolution can be performed by acquiring, without collimator and using a test pattern (a lead mask with 1 mm wide parallel slits),a pointlike source and evaluating the FWHM of the profile obtained taking a line perpendicular to the source image ([[25]]). For modern gamma cameras, the intrinsic spatial resolution is typically in the order of 2.9 – 4.5 mm for ^{99m}Tc, meaning for the 140 keV peak that is used as a standard reference.

It is important to point out that intrinsic resolution becomes worse in case of low energy gammas, since they produce fewer light photons per scintillation event. A thicker detector crystal, which is associated to a greater spreading of scintillation light, decreases the intrinsic resolution too. Another limit to the intrinsic spatial resolution is associated to events of type “B" in Figure 2.5, i.e. scatter events inside the NaI(Tl) crystal. In fact, the two photons are registered as a single event, which take place in some location along the line joining the two actual interaction sites. Luckily, this type of event does not cause serious degradation of the image quality in the energy range $\leq 300\ keV$.

The system spatial resolution is instead the actual parameter to consider for measurements and simulations. It differs from the intrinsic spatial resolution since it includes collimator blurring, septa penetration and the effect of the holes' diameter and length. Given the dependence of the collimator resolution on the source-collimator distance (see Equation 2.2), the system spatial resolution will depend on the source-collimator distance. The system spatial resolution can be evaluated by filling a capillary source with a ^{99m}Tc solution (see NEMA NU 1 [[25]]). The standard reference is the system spatial resolution at 10 cm in source-collimator distance, but the dependence of the resolution on this variable shall be evaluated too.

2.4.3 Energy Resolution

The energy resolution of the gamma camera is represented by the FWHM of the gaussian-shaped photopeak in the energy spectrum. The main factors that cause the broadening of the photopeak are:

- the statistical variations in the number of scintillation light photons;
- the statistical variations in the number of released photoelectrons by the photocathode;
- the non-uniform sensitivity of the PMT respect to scintillation light;
- the non-uniform light collection efficiency;
- the statistical variations in the multiplication factor of the PMT's dynodes;
- the electrical noise;
- the nonlinear energy response in the scintillator;
- the poor light coupling between the crystal and the PMTs.

Typical energy resolutions for modern gamma cameras range from 9% to 11% for the reference 140 keV gamma peak of ^{99m}Tc.

2.4.4 Dead Time

When subject to high counting rates, gamma camera systems may undergo counting losses and image distortion because of pulse pile-up. These inaccuracies can be corrected by applying dead time models, but corrections become increasingly inaccurate as counting losses increase.

Pulse pile-up can occur between any two events in the pulse-height spectrum when two photons impinge on the detector within a time interval comparable to the time resolution of the system. Energy-sensitive detectors such as NaI(Tl) scintillators usually incur in signal overlapping within the pulse amplifier, which cause baseline shift and pulse pile-up. Shifted or overlapped pulses may fall outside the analyzer window resulting in a loss of valid events referred to as dead time losses. The result is that the two photons can be seen by the system as a single event, they could be both lost misplaced in space.

When it comes to dead time, counting systems are classified in paralyzable or nonparalyzable type. In the former, an event causes the detector to be unresponsive for a certain period of time thus simply ignoring other events taking place. In the latter, events introduce a dead

time whether or not they were actually counted: an event occurring during the dead time of a previous event would not be counted but would still introduce its own dead time. Many nuclear medicine systems have multiple components in cascade, each having its own dead time and being either paralyzable, such as the scintillation detector, or nonparalyzable, such as the multichannel analyzer. The behavior of such systems is then a hybrid of the two previously described.

2.5 Conclusions

Image acquisition is a necessary step for the dosimetric procedure. In this chapter the fundamentals of the imaging methods used in this work were presented: SPECT and CT.

By performing a CT scan, the morphological information (i.e. the attenuation map) of the patient is acquired. By performing a SPECT scan, the functional information (i.e. where the radiopharmaceutical is located) is acquired. Both CT and SPECT scans, though, do not return three-dimensional images but a sequence of transverse projections of the patient. Thus, after being acquired, projection images from the gamma camera need to be reconstructed into three-dimensional tomographic images in order to successively quantify the activity in the tissues of interest.

The next chapter will thus introduce the fundamentals of image reconstruction, and how they are implemented into the iterative reconstruction softwares exploited in this work.

Chapter 3

Image Reconstruction

Radionuclide imaging as well as x-rays imaging consist in two-dimensional (2D) projections of three-dimensional (3D) source distributions. This results in obtaining images of structures at one depth in the patient that are obscured by the superimposed images of overlying and underlying structures.

The solution to this problem is solved with the tomographic imaging approach. Modern computed tomography (CT) techniques, such as positron emission tomography (PET), single photon emission tomography (SPECT) and x-ray CT, use detector systems placed or rotated around the patient to obtain different angular views, referred to as projections. Mathematical algorithms are then used to reconstruct the 2D projections into a 3D image representing the patient. The reconstruction of projection images of the detected emissions from radionuclides within the body is known as emission computed tomography (ECT), while the reconstruction of projection images of transmitted emission from an external source is known as transmission computed tomography (TCT). Even though there are differences in the implementation of ECT and TCT, the mathematical basis is the same for the two and will be treated as one.

In this chapter the tomographic reconstruction and its mathematical basis will be presented with some simplified assumptions. Data are assumed to be collected by a gamma camera equipped with a parallel-hole collimator and being detected only when impinging the crystal coming from a direction parallel to the collimator holes (see Figure 3.1). Scattering and attenuation are neglected, thus we consider the registered counts to be proportional to the total activity contained in the whole Line of Response (LOR) and we refer to them as “line

integral of the LOR". The projection profile is made considering all line integrals, and the collection pf projection profiles is the base on which the reconstruction of the image is made (see Figures 3.1 and 3.2).

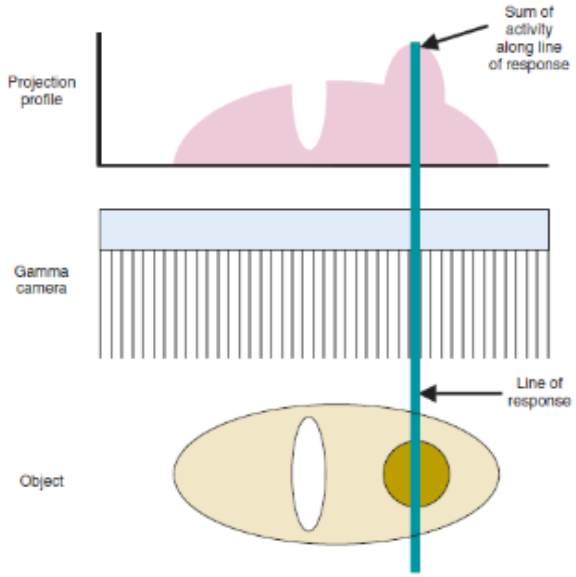

Figure 3.1: Ideal acquisition configuration: the collimator holes view only the radioactivity within a cylinder perpendicular to the gamma camera. The signal recorded in each hole is the sum of all the activity in the line of response. The final projection profile is shown [[26]].

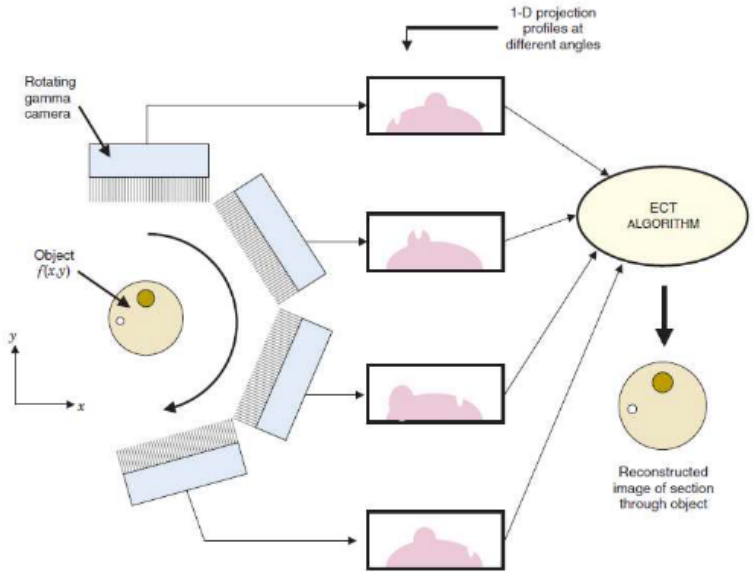

Figure 3.2: Working scheme of the reconstruction: the gamma camera head acquires projections while rotating around the patient [[23]].

3.1 Analytic Reconstruction

Considering an object represented by a 2D function $f(x, y)$, it can be described as a series of rays modeled with a parametric function as shown in Figure 3.3:

$$t = x\cos\theta + y\sin\theta \tag{3.1}$$

The line integral $p_\theta(t)$ can be defined as:

$$p_\theta(t) = \int_{(\theta,t)line} f(x,y)ds = \int_{-\infty}^{\infty}\int_{-\infty}^{\infty} f(x,y)\delta(x\cos\theta + y\sin\theta - t)dxdy \tag{3.2}$$

Equation 3.2 is the Radon Transform of the function $f(x, y)$ that is the integral transform taking a function $f(x, y)$ into a function $R[f(x, y)]$ whose value, on a specific line, is equal to the line integral of the function over that line. Projections data are path integrals of the object prole along a specific direction.

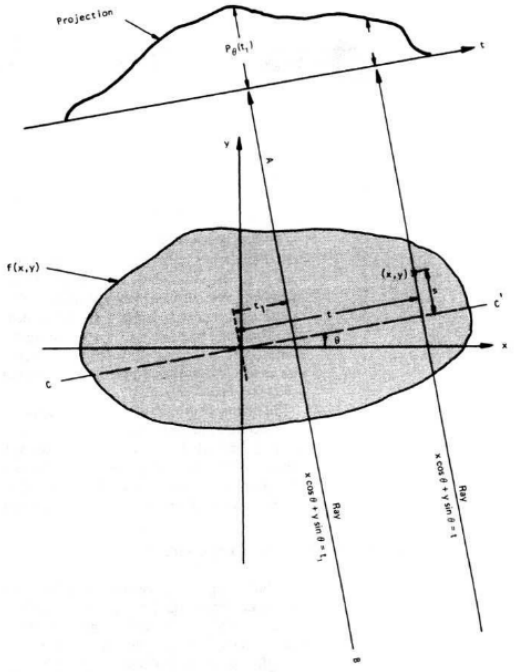

Figure 3.3: Object $f(x, y)$ and two rays of equation 3.1 [[27]]

All the projections may be represented as a function of the rotation angle they are acquired, and the full set of projection data $p_\theta(t)$ constituting a matrix in which each row represents the intensity across a single projection. The matrix is graphically represented with the so called sinogram, name that arises from the fact that the projection of a point-like object would have a sinusoidal shape (see Figure 3.4).

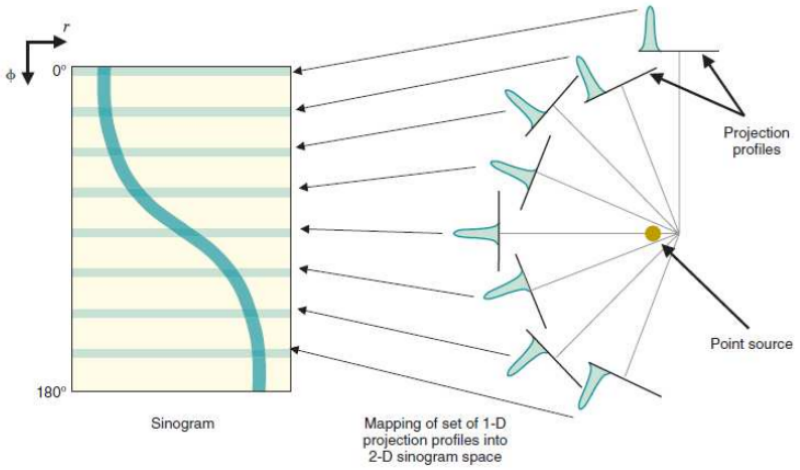

Figure 3.4: Illustration of the sinogram as a result of the projections of a point-like source [[23]].

The Fourier Slice Theorem states that the Fourier transform of a parallel projection of an image $f(x, y)$ taken at angle θ ($P_\theta(\omega)$) is equal to a slice of the two-dimensional Fourier transform of the original object, $F(u, v)$, subtending an angle θ with the u-axis (see Figure 3.5).

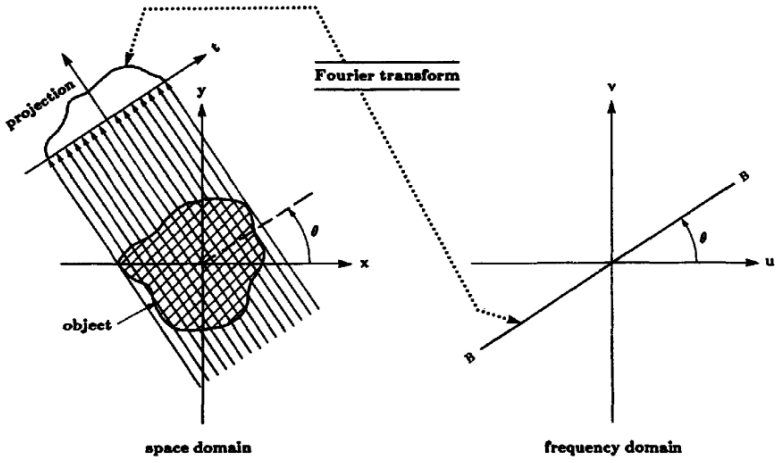

Figure 3.5: Illustration of the Fourier Slice Theorem [[27]].

By applying the Fourier Slice Theorem to Equation 3.2, one obtains:

$$P_\theta(\omega) = \int_{-\infty}^{\infty} p_\theta(t) e^{-2\pi i \omega t} \tag{3.3}$$

Equation 3.3 shows that the Fourier transformations of each object functions' projections at θ_1, θ_2, ..., θ_k angles determine the values of $F(u, v)$ on radial lines (see Figure 3.6). If an infinite number of projections were taken, then $F(u, v)$ would be known at all points in the (u, v) plane.

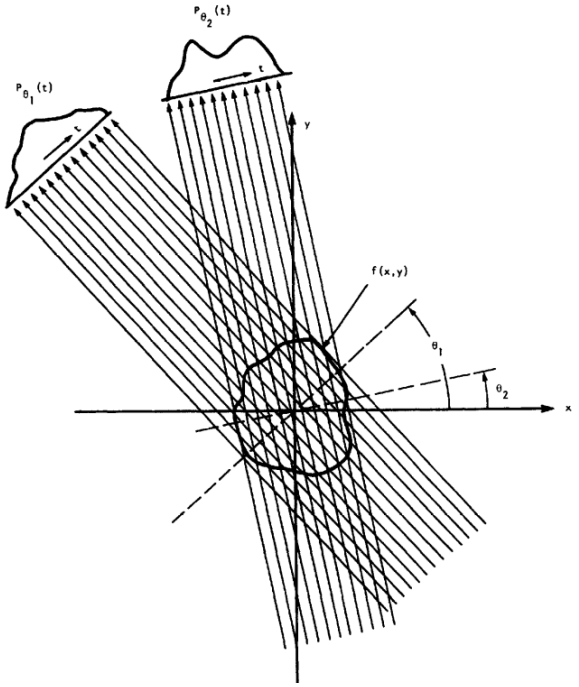

Figure 3.6: Object $f(x, y)$ and the projections for two different angles θ_1 andθ_2 [[27]]

Knowing $F(u, v)$, the object function $f(x, y)$ can be obtained by applying an inverse Fourier Transform:

$$f(x,y) = \int_{-\infty}^{\infty} \int_{-\infty}^{\infty} F(u,v) e^{2\pi i(ux+vy)} du dv \tag{3.4}$$

It should be then possible to reconstruct the object function by performing a two-dimensional inverse Fourier Transform on the projection data. The number of projections is finite though, implying that $F(u, v)$ has a finite number of measures and can be evaluated on a finite number of radial lines (see Figure 3.7).

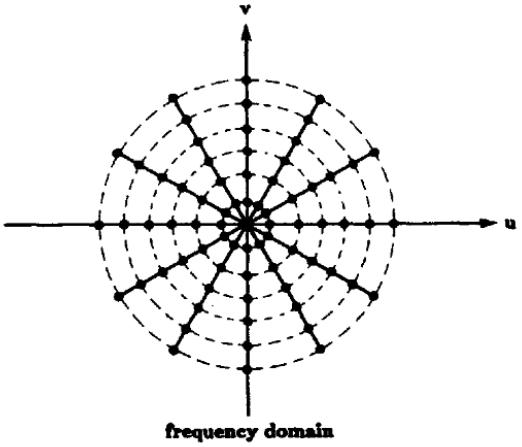

Figure 3.7: Representation of how a limited number of angles gives limited estimation of the Fourier Transform of the object along radial lines. The dots represent the actual location of estimates of the object's Fourier transform [[27]].

In order to be able to use Equation 3.4, one should then interpolate from these radial points

to the points on a square grid. This calculation is commonly performed by determining the values on the square grid by some kind of linear interpolation from the radial points. Since the density of the radial points becomes sparser as one gets farther away from the center, the interpolation error also becomes larger. This implies that there is a greater error in the calculation of the high frequency components in an image than in the low frequency ones, which results in some image degradation.

This issue is overcome by applying an algorithm called Filtered Backprojection, that can be derived from the Fourier Slice Transform with polar coordinates. Moving from rectangular coordinates (u, v) in the frequency domain to polar coordinates (ω, θ) with ($u = \omega \cos\theta$, $v = \omega \sin\theta$), Equation 3.4 becomes:

$$\begin{aligned} f(x,y) &= \int_0^{2\pi} \int_0^{\infty} F(\omega,\theta) e^{2\pi i \omega (x\cos\theta + y\sin\theta)} \omega d\omega d\theta \\ &= \int_0^{\pi} \left[\int_{-\infty}^{\infty} F(\omega,\theta) |\omega| e^{2\pi i \omega t} d\omega \right] d\theta \end{aligned} \tag{3.5}$$

That, by applying the Fourier Slice Theorem, becomes:

$$\begin{aligned} f(x,y) &= \int_0^{\pi} \left[\int_{-\infty}^{\infty} P_\theta(\omega) |\omega| e^{2\pi i \omega t} d\omega \right] d\theta \\ &= \int_0^{\pi} Q_\theta(x\cos\theta + y\sin\theta) d\theta \end{aligned} \tag{3.6}$$

with

$$Q_\theta(t) = \int_{-\infty}^{\infty} P_\theta(\omega) |\omega| e^{2\pi i \omega t} d\omega \tag{3.7}$$

The original 3D object is given by the Fourier Transform of the projections multiplied by $|\omega|$, that is a filtering operation: $Q_\theta(t)$ is thus known as filtered projection. Then, all the projections corresponding to different angles are added to form the estimation of $f(x, y)$. Equation 3.6 is known as Filtered Backprojection method (FBP).

It should be noticed that the value of $t = x\cos\theta + y\sin\theta$ is the same for all (x, y) for the same projection line, and so for a given value of θ. Thus, the filtered projection Q_θ will give the same contribution to the reconstruction for all the points on the same projection line.

The complete process can be summarized as follows: for each values of θ from 0 to

180 degrees the system measures the projection $p_\theta(t)$ and computes its Fourier Transform, obtaining $P_\theta(t)$. The result is then multiplied by the weighting function $|\omega|$, and finally the backprojection process is applied through the Inverse Fourier Transform of the filtered projections. In Figure 3.8 a comparison between simple backprojection and filtered one is presented.

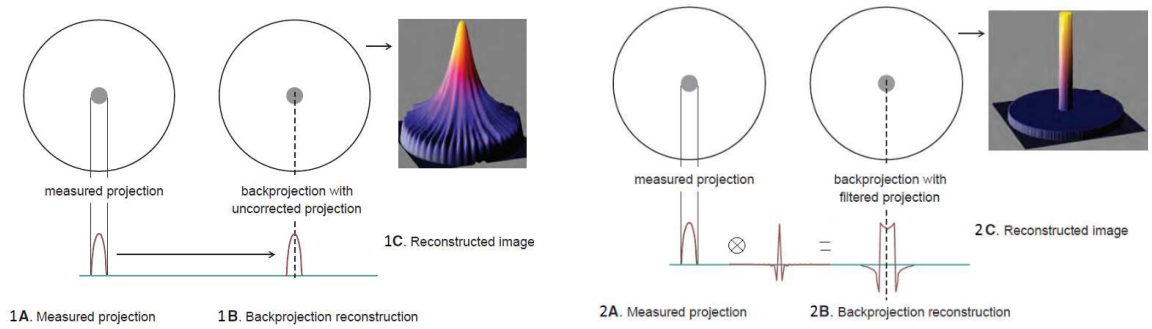

Figure 3.8: Figure 1B: backprojection method applied to a circular object and the resulting tridimensional reconstruction (1C). Figure 2: filtered backprojection applied to the same object as a result of the convolution of the backprojection and the ramp filter kernel in spatial domain. [[22]].

3.2 Iterative Reconstruction

Modern reconstruction systems use iterative algorithms, whose operation is sketched in Figure 3.9.

The idea is to start by estimating the true image $f(x, y)$ with a very simple approximation $f'(x, y)$, such as a blank or a uniform image. Then the algorithm calculates the projection data by forward projection, that is performed by summing up the intensities along the ray paths for all projections through the estimated image. The set of generated projections is then compared to the recorded projections, and their difference is used to adjust the estimated image. The algorithm stops when the $f'(x, y)$ converges towards the true image, ideally obtaining:

$$f'(x, y) \cong f(x, y) \tag{3.8}$$

In practice the guessed image will always differ from the true image due to inaccuracies and statistical noise. Iterative reconstruction algorithms are more time consuming with respect to Filtered Backprojection, and this is due to the fact that the process involves a certain amount of iterations and because the projection process is repeated during every iteration. Iterative

reconstruction algorithms also incorporate several factors that consider specific characteristics, such as the collimator, the object scatter, the system geometry and the detector resolution: these features increase the accuracy of the reconstruction but lengthen the process duration even more.

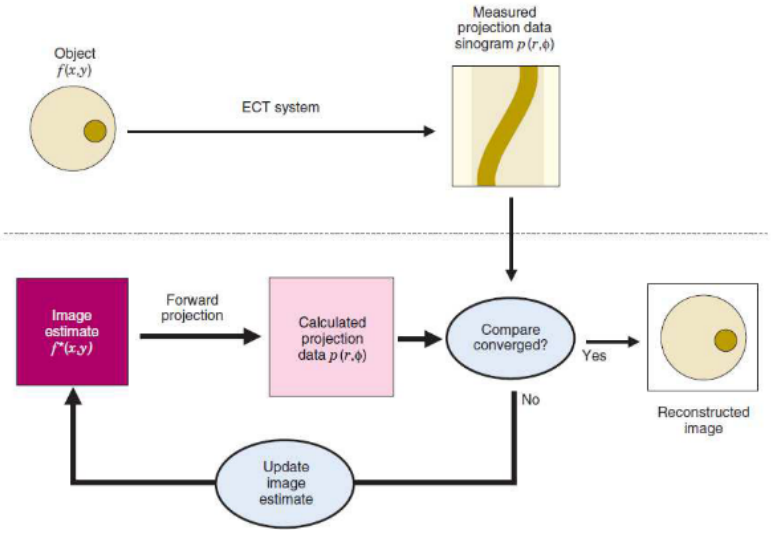

Figure 3.9: Functioning scheme of an iterative reconstruction algorithm [[23]].

3.3 MLEM, OSEM, Flash 3D

Collimator Detector Response (CDR) is of the most degrading factors in SPECT imaging [[28]]. It is caused by several factors: photons which passes through the holes' septa, photons which penetrate holes septa and photons which, despite the scattering with hole septa, are been detected. A compensation factor to reduce the CDR effect has to be provided for each radionuclide of interest (CDR will be discussed in section 4.1.1).

The Maximum Likelihood Expectation-Maximization (MLEM) is an example of iterative reconstruction model. It aims at evaluating the activity distribution that maximize the Poisson Likelihood starting from the SPECT projection data ([29]) and can implement and incorporate CDR corrections directly into the reconstruction.

An expectation-maximization algorithm incorporates statistical considerations to compute the maximum-likelihood source distribution that would have created the observed projection data, including the effects of counting statistics. Specifically, it assigns greater weight to

high count elements of a profile and smaller weight to low-count elements; on the opposite, backprojection assigns the same weight to all elements. The statistical behavior of the physical quantities is taken into account by considering both the emitted and the detected radiation as Poisson variables [[30]].

If $\overline{f}_j$ is the average number of disintegrations occurring in pixel j and a_{ij} is the element of the detector matrix A, the mean number of photons emitted from pixel j and detected from bin i will be $a_{ij}\overline{f}_j$. Thus, the total number of photons $\overline{g}_i$ detected from bin i will be:

$$\overline{g}_i = \sum_{j=1}^{m} a_{ij}\overline{f}_j \tag{3.9}$$

Because of the Poisson nature the variables, the probability of detecting g_i photons is calculated as:

$$P(g_i) = \frac{e^{-\overline{g}_i}}{e^{-g_i}g_i!} \tag{3.10}$$

The likelihood function $L(\overline{f})$ will be $P(g|\overline{f})$, meaning the probability of observing g with $\overline{f}$ emission map. Since the two Poisson variables emitted photons and detected photons are independent, the final probability will be the product of the single probabilities:

$$L(\overline{f}) = P(g|\overline{f}) = P(g_1)P(g_2)..P(g_n) = \prod_{i=1}^{n} P(g_i) = \prod_{i_1}^{n} \frac{e^{-\overline{g}_i}}{e^{-g_i}g_i!} \tag{3.11}$$

Thus, by taking the natural logarithm and using Eq. .., one obtains the likelihood function:

$$l(\overline{f}) = \log L(\overline{f}) = \sum_{i=1}^{n}(-\overline{g}_i + g_i \log(\overline{g}_i) - \log(g_i!)) = \sum_{i=1}^{n}\Big(-\sum_{j=1}^{m} a_{ij}\overline{f}_j + g_i \log\Big(\sum_{j=1}^{m} a_{ij}\overline{f}_j\Big) - \log(g_i!)\Big) \tag{3.12}$$

In order to find the maximum, it is necessary to derive and equal the result to zero (is demonstrated to have one and only one maximum):

$$\frac{\partial l(\overline{f})}{\partial \overline{f}} = 0 \tag{3.13}$$

To finally obtain the MLEM formula:

$$\overline{f}_j^{k+1} = \frac{\overline{f}_j^{k}}{\sum_{i=1}^{n} a_{ij}} \sum_{i=1}^{n} \frac{g_i a_{ij}}{\sum_{j'=1}^{m} a_{ij}\overline{f}_{j'}^{k}} \tag{3.14}$$

Where:

- $\sum_{i=1}^{n} \frac{g_i}{\sum_{j'=1}^{m} a_{ij} \overline{f}_{j'}^{k}}$ is the ratio between the number of measured counts and the mean number of counts in bin i;

- $\sum_{i=1}^{n} \frac{g_i a_{ij}}{\sum_{j'=1}^{m} a_{ij} \overline{f}_{j'}^{k}}$ is the backprojection of the previous ratio for pixel j.

The MLEM formula 3.14 can be interpreted as:

$$Image^{k+1} = Image^{k} \times Normalized\, BP\, of\, \frac{Measured\, projection}{Projection\, of\, the\, Image^{k}} \tag{3.15}$$

A simplification of the MLEM algorithm is the Ordered-Subsets Expectation Maximization [[31]]. The OSEM model consists in considering only subset of the total amount of angular views in order to reduce the time requested for the algorithm to converge to the final image.

When it comes to image reconstruction, besides explicit Poisson modelling, an important additional advantage of the MLEM reconstruction algorithm and its accelerated version OSEM is the capacity to implement attenuation and scatter corrections, and to model the collimator-detector response (CDR) directly into the reconstruction. While the attenuation and scatter corrections are involved in the interaction of the photons with the imaged object, the CDR represents their interaction with the detection system (collimator, crystal and electronic).

With increasing number of iterations the difference between the mean reconstructed image and the true activity distribution is reduced, but at the cost of increasing artifacts and noise level [[32], [33]].

Siemens developed another iterative reconstruction algorithm, called Flash 3D. Flash-3D is similar to OSEM but it has the characteristic of introducing, in the reconstruction method, also the 3D collimator beam modelling. Considering a depth dependent resolution [[34]], Flash 3D gives a higher spatial resolution, lower noise, better contrast and reduction of distortions [[35], [36]].

3.4 Conclusions

Image reconstruction allows to transform two-dimensional transverse projections of the patient SPECT and CT scans into three-dimensional images. Moreover, with specific iteration reconstruction processes (MLEM and OSEM), it allows to implement crucial corrections of imaging degrading factors.

Once the patient's images have been acquired and reconstructed, the following step in the dosimetric evaluation process is the quantification of the image. In fact, in order to evaluate the Absorbed Dose to the patient's tissues, a precise measurement of the radionuclide activity in the sites of interest is required.
The activity quantification and a detailed description of the corrections to be performed on SPECT images are be the object of the next chapter.

Chapter 4

Absolute Activity Quantification

As discussed in Chapter 3 and Chapter 4, single photon emission computed tomography (SPECT) allows the visualization of the distribution of radioactivity within the human body. SPECT also allows to exactly quantify the concentration of radioactivity within a given volume of tissue in absolute units, e.g. as kilobecquerels per cubic centimetre.
Image absolute quantification is, in fact, a necessary step in order to evaluate the Absorbed Dose to the tissues of interest, meaning to monitor the damage assessed by MRT treatment to tumors and to organs at risk.
In this chapter, the absolute quantification of SPECT images and the corrections to be implemented are discussed.

In order to perform quantification of SPECT images some essential steps need to be performed. A first step involves quantitative SPECT reconstructions, discussed in Chapter 3. Since the data acquired in projections are affected by physical phenomena such as photon attenuation and scatter, collimator blurring, camera dead-time and partial volume effects, in order to get quantitatively accurate images, all these factors must be properly compensated for during the reconstruction process. With the introduction of hybrid SPECT/CT imaging systems and the development of statistical iterative reconstruction algorithms such as MLEM and OSEM, quantitative reconstructions have become available for the majority of the commercial SPECT/CT cameras [[37], [38], [39]].

A second step is to apply camera calibration factor (CF) to the reconstructed images: this factor translates the three-dimensional (3D) count maps into 3D activity maps. It is

important to stress at this point that CF provides only a numerical coefficient necessary for this translation.

Finally, in order to obtain a quantitative value of the activity contained in any particular region of interest (ROI) or volume of interest (VOI) such as a specific organ or a tumor lesion, the third step involves the segmentation of the activity map. As segmented volumes will be affected by partial volume effects (PVE), for accurate activity quantification, appropriate PVE correction methods must be applied [[40]].
Alternatively, a different approach to Absorbed Dose calculation removes the need for segmentation: voxel-based quantification. Voxel dosimetry is defined as the calculation of radiation absorbed dose to tissue in voxels, meaning in regions with dimensions ranging from a few centimeters to hundreds of micrometers. As the name implies, voxel dosimetry is generally associated with tomographic imaging, and will be discussed in Chapter5.

4.1 Corrections

The ideal situation of a detector whose signal varies linearly with the activity and thus being able to allow a complete conversion of the collected counts into activity is never fully achieved. This is due to several physical effects that have to be corrected for, affecting both the photons collection, their conversion into signal and the reconstruction algorithm (see Figure 4.1).

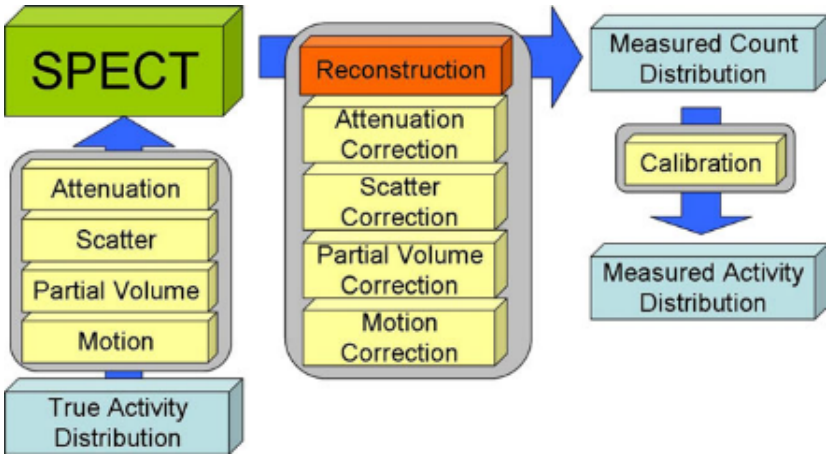

Figure 4.1: Workflow for activity distribution calculation through SPECT imaging and its corrections [[38]].

For instance, the reconstruction algorithm is based on ideal assumptions having slight but

significant differences from the reality, such as the definition of the line of response as a cylinder parallel to the holes' septa, although it actually is a cone (see Section 3.1). Moreover, because of scattered radiation and septal penetration, the information about the activity contained in a specific voxel is spread to different voxels, thus implying that voxels contain information about different regions in the studied patient or phantom (see Section 2.1.4). The attenuation of photons coming from the inner parts of the patient or phantom plays a significant role in the recorded signal too, as well as the Partial Volume Effect (PVE) affecting the segmented VOIs.

In the following sections these effects and the computational solutions applied to correct for them will be presented. All the corrections presented by this chapter, with the exception of the partial volume effect correction, are usually implemented into the image reconstruction process.

4.1.1 Collimator Detector Response

As anticipated in section 3.3, Collimator Detector Response (CDR) is of the most degrading factors in SPECT imaging [[28]]. It is caused by several factors: photons which passes through the holes' septa, photons which penetrate holes septa and photons which, despite the scattering with hole septa, are been detected.

The main components of the CDR are the intrinsic response that is caused by scatter events occurring in the crystal and the uncertainty of the position estimation of the detected photon, the geometric response representing a distance-dependent spatial resolution caused by the finite collimator hole length and width, scatter events occurring in the collimator, and the septal penetration occurring when photons are detected after passing through the walls of the collimator holes. These effects contribute to the emergence of star-shaped structures, as shown in Figure 4.2 .

With increasing source-to-collimator distances, the counts are distributed over wider areas and the stars appear to be dilated. In order to obtain quantitatively correct images, these effects need to be considered and corrected for. The CDR is commonly assumed to be Gaussian and modelled as such in the reconstruction. Significant differences between the

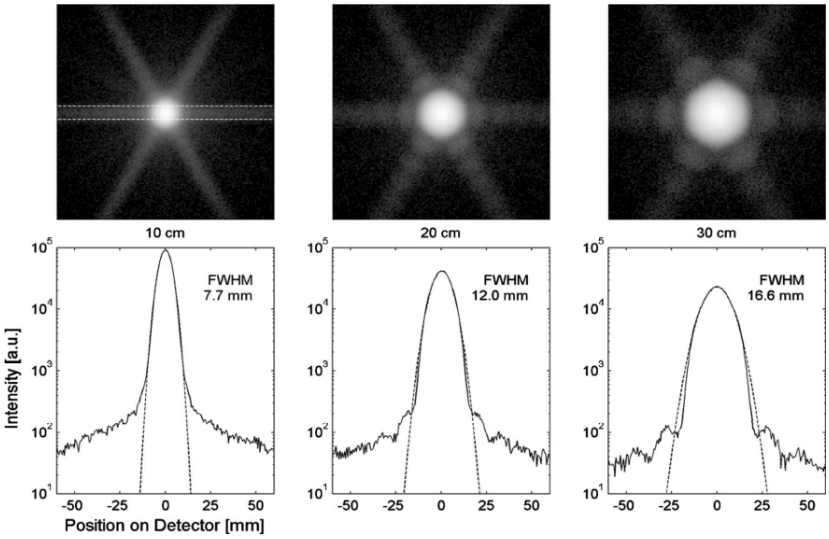

Figure 4.2: Top row: images of ^{99m}Tc point sources measured at different typical source-to-collimator distances. Bottom row: line profiles through the center of the point sources. The extent of the line profiles is indicated in the upper left image. Gaussian functions were fitted to the line profiles. The full widths at half maximum (FWHM) values of the Gaussians are provided as well [[41]].

Gaussian model and the real CDR can be found, especially in regions on the edge of the geometric response where the model systematically underestimates the number of detected counts. Additionally, a rotationally invariant function like the Gaussian cannot express the contours found in real CDRs which mimic the shape of the collimator hole. Multiple solutions have been proposed for further improving the modelling: MC simulations can be used to calculate the CDR during reconstruction [[28]] or prior to reconstruction [[42]]. Other approaches rely on more sophisticated mathematical models and fit their free parameters to a set of point source measurements [[43]]. Nevertheless, Gaussian modelling is the method that is applied in most clinically available tools, such as the reconstruction algorithms used in this work (SIEMENS Flash 3D, CastOr).

CDR correction, has to be provided for each radionuclide of interest, is implemented in MLEM and OSEM reconstruction algorithms.

4.1.2 Attenuation

SPECT images are heavily affected by attenuation artifacts. In fact, the probability of detection depends on the location of the decay and on the linear attenuation coefficients $\mu(r)$ of the object. For the correction of the attenuation effect in the reconstruction step, the spatial distribution of the attenuation coefficients of the examined object for the photon

energy of the radionuclide used needs to be known.

Before the introduction of hybrid SPECT/CT devices, radionuclide (source-based) transmission measurements (e.g. ^{153}Gd, ^{99m}Tc, ^{133}Ba) were commonly employed [[38]]. They consist in a first step, named “blank" or “reference scan", which is a simple acquisition of the source. Then, a second step consisting in the acquisition with both the source and the considered object, allowed to have a relation between the two different scans, particularly between the two registered intensities:

$$I_{trasm} = I_{ref} e^{-\mu x} \tag{4.1}$$

$$\log\left(\frac{I_{ref}}{I_{trasm}}\right) = \mu x \tag{4.2}$$

Thus, the projection profiles of can be obtained and reconstructed. These source-based methods have the advantage that the same detector can be used for both the emission and the transmission scans, which makes the methods very cost-efficient. However, they are disadvantageous for the image quality of the transmission scan, due to a poor signal-to-noise ratio and due to a limited spatial resolution.

With the advent of hybrid SPECT/CT, and thus the availability of highly correlated high-quality X-ray CT transmission scans, it is now standard to use CT scans for attenuation correction. The CT scans, usually in Hounsfield units (HU), have to be converted to linear attenuation coefficients $\mu(E)$ whose value depend on the photon energy. The transformation can introduce some errors: first, it is specific for different acceleration voltages and beam filters of the CT scanner [[44]]. Second, the polychromaticity of the X-ray beam also introduces artefacts, mainly caused by beam hardening. Finally, patient motion that occurs between the emission and transmission acquisitions in a hybrid system can lead to artefacts, which in turn can lead to false readings of the SPECT images [[45]].
Similarly to the CDR correction, attenuation correction is implemented into the reconstruction algorithms.

4.1.3 Scatter

In gamma camera imaging, a significant fraction of the detected photons is scattered in the body. This is due to the finite energy resolution of the gamma camera, which results in imperfect energy-based scatter rejection. The scatter to primary ratio (SPR) depends on the radionuclide, energy window, energy resolution, source depth and the size of the object. Scatter correction requires estimating the scatter component of the projection data combined with a compensation method. Most frequently, the scatter component is estimated using data acquired in auxiliary energy windows.

The most common and flexible methods based on auxiliary energy windows are the triple energy window (TEW) method and the dual energy window (DEW) method. The TEW method uses two scatter energy windows, one above and one below the photopeak window, as illustrated in Figure 4.3. The scatter is estimated from the counts in the scatter windows using a trapezoidal approximation where counts in the scatter windows divided by their window widths are treated as the sides, and the scatter in the photopeak window is the area of the trapezoid. The estimated scatter counts in the photopeak window estimated using TEW are given by:

$$c_{TEW} = \left(\frac{c_{low}}{w_{low}} + \frac{c_{up}}{w_{up}}\right) \cdot \frac{w_{peak}}{2} \tag{4.3}$$

clow and cup are the counts in the lower and upper scatter windows, respectively, and wpeak, wlow and wup are the widths of the photopeak, lower scatter and upper scatter windows, respectively. Thus, the corrected counts for the main energy peak will be:

$$c_{corr} = c_{main} - c_{TEW} \tag{4.4}$$

The DEW method, also called Jaszczak correction [[46]] uses a Compton window and assumes a proportionality (usually k=0.5) between the photons detected in the Compton windows and the photopeak. The calculation for the scatter contribution is analogous, where one considers the counts in the scatter window divided by their window width to be treated as the side, and the scatter in th e photopeak window to be the area of the triangle:

$$c_{DEW} = \frac{c_{low}}{w_{low}} \cdot \frac{w_{peak}}{2} \tag{4.5}$$

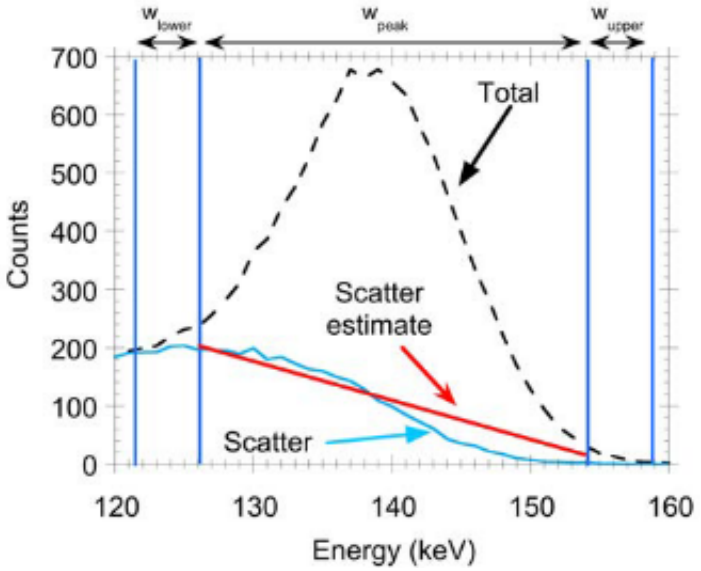

Figure 4.3: Illustration of the TEW method [[2]].

In DEW and TEW methods, the scatter images are acquired simultaneously with the photopeak image. For each pixel of the projection image, the amount of scattered radiation in the photopeak window image is estimated from the scatter window images. Subsequently this amount can be subtracted from the projections or, more commonly, incorporated into the reconstruction process.

4.1.4 Dead Time

As previously described in section 2.1.4, events occurring in close temporal proximity to a preceding event will be lost or mispositioned because of the short but finite time interval required to process each recorded event.

In SPECT after therapy, where injected activities are often over 4 GBq, dead-time (DT) losses can be substantial and dead-time related count losses must be corrected. Even with dead-time correction, however, such high counting rates may result in prohibitive image distortion. Dead-time correction is particularly important for radionuclides with multiple photon emissions such as 131I, as photons not included in the acquisition window also contribute to dead time. Before SPECT reconstruction of posttherapy data, the measured projection counts should be corrected for camera dead time. The simplest method for dead-time correction is based on monitoring counts corresponding to a reference source placed at the edge of the

camera FOV. Another way of addressing the DT problem is to perform a series of phantom experiments with gradually decaying activity, using the same acquisition protocol and scatter correction as used for patient studies. Analysis of count losses in these phantom images can be used to establish DT correction factors as a function of count rate for any particular camera system.

Although in principle, in radionuclide therapy imaging the count losses related to DT effects can be substantial, in ^{177}Lu imaging (that is the radioisotope studied for patients in this work), the DT effects are actually rather small (even for high activities) because of the low yield of photons emitted in the decay of ^{177}Lu and the very small bremsstrahlung contribution.

4.1.5 Partial Volume Effect

When it comes to volume segmentation, meaning the operation of volume of interest (VOI) contouring for dosimetric evaluation on SPECT images, the limited spatial resolution affects the activity quantification. The spill-out effect, named partial volume effect (PVE), consists in the activity of the ROI/structure distributing over the borders and therefore "lost" for the quantification of that structure: the activity inside the VOI is decreased. The degree of the PVE depends on the system spatial resolution, the true distribution of radioactivity in the image and specifically to the VOI volume.
PVE correction is thus performed after the SPECT images have been reconstructed and quantified, and is a preliminar step to the absorbed dose calculation, that will be discussed in the next chapter.

Ideally, the intensity of each pixel in a SPECT image would be proportional to the activity within the corresponding volume of tissue in the patient. For sources or measurement volumes of the size of the system resolution or lower, the sum of the intensities of all the pixels attributable to the studies source still reflects the total amount of activity. Though, the intensities of the individual pixels do not accurately reflect the real activity concentration because the signal is distributed over a volume that is larger than actual size of the source. This PVE is important for both qualitative and quantitative SPECT imaging, and it has to be corrected for to accurately estimate activity concentrations.

An example of the PVE is illustrated in Figure 4.4, where a series of different volume spheres are presented with the spill-out effect of their acquisition.

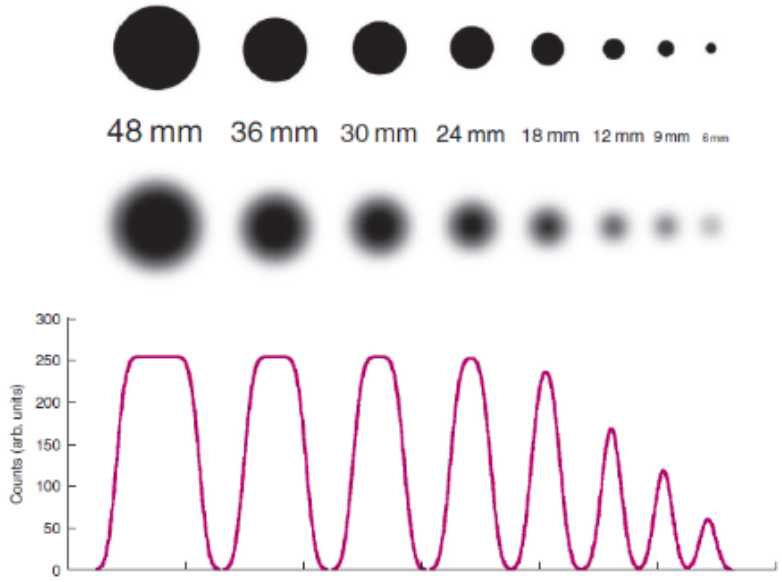

Figure 4.4: Illustration of the partial volume effec: on the top row, spheres of different size and same activity concentration are shown; in the middle row, SPECT acquisition simulations of the same spheres. The bottom row shows their count profiles [[23]].

The ratio between the apparent activity concentration and the real one is called recovery coefficient (RC), and it depends on the source dimension. Thus, PVE corrections can be estimated through phantom studies, using Jaszczak phantom with known volume spheres. The RC factors for the specific source diameter can be used to correct the observed activity concentration.

Figure 4.5 illustrates RC as a function of the diameter of the cylindrical or spherical source. As one can see, for small volumes the PVE correction will be significant, and it will asymptotically reach a plateau of value 1 for higher volumes.

4.2 SPECT Calibration Factor

The calibration of the SPECT imaging system volume sensitivity CF (e.g. in cps/Bq) (Eq. 4.6) is the final requirement for absolute quantitative imaging.

This parameter is the factor that gives the proportion between the counts of a determined

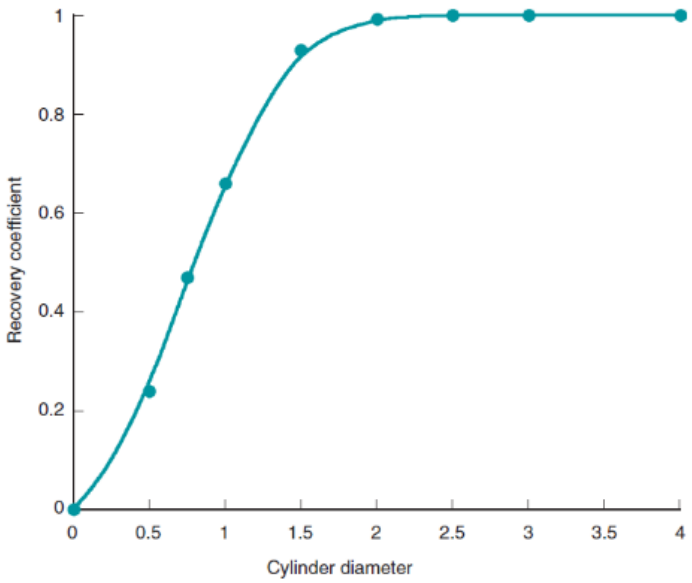

Figure 4.5: Typical recovery coefficient curve [[23]].

region of interest (ROI) recorded from the detector and the activity value in the same ROI. It is named Calibration Factor (CF) and can be determined through a SPECT study of a cylindrical phantom [[32], [33], [47]].

The value of the CF depends on the energy of the measured photons. Therefore, it is radioisotope specific and represents the joint sensitivity of the camera and the collimator for the detection of a particular isotope's emissions in the energy windows that are used for data acquisition.

The expression for the calculation of the CF is [[38]]:

$$CF = \frac{R}{V_{VOI} \cdot c_{Vol}} \times \exp\left(\frac{T_0 - T_{cal}}{T_{1/2}} \cdot \ln 2\right) \times \left(\frac{T_{acq}}{T_{1/2}} \cdot \ln 2\right) \times \left(1 - \exp\left(-\frac{T_{acq}}{T_{1/2}} \cdot \ln 2\right)\right)^{-1} \quad (4.6)$$

The measurement procedure is as follows [[25]]: large (to avoid partial volume effects) cylindrical phantom with known activity concentration c_{Vol} (in Bq/ml) is scanned. Corrections for attenuated and scattered photons are applied in reconstruction. A large VOI with volume V_{VOI} (in ml) is placed in the reconstructed image. T_0 is the start time, and T_{acq} the duration of the acquisition. $T_{1/2}$ is the half-time of the radionuclide used and T_{cal} the time of the activity calibration. R (in cps) represents the counting rate measured in the VOI. Finally, according to Equation 4.6, a calibration factor from detected counts per second to becquerels

is derived.

The first exponential term of Equation 4.6 corrects for decay in the time interval between calibration and the acquisition start. The second and third parenthesis correct for the time duration of the acquisition and calculate the mean counts considering an exponential decay during acquisition. These last corrections are quite small given the acquisition time durations and the half-life of the radionuclides used in this thesis (6h for ^{99m}Tc and 6.6gg for ^{177}Lu, with a scan duration of about 30min). Thus, in a first approximation, the CF formula may be simplified to:

$$CF = \frac{R}{V_{VOI} \cdot c_{vol}} \times \exp\left(\frac{T_0 - t_{cal}}{T_{1/2}} \cdot \log 2\right) \tag{4.7}$$

The CF unit is cps/MBq and has to be computed for every combination of radionuclide and collimator used.

4.3 Conclusions

SPECT allows the three-dimensional visualization of radioactivity within the human body. In SPECT, image quality is compromised by several factors including photon attenuation, photon scatter and the partial volume effect. These variables also confound the capacity of SPECT to quantify the concentration of radioactivity within given volumes of interest in absolute units.

Iterative SPECT image reconstruction techniques incorporating information from SPECT/CT image datasets greatly increase the accuracy of SPECT in quantifying radioactivity concentrations in phantoms and also in humans. After applying the forementioned corrections during the reconstruction process and the calibration factor to the resulting three-dimensional SPECT images, one can correctly associate activities (e.g. MBq) or activity concentrations (e.g. MBq/ml) to the tissues of interest.

The final process in the dosimetric procedure is finally that of calculating the Absorbed Dose (e.g. Gy) to the tissues of interest when considering as source of radiation the assessed activity distributions inside the patient. The calculation of Absorbed Dose with different

methods will be presented in the following chapter.

Chapter 5

Internal Radiation Dosimetry

As exposed in Chapter 1, ionizing radiation may damage living tissue. This effect is exploited in radionuclide therapy to damage cancerous cells, but radiopharmaceuticals also deposit in non-target tissues and organs. It is thus crucial to quantitatively estimate the damage assessed to the different tissues, that is established through the evaluation of the absorbed dose: the best therapeutic effect has to be ensured while limiting the dose imparted to healthy tissues and monitoring the dose delivered to organs at risk (OaR).

The computation of the absorbed dose to tumor lesions and organs is a complex task. The first step, as explained in the previous chapters, is the knowledge of the radiopharmaceutical distribution in the patient over time, specifically inside a source organ. Then, the calculation of the energy emitted from the radiopharmaceutical accumulated in the source organ and delivered to the target organ is necessary. This calculation is particularly difficult, since it depends on the radiation type and energy but also on the patient's anatomy and can be only carried out starting from information obtained through the CT and SPECT imaging carried out on the patient after the radiopharmaceutical injection.

To estimate the absorbed dose for the tissue of interest, one has to determine the absorbed energy per unit mass. Depending on the radionuclide, particles or rays of characteristic energy and abundance will be emitted from the source tissue at a rate dependent on the activity amount and will hit the target tissue depositing energy. In particular, the ratio between the energy E absorbed within the target and emitted energy E_0, also called absorbed fraction ϕ, is a number between 0 and 1, and has value 1 for electrons and beta particles that are

considered as 'nonpenetrating' radiation.

$$\phi = \frac{E}{E_0} \tag{5.1}$$

A generic equation for the absorbed dose rate can be then defined as:

$$\dot{D} = \frac{kA \sum_i n_i E_i \phi_i}{m} \tag{5.2}$$

where $\dot{D}$ is the absorbed dose rate ($rad\,h^{-1}$ or $Gy\,s^{-1}$), A is the activity (μCi or MBq), n is the number of radiations with energy E emitted per nuclear transition, E is the energy per radiation (MeV), ϕ is the fraction of energy emitted that is absorbed in the target, m is the mass of target region (g or kg) and k is a proportionality constant.

In order to obtain the total absorbed dose, the time integral of the dose equation must be calculated. In most cases, the only term which has time dependence is the activity A, so the integral is just the product of all of the factors in the above equation except for activity by the integral of the time-activity curve:

$$\overline{D} = \frac{k\tilde{A} \sum_i n_i E_i \phi_i}{m} \tag{5.3}$$

where D is the absorbed dose (rad or Gy) and $\tilde{A}$ is the cumulated activity ($\mu Ci\,h$ or $MBq\,s$).

Equations 5.2 and 5.3 are generic equations that have to be developed for the practical calculations. The most used calculation system has been developed by the Medical Internal Radiation Dose (MIRD) Committee of the Society of Nuclear Medicine.

5.1 MIRD System

The Committee in Medical Internal Radiation Dose (MIRD) was formed in 1965 with the purpose of standardize internal dosimetry calculations and to enhance the available data about radiopharmaceuticals' kinetics. In 1968 the first of the MIRD Pamphlets was published [[48]] containing a unified approach to internal dosimetry. The nomenclature and the equations

were then revised in MIRD pamphlet n. 21 [[49]]

The equation for the absorbed dose rate provided by the MIRD scheme is misleadingly simple:

$$\dot{D}(r_T, t) = \sum_{r_S} A(r_S, t) \cdot S(r_T \leftarrow r_S, t) \tag{5.4}$$

Where $A(r_S, t)$ is the time-dependent activity of the radiopharmaceutical in source tissue r_S , and $S(r_T \leftarrow r_S, t)$ is the radionuclide-specific quantity representing the mean absorbed dose rate to target tissue r_T at time t after administration per unit activity present in source tissue r_S. D_{r_T} is then computed by summing all the contributions from source tissues. Among these, the self-absorbed dose provides the largest contribution.

5.1.1 Time Integrated Activity

The time integrated activity, that is the number of decays in the source region, is calculated as the area under the curve that describes the activity as a function of time in the source region after the administration of the radiopharmaceutical ($\tilde{A}(r_S, t)$).

$$\tilde{A}(r_S) = \int A(r_S, t)dt \tag{5.5}$$

The time-integration period T_D, for which the time-integrated activity in the source region is determined, is commonly chosen from the time of administration of the radiopharmaceutical until infinite time (Equation 5.6). However, the integration period should be matched to the biological end point studied in combination with the time period in which the relevant absorbed dose is delivered.

$$\tilde{A}(r_S) = \int_0^{T_D} A(r_S, t)dt \tag{5.6}$$

The time-integrated activity coefficient $\tilde{a}(r_S, T_D)$ represents the cumulative number of nuclear transformations (Bq $\cdot$ s) occurring in source tissue r_S over a dose-integration period T_D per unit administered activity A_0 (Bq). The time-integrated activity coefficient was named the 'residence time' τ in the MIRD Primer and is shown in Equation 5.7.

$$\tilde{a}(r_S, T_D) = \int_0^{T_D} a(r_S, t)dt = \frac{1}{A_0} \int_0^{T_D} A(r_S, t)dt \tag{5.7}$$

The activity in a region as a function of time is commonly determined from consecutive quantitative imaging sessions after the administration and can be described by a sum of exponential functions.

$$A(r_S, t) = \sum_j A_j \cdot e^{-t(\lambda+\lambda_j)} \tag{5.8}$$

Where j denotes the number of exponentials, A_j the initial activity for the j^{th} exponential, λ the decay constant for the radionuclide, λ_j the biological decay constant and t the time after the administration of the radiopharmaceutical. The sum over j of the coefficients A_j gives the total activity in the source region at the time of the radiopharmaceutical administration (t = 0).

The decay constant λ equals the natural logarithm of 2 divided by the half-life, that in the case of the activity of a particular radioisotope deposited in a living tissue is the effective half-life $T_{1/2,eff}$. $T_{1/2,eff}$ is the combination of the physical half-life $T_{1/2}$ and the biological half-life $T_{1/2,j}$ (Equation 5.9).

$$\frac{1}{T_{1/2,eff}} = \frac{1}{T_{1/2,j}} + \frac{1}{T_{1/2}} \tag{5.9}$$

Where the biological half-life $T_{1/2,j}$ is the time required for a biological tissue to eliminate, by natural processes, half of the amount of the radioactive material that has entered it.

The shape of the fitted curve, which describes the activity as a function of time after the administration of the radiopharmaceutical, can be strongly influenced by the number and timing of the individual activity measurements. Three data points per exponential phase should be considered the minimum data required to determine the pharmacokinetics, and data points should be followed for at least two to three effective half-lives.

5.1.2 S-values

The starting point for the calculation of the S-values is the Energy emitted per unit of cumulated energy. It is given by the Equilibrium Absorbed Dose Constant (Δ), that is a factor to be calculated for each type of emission for the radionuclide of interest. It is given by

the expression:

$$\Delta_i = 1.6 \times 10^{-13} N_i E_i \tag{5.10}$$

where E_i, expressed in MeV is the average energy of the i^{TH} emission, while N_i is the relative emission frequency. Its dimension is $Gy\,kg/Bqs$, and the product of the cumulative activity and the equilibrium absorbed dose constant is the radiation energy emitted by the i^{TH} emission during the time that radioactivity is present in a source tissue.

Then, the fraction of radiation energy E_i emitted within the source tissue r_S at time t that is absorbed in the target tissue r_T is given by the absorbed fraction $\phi(r_T \leftarrow r_S, E_i, t)$. The absorbed fraction depends on the amount of radiation energy hitting the target, on the volume and composition of the target tissue. Thus, the total energy absorbed by a specific target tissue is given by:

$$Absorbed\ Energy = \tilde{A} \sum_i \phi(r_T \leftarrow r_S, E_i, t)\Delta_i \tag{5.11}$$

Thus, the absorbed energy per mass unit over a defined dose-integration period T_D after administration of the radioactive material to the subject, that is the average absorbed dose to the target tissue r_T of mass $M(r_T, t)$ from the activity in a source tissue r_S is given as:

$$D(r_T \leftarrow r_S, T_D) = \int_0^{T_D} A(r_S, t) \frac{1}{M(r_T, t)} \sum_i \phi(r_T \leftarrow r_S, E_i, t)\Delta_i dt \tag{5.12}$$

Where the summation $\sum_i$ includes the values of $\phi(r_T \leftarrow r_S, E_i, t)$ and Δ_i for all the emissions of the radionuclide, and the values of $\phi(r_T \leftarrow r_S, E_i, t)$ for the source-target pair.

Dose assessment for penetrating radiations is a cumbersome task, especially when the radionuclide of interest is source for multiple emissions to be considered in the calculation. This problem has been simplified by the introduction of S-values [[50]]. The S-values represent the mean absorbed dose to a tissue target r_T per unit cumulated activity in the source target r_S:

$$S(r_T \leftarrow r_S, t) = \frac{1}{M(r_T, t)} \sum_i \phi(r_T \leftarrow r_S, E_i, t)\Delta_i \tag{5.13}$$

Where S has units of $Gy/Bq \cdot s$ and are are specific for a certain radionuclide and source-target combination. Thus, the average absorbed dose to the target tissue r_T from the activity in the source tissue r_S can be written as:

$$D(r_T \leftarrow r_S, T_D) = \int_0^{T_D} A(r_S, t) \cdot S(r_T \leftarrow r_S, t) \tag{5.14}$$

And finally the total absorbed dose to the target tissue from all the surrounding activity distributions, including that contained in the target tissue itself ($T = S$), as:

$$D(r_T, T_D) = \sum_{r_S} \int_0^{T_D} A(r_S, t) \cdot S(r_T \leftarrow r_S, t) \tag{5.15}$$

5.1.3 MIRD Organ S-values Limitations

S-values are calculated with different computational methods (assuming local energy deposition, by convolution or Monte Carlo) for each radionuclide and source-target pair.

In MIRD Pamphlet No. 11 [[50]], the S-values are determined at an organ level, meaning by considering the target tissue r_T and the source tissue r_S as whole organs. This computation, though, comes at the cost of strong assumptions that lead to meaningful approximations:

- The activity distribution in the source organ is considered to be uniform;
- The computed dose is an average over the whole target organ;
- Below $10\,keV$ and when the source and target are not the same, the absorbed fraction values ϕ for photons are extrapolated linearly to zero as energy decreases to zero, and when the source and target coincide, ϕ values are linearly extrapolated to unity as energy decreases to zero.
- The organs' shape, dimension and collocation are that of a standard human body model of defined body mass, and the scaling for the actual weight of the patient may lead to further approximations.

Furthermore, the dose calculation to tumor lesions is based on the sphere model in standard calculation softwares based on the MIRD S-values at the organ level such as OLINDA/EXM. The sphere model assumes tumor lesions that accumulate radionuclides to have a spherical shape and to have a uniform distribution of activity.

These limitations make so that the MIRD S-values at the organ level grant a computation

of the average absorbed dose to organs in order to monitor the therapy, but do not allow an image-based, thus a patient-specific, dosimetry.

5.2 Voxel Dosimetry

Voxel dosimetry is defined as the calculation of radiation absorbed dose in voxels, meaning to tissue regions with dimensions ranging from a few centimeters to hundreds of micrometers. As the name suggests, voxel dosimetry is commonly associated with tomographic imaging for activity quantification such as SPECT.

In radionuclide therapy, the activity distributions defined as source regions may be segments of individual tumors or organs. Both the tumor lesions and healthy tissue acquire nonuniform distributions of activity due to the kinetics of the radiopharmaceutical (delivery, uptake, site-specific binding and clearance) leading to a nonuniformity of the dose deposition. Non damaged parts of the target deriving from these nonuniformities may lead to a regrowth of tumor cells. The mean absorbed dose to the tumor cannot provide such information: a specific knowledge of the dose deposition distribution may thus be crucial for the evaluation of clinical results. Thus, in Pamphlet 17 [[51]] MIRD introduced the formalism for the adaptation of the schema to the voxel level.

5.2.1 Direct Monte Carlo Radiation Transport

A first approach for the calculation of the dose deposition at a voxel level is through Monte Carlo codes.

In radiopharmaceutical therapy information about the spatial distribution of absorbed dose is critical for assessing potential efficacy on tumor lesions and toxicity to organs. Thus, anatomic and functional variations among patients require patient-specific absorbed dose calculations. Variations in patient geometries consist of organs' shape, size, and relative distances. These characteristics are reproduced by the distributions of the physical density ρ

and the atomic number Z inside the patients' body. The ρ distribution influences the particles transport, while Z affects the number of low-energy photoelectric interactions. Functional variations consist in the patient-specific injected radiopharmaceutical uptake that results in peculiar spatial distribution of the radionuclide, not always approximable to a uniform distribution activity inside the organ of interest.

A Monte Carlo dosimetry method can precisely consider ρ and Z variations as well as the actual activity spatial distribution by simulating particle transport and recording the energy deposition. Specifically, a SPECT array can be used to determine the number of radioactive emissions at each array voxel while the emission transportation can be computed across a CT density array.

Several Monte Carlo codes exist that allow the transport of photons and electrons in user-defined geometries. Version 4 of the EGS4 transport code system and Version 4B of the Monte Carlo N-Particle transport code system (MCNP) have been used and validated for this purpose [[53], [54]].

5.2.2 Voxel S-values Approach

Another approach to voxel dosimetry allows the application of the MIRD formalism to quantitative data on nonuniform distributions of activity within target organs, suborgan regions and tumors, and is explained in Mird pamphlet n.17 [[51]].

Through sequential scans after the radiopharmaceutical administration, cumulated activities per image voxel (or groups of voxels) may be determined. Thus, by providing S-values that correspond to the voxel geometry of the imaging data, a dose calculation at the voxel level may be performed . As shown in Equation 5.16 below, the MIRD schema may be applied in a three-dimensional array summation to assess the dose to a given target voxel k from N surrounding source voxels h (including dose contributions from the target voxel itself, h = 0) [[51]]:

$$\overline{D} = \sum_{h=0}^{N} \tilde{A}_{voxel_h} \cdot S(voxel_k \leftarrow voxel_h) \tag{5.16}$$

A voxel S-value is defined as the mean absorbed dose to a target voxel per radioactive decay in a source voxel, both of which are contained in an infinite homogeneous tissue medium. As a result, this method may lead to errors in body regions with tissue-air or tissue-bone interfaces. Furthermore, the method does not account for variations in atomic number throughout a tissue region that may influence the distribution of dose delivered by low-energy photons. Nevertheless, the voxel S-value approach offers a convenient and rapid tool for voxel-scale dosimetry studies in a manner analogous to MIRD calculations at the level of whole organ dosimetry. Moreover, the use of voxel S-values avoids the need to perform time-consuming computations with the direct Monte Carlo radiation transport and qualifies as a useful tool for clinical use.

5.3 Conclusions

The MIRD formalism allows to compute the absorbed dose to a target region (organ or voxel).

When using the MIRD S-values at the organ level, the complex and cumbersome procedure of estimating the absorbed dose to the tissue of interest is reduced to that of calculating the S-values for each couple of source and target organ. This is done, though, at the cost of computing an average dose that assumes both the source activity distribution and the target dose absorption as uniform.

The MIRD formalism adapted to the calculation of absorbed dose at the voxel level: by considering both the source and the target as single voxels, one can overcome the strong assumptions of uniformity brought by the S-values at the organ level. The voxel S-value approach offers a convenient and rapid tool for voxel-scale dosimetry and avoids the need to perform CPU-intensive calculations, but cannot take into account for inhomogeneities in the attenuation map.

Direct Monte Carlo radiation transport is another possible solution. It offers a generalized method for handling tissue inhomogeneities and for assessing their influence on the resulting dose distributions, and can take into account disuniformities in the activity concentrations.

Though, it requires time-consuming CPU-intensive computations.

The description of the different absorbed dose calculation methods brought in this chapter completes the characterization of the whole dosimetric procedure. As a brief summary, the procedure starts with the image acquisition (Chapter2) of the patient after the radiopharmaceutical administration and its reconstruction (Chapter3) into three-dimensional maps. The images are then quantified (Chapter4), meaning the acquired counts information is converted into activity value, and finally the activity values are used for the absorbed dose calculation.

In the next chapters, the original work will be presented. Specifically, the next chapter will focus on the use of Monte Carlo codes for imaging purpose through the modelling of a Siemens Symbia Intevo Excel SPECT/CT scintillation camera.

Chapter 6

Monte Carlo modelling

Monte Carlo simulation in Nuclear Medicine is a powerful tool for modelling many physical phenomena which are difficult to track or to measure directly. MC simulation in imaging is particularly suitable for optimizing the quantification of activity in a patient, and, consequently, the absorbed dose to each organ. To do so, it is mandatory validate MC results with real data acquired with gamma camera. In this chapter the validation of SIMIND Monte Carlo code is presented for modelling a Siemens Symbia Intevo Excel SPECT-CT gamma camera both for ^{99m}Tc and ^{177}Lu.

Phantom experiments using ^{99m}Tc and ^{177}Lu have been performed with the purpose of measuring spatial resolution, sensitivity and to evaluate the calibration factor (CF) and recovery coefficients (RC) from acquired data. The geometries used for 2D planar imaging were (1) Petri dish and (2) capillar source while for 3D volumetric imaging were (3) a uniform filled cylinder phantom and (4) a Jaszczack phantom with spheres with different volumes. The experimental results have been compared with the results obtained from Monte Carlo simulations performed in the same geometries.

6.1 Background

In modern nuclear medicine, the absolute quantification of SPECT images are fundamental for providing an estimate of the activity uptakes in various organs and tissues for the purpose of diagnostic assessments and therapeutic decisions. Monte Carlo (MC) simulation is a tool

widely used to model real life systems, including nuclear medicine devices [[55]]. Starting from the description of particles interaction with matter, by using probability density functions (pdfs) and with the help of random number generators and sampling techniques, MC provides the opportunity to analyze the physics phenomena responsible for images formation with the aim of optimizing the data acquisition and processing steps. Due to the approximation and the simplification used in the description of physics laws inside a MC code, a mandatory step is the validation of MC model (code) before using it to simulate real world systems, in particular as a clinical simulator for SPECT imaging. To validate a MC code, outputs of simulated experiments are compared against results obtained from real measurements on the physical system. The validation ensures that the simulated system truly represents the physical one.

In this work, a Siemens Symbia Intevo Excel SPECT/CT scintillation camera has been modelled by using the SIMIND Monte Carlo Program (version 6.1) [[56]]. Planar and tomographic studies have been performed for two radioisotopes: ^{99m}Tc the most used radionuclide in SPECT/CT imaging studies, and ^{177}Lu an attractive radionuclide used for for peptide receptor radionuclide therapy (PRRNT) using the theranostic approach [[57]]. The recent progress in SPECT/CT instrumentations has allowed more accurate quantitation of SPECT studies: quantitative imaging is necessary when the absolute value of activity must be known for example in standard uptake value (SUV) measurement or in dosimetry applications [[58]].

The absolute activity quantification consists in several steps: the first one is to reconstruct projection images, taking into account photon attenuation, scatter and CDR (Collimator Detector Response). CDR is one of the most degrading factors in SPECT imaging [[28]]. It is caused by several factors: photons which pass through the holes' septa and photons which, despite the scattering with hole septa, are been detected. For modeling the scanner CDR one can use a capillary source placed at several source-to-detector distances while keeping the rotation angle fixed [[43]]. Usually, the Gaussian + exponential function fits the measurements and the fit results are used to model the distance-dependent CDR. The second step is to convert the reconstructed counts per second into activity [in MBq] through a Calibration Factor (CF). Different camera calibration methods have been proposed for evaluating CF: some researchers use planar scans of a small source [] or of a petri dish (following NEMA protocol for camera sensitivity test) [[59]], other ones use tomographic scans of a very simple phantom, such as a large cylindrical phantom (to avoid Partial Volume Effect, PVE), with

Table 6.1: Decay characteristics of both ^{99m}Tc and ^{177}Lu; data from [[13]]

Isotope	Half-life	Main γ emission $E_\gamma[keV](I_\gamma[\%])$	Max β energy $E_{max}[keV]$
^{99m}Tc	6.01 h	140.5 (88.5)	436.2
^{177}Lu	6.65 d	112.9 (6.2) 208.4 (10.4)	498.3

a certain, known activity inside. The CF unit is cps/MBq and it should be computed for every radionuclide and collimator used. The last step is to compute recovery coefficient (RC) factors in order to correct for the PVE: for small volumes, measured activity appears to be distributed among a larger volume respect to the actual one; this may lead to an underestimation of the activity in the real volume (and, then, of the measured absorbed dose) and to a wrong volume estimation. This is due to blurring effect, caused by a finite spatial resolution. PVE can be estimated through phantom studies, using Jaszczak phantom with known volume spheres. The RC factors are equal to the ratio between the measured activity in each sphere and the true one and it is expressed in percentage; they will be used to correct the final activity inside each sphere. This procedure has been performed both for ^{99m}Tc and ^{177}Lu.

Final aim of the work presented in this chapter is to have a tool able to simulate accurately the activity distribution inside the patient body, in order to calculate the dose imparted to each organ from the reconstructed activity distribution and finally to compare the imparted dose with the dose calculated from the true distribution so as to implement patient-specific dosimetry.

6.2 Materials and Methods

The study presented in this chapter is composed of two parts: experimental data acquisition and Monte Carlo simulations. In each part both ^{99m}Tc and ^{177}Lu radioisotopes are studied, for a total of 40 experimental scans and 140 simulation runs. The information about the isotopes' half-lives, their main gamma emissions and the maximum energy of their beta emission are summarized in Table 6.1.

The SPECT scanner used for the experimental measurements is a Siemens Symbia Intevo Excel, provided by Arcispedale di Cona (Ferrara, Italy). The Siemens Symbia Intevo Excel

Table 6.2: Main Symbia parameters, taken from Symbia Intevo data sheet

Crystal size	59.1×44.5
Crystal thickness	$9.5\,mm$
PMT total number	59
PMT array	Hexagonal
System resolution at $10\,cm$, $140\,keV$	$7.5\,mm$
Energy resolution at $140\,keV$	9.9%
Sensitivity at $10\,cm$, $140\,keV$	$202\,cpm/\mu Ci$
SPECT reconstruction matrix	128×128

is a SPECT/CT, a system with two gamma camera heads (3/8" or 9.5 mm) and a NaI scintillator crystal, with a 53.3x38.7 cm FOV. Acquisitions were performed using a 128x128 matrix, with a pixel size of 4.67 mm. The so-called "step and shot" technique was used for the tomographic studies. The CT was performed after the SPECT acquisition, with a 110 kV voltage and Care Dose 4D. The Symbia Intevo Excel was equipped with a Low Energy High Resolution (SY-LEHR) collimator for ^{99m}Tc studies and with a Medium Energy Low Purpose collimator (SY-MELP) for ^{177}Lu studies. The gamma camera parameters are listed in Table 6.2. A Mec Murphil MP-DC-Chamber dose calibrator has been used for the activity measurement. Activities have been assessed by performing five measurements of the syringes containing the isotopes, and then by subtracting the residual activity remaining in the syringes once emptied in the phantoms used for measurements. The ^{99m}Tc radioisotope has been obtained as sodium perthecnetate (Na[^{99m}Tc]O_4) from ^{99}Mo/^{99m}Tc generator (Ultratechnekow, CURIUM, Netherlands), while the ^{177}Lu has been obtained as lutetium chloride ([^{177}Lu]Cl_3) (EndoLucinBeta, ITM, Munich, Germany).

6.2.1 Phantom Experiments for ^{99m}Tc and ^{177}Lu: Planar Imaging

Planar measurements aim at the evaluation of the fundamental SPECT features: spatial resolution and sensitivity, which are defined by the scintillation crystal and the collimator. In order to characterize the main properties of the Symbia Intevo gamma camera's SPECT, one at a time the two heads have been exploited. The gamma camera data were acquired with a 15% energy window centered on the 140.5 keV for the main photopeak of the ^{99m}Tc, and with two 15% energy windows centered on the 113 keV and 208 keV photopeaks of the ^{177}Lu. All measurements have been repeated three times and performed with different distances between the source and the detector.

A capillary tube with an inner diameter of $1\,mm$ was used to determine the system spatial resolution. The tube was filled with $30 \pm 1\,MBq$ of a ^{99m}Tc solution and with a $130 \pm 7\,MBq$ of a ^{177}Lu solution. In order to study the spatial resolution, the tube was placed at three different distances from the front face of collimator for the experimental measurements: $10.0 \pm 0.5\,cm$, $25.0 \pm 0.5\,cm$ and $35 \pm 0.5\,cm$. The spatial resolution was measured by drawing a profile across the image of the capillary tube in three different positions in order to compensate for the possible non-uniformity in the tube filling. The line profile was fitted with a Gaussian function from whose full width at half maximum (FWHM) and the full width at tenth maximum (FWTM) were calculated. The reference value provided by SIEMENS for the extrinsic spatial resolution with a LEHR collimator and a capillary tube filled with a ^{99m}Tc source is $7.5\,mm$ at $10\,cm$.

A Petri Dish with an inner diameter of $10\,cm$ was filled with $25.0 \pm 1.3\,MBq$ of a ^{99m}Tc solution to a depth of $4 \pm 1\,mm$. The dish was placed on a low density block at a distance from the collimator front of $10.0 \pm 0.5cm$. Planar images were acquired in a 128x128 image matrix with a pixel size of 4.8x4.8 mm^2 until the total counts in the image exceeds 1 million. A background image was acquired for the same time after removing the radioactive source. A second Petri dish was filled with 30.0 ± 1.5 MBq of a ^{177}Lu solution, and planar images were acquired, as before, at the same distance. The total net counts over the detector's useful field of view (UFOV) was obtained and the sensitivity was calculated as follows:

$$Sensitivity\ [cps/MBq] = \frac{totalnetcounts}{activity\ (MBq) \cdot acquisition\ time(s)} \tag{6.1}$$

The reference value provided by SIEMENS for the sensitivity with a LEHR collimator and a Petri dish filled with a ^{99m}Tc source is $91.8\,cps/MBq$ at $10\,cm$.

6.2.2 Phantom Experiments for ^{99m}Tc and ^{177}Lu: Tomographic Imaging

A cylindrical Jaszczak SPECT Phantom (see Figure 6.1) deprived of the inner spheres has been employed to obtain the CF. The cylinder was filled with a $6800\,ml$ solution of distilled water, $350\,MBq$ of ^{99m}Tc.

Similarly, the uniform Jaszczak phantom was filled with a $6800\,ml$ solution of distilled water

Table 6.3: The lower and upper scatter windows for technetium and lutetium main peaks are listed.

Radionuclide	Main peak [keV]	PW range [keV]	LSW range [keV]	USW range [keV]
^{99m}Tc	140.5	123.9 - 151.4	103.2 - 123.9	Not used
^{177}Lu	113	102.7 - 119.4	86.1 - 102.7	119.4 - 128.2
^{177}Lu	208	189.3 - 220.0	168.8 - 189.3	Not used

(6720 ml), 2810 MBq of ^{177}Lu from a certificated vial with an accuracy of $\pm 10\%$, 67 ml of HCl (37%) added in order to make the solution the most homogeneous as possible and to avoid lutetium accumulation on phantom surfaces.

Both for ^{99m}Tc and ^{177}Lu, the SPECT/CT acquisitions were performed via the Siemens Symbia Intevo Excel with the step-and-shoot technique. Each tomographic acquisition consisted in 64 projections performed maintaining a constant distance of 25 cm between the centre of the cylinder and the lower part of the detector head. The acquisition time was 20 s for ^{99m}Tc, while it was 30 s for ^{177}Lu.

The reconstruction of the projected images was performed with the built-in software from the vendor, Siemens Flash3D. The OSEM 3D was the iteration reconstruction technique chosen, with X iterations and Y subsets. The Flash3D is capable of applying attenuation, scatter and CDR corrections.

The scatter correction for Technetium was performed via the DEW (Double Energy Windows) technique with the use of the PW (Peak Window) and the LSW (Lower Scatter Window). The scatter correction for lutetium was performed via the TEW (Double Energy Windows) method for the 113 keV peak and the DEW method for 208 keV peak; the widths of each photopeak window are reported in Table 6.3.

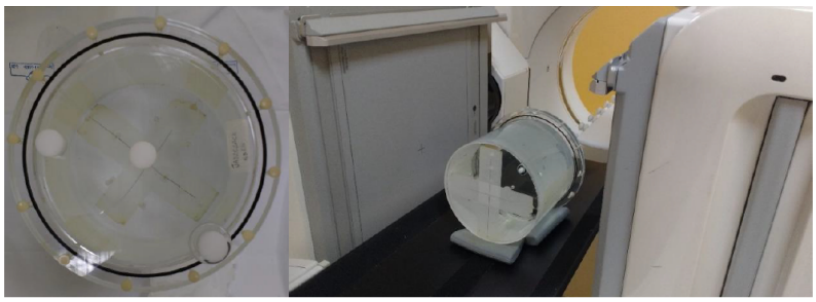

Figure 6.1: On the left, the uniform phantom is shown; on the right, the acquisition moment for ^{99m}Tc.

In order to obtain the RC (Recovery Coefficient) factors, the absolute quantification of ^{99m}Tc was performed via a Jaszczak SPECT Phantom with six hot spheres.

The phantom was placed in the centre of the field of view. Acquisitions were per- formed with

the same settings as those of the uniformly filled Jaszczack phantom previously described and conducted with 64 projections of 20 s scan time.
The energy windows are the same as those set for the CF evaluation and are listed in Table 6.3. The spheres volume and the background activity are listed in Table 6.4. Each activity value reported in Table 6.4 is the mean of five different measurements. The process of activity measurement consisted in several steps: first, the activity in the syringe was measured. Then, after the injection of the radionuclide into the spheres, the residual activity in the syringe was measured and subtracted to the initial value. Finally, the activity in the sphere was measured.

For the evaluation of the RC factors of ^{177}Lu a NEMA image quality PET phantom with five spheres of different diameters was used. Spheres diameters, volumes, injected activities and background activity are listed in the Table 6.5. Measurement settings are the same as those used for the CF evaluation and are listed in Table 6.2 and Table 6.3. The number of projections was 64, each of 30 s duration. The ratio between activity concentration in the background and the activity concentration in the spheres was not constant but ranged from 0.2% to 7% starting from the smallest sphere to the largest. Each value reported in this Table 6.5 is the mean of five different measurements, with an associated standard deviation of less than 1%. The process of activity measurement is the same as that described for the ^{99m}Tc. CT data have been used for the delineation of volume of interest (VOI) of each sphere in Symbia SPECT studies, while for SIMIND studies we used the geometric data for each sphere: 3D center coordinates and radius.

The exponential curve fitting the RC values was performed using the Igor software [new4: Igor Pro, version 4.01, Wavemetrics, Inc, 1988-2000, Oregon, USA]. RC data errors were evaluated by taking into account the Poissonian distribution of the SPECT acquired counts and the errors in activity measurement, volume and time interval estimation.

6.3 Monte Carlo Simulation for ^{99m}Tc and ^{177}Lu

Monte Carlo simulations have been performed via SIMIND v6.1. The Monte Carlo simulation code SIMIND is a photon-tracking program developed by Professor Michael Ljungberg (Medical Radiation Physics, Department of Clinical Sciences, Lund, Lund University, Sweden). SIMIND describes a standard clinical SPECT camera and provides projected images from

Table 6.4: The five spheres of the Jaszczack phantom with their respective ^{99m}Tc activity and the background are shown. Each of the value reported in this Table is the mean value of five different measurements, with a standard deviation less than 1%. These errors must be added to the 10% error on the Activity (certified by the producer).

Sphere Volume [ml]	Sphere Diameter [ml]	Activity [MBq]
0.5	9.8	4.8
1.0	12.4	4.4
2.0	15.6	4.5
4.0	18.9	4.7
8.0	24.8	4.7
16.0	31.2	4.6
Phantom Volume [ml]		Activity [MBq]
6800		131.7

Table 6.5: The six spheres of the NEMA PET phantom with their respective ^{177}Lu activity and background are shown. Each of the value reported in this Table is the mean value of five different measurements, with an associated error of less than 11%.

Sphere Volume [ml]	Sphere Diameter [ml]	Activity [MBq]
1.4	13.0	8.3
2.5	17.0	8.4
5.0	22.0	8.6
11.0	28.0	8.7
26.0	37.0	7.5
Phantom Volume [ml]		Activity [MBq]
6800		131.7

user defined attenuation map and activity distribution.

Both ^{99m}Tc and ^{177}Lu were studied via SIMIND: the main parameters set for the Monte Carlo simulations are listed in Table 6.6.

In SIMIND, we simulated all the planar and tomographic acquisitions reported previously, and we added the simulation of the system spatial resolution for distances from the source to collimator front-end ranging from 5 cm to 40 cm in 5 cm steps both for ^{99m}Tc and ^{177}Lu. These curves are useful to estimate the compensation for system spatial resolution in the reconstruction process. To obtain the three-dimensional studies, the projected images produced via SIMIND were reconstructed using CASToR (Customizable and Advanced Software for Tomographic Reconstruction [[60]]), an open-source toolkit for tomographic reconstruction for both emission and transmission exams. CASToR applies an iterative reconstruction technique, in particular an OSEM-3D with 10 iterations and 8 subsets was used including scatter and attenuation correction with a stationary PSF modelled as a 3D isotropic Gaussian.

Table 6.6: Table 6: Main parameters inserted in SIMIND's CHANGE program for horizontal cylinder ^{99m}Tc and ^{177}Lu filled.

	^{99m}Tc	^{177}Lu
Photon energy	140.5 keV	113 keV, 208 keV
Source type	Horizontal cylinder	Horizontal cylinder
Energy resolution	9.9% at 140.5 keV	9.9% at 140.5 keV
Intrinsic resolution	0.38 mm	0.38 mm
Photons per projection	10e7	10e7
Distance to detector (circular orbit)	25 cm	25 cm
Matrix sixe	128×128	128×128
Acceptance angle	45 deg	45 deg
Rotation mode	CW	CW
Rotation angle step	5.625 deg	5.625 deg
Number of projections	64	64
Collimator	Sy-LEHR	Sy-ME

Table 6.7: Comparison of measured planar System Sensitivity with Monte Carlo results. All parameters have been measured at distance of 10 cm from collimator.

		FWHM [mm]		FWTM [mm]	
Radioisotope	Main peake [keV]	Measured	Simulated	Measured	Simulated
^{99m}Tc	140.5	8.3 ± 0.8	7.8 ± 0.2	14.9 ± 0.9	14.2 ± 0.2
^{177}Lu	113.0	11.7 ± 0.4	11.3 ± 0.6	21.3 ± 0.7	20.6 ± 1.0
^{177}Lu	208.0	11.8 ± 0.6	12.4 ± 0.4	21.6 ± 1.2	22.0 ± 0.7

6.4 Results

6.4.1 Planar Spatial Resolution and Sensitivity

The measured and simulated planar system spatial resolution, stated as FWHM and FWTM, at a source-detector distance of 10 cm are reported in Table 6.7 both for ^{99m}Tc and ^{177}Lu.

Figure 6.2(top) shows the comparison between the experimentally measured and Monte Carlo calculated spatial resolution plotted as function of the source-detector distance for ^{99m}Tc. Figure 6.3 shows the data about the spatial resolution for the peaks 113 keV and 208 keV of ^{177}Lu as function of source detector distance. The simulated data are fitted with the curve suggested by Frey et al. [[61]]:

$$FWHM = \sqrt{(a \cdot D + b)^2 + c^2} \tag{6.2}$$

and the value of χ_r^2 is 0.72 for ^{99m}Tc, while the χ_r^2 values for the 113 keV and 208 keV peaks of 177 Lu are0.8 and 0.64 respectively.

In Table 6.8, the measured and the simulated sensitivity at a distance of source-detector of 10 cm both for ^{99m}Tc and ^{177}Lu are reported. Figure 6.2(bottom) shows the comparison

between the experimentally measured and Monte Carlo calculated sensitivity plotted as function of the source-detector distance for ^{99m}Tc, while Figure 6.4 shows the experimentally measured and Monte Carlo calculated sensitivity as function of source detector distance for the two peaks of ^{177}Lu. Even in this case, the experimental results are in good agreement with the simulated ones, apart from the 208 keV sensitivity: the experimental values are nearly 13.6% lower than those obtained with SIMIND.

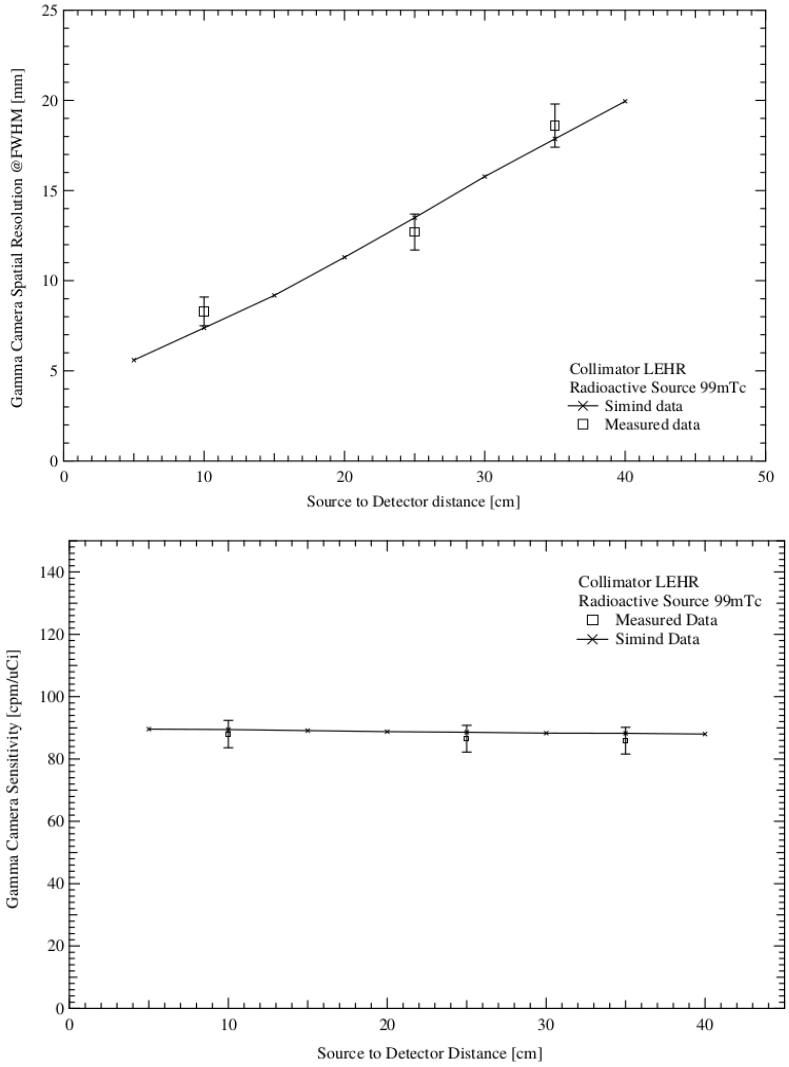

Figure 6.2: (top) Plot of spatial resolution as function of distance between source and detector for ^{99m}Tc. (bottom) Plot of sensitivity as function of distance between source and detector for ^{99m}Tc.

6.4.2 CF and RC for ^{99m}Tc and ^{177}Lu

As preliminary step, we compared the horizontal profiles of a uniform filled cylinder with the radionuclides used in this study, ^{99m}Tc or ^{177}Lu, measured experimentally with the Monte Carlo calculated ones. The horizontal profiles were obtained by drawing a line on a

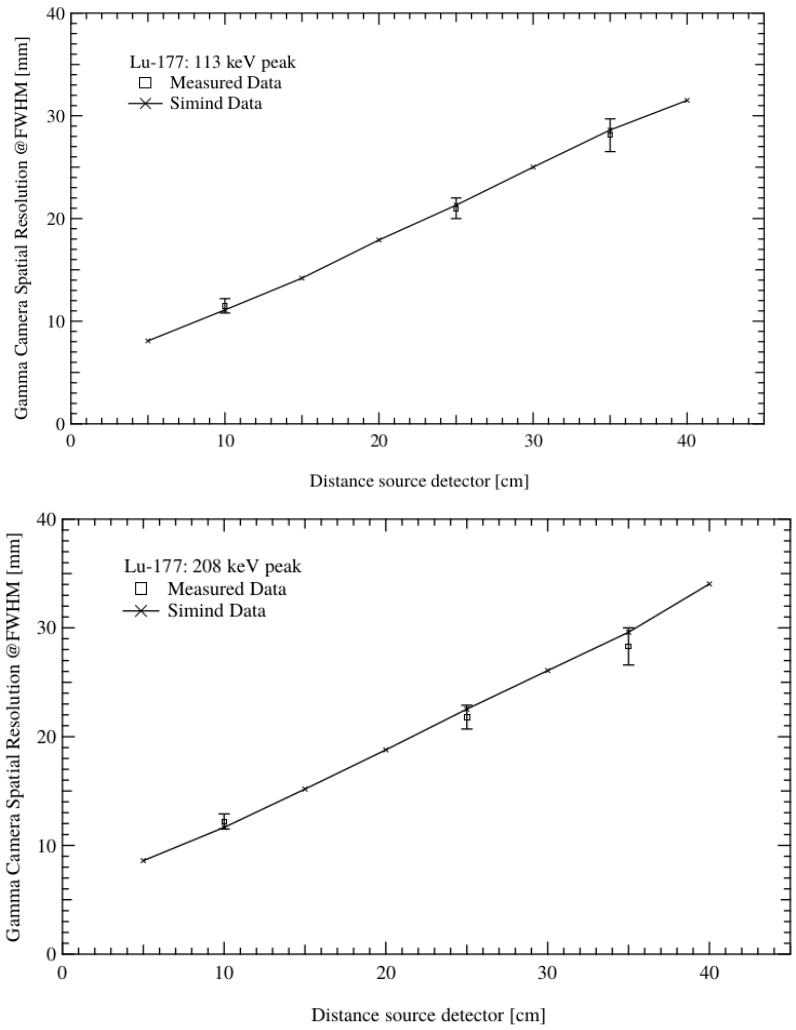

Figure 6.3: Plot of spatial resolution as function of distance between source and detector for ^{177}Lu: 113 keV peak (top), 208 keV peak (bottom).

cylinder projection at three different positions and calculating the mean value for each profile coordinate. Figure 6.5(left) shows the result for^{99m}Tc, while the Figure 6.5(right) shows the results for ^{177}Lu. The error bar associated with each position of the measured profile has been calculated as the square root of the counts associated with the position. Symbia Intevo CF has been evaluated for all the uniformity phantom acquisitions performed. Two cylindrical VOIs were used for CF evaluation: the type 1 VOI had linear dimensions 30% larger than those of the Jaszczak phantom but with the same geometrical centre, while the type 2 VOI had linear dimensions 30% smaller than those of the Jaszczak phantom but with the same geometrical

Table 6.8: Comparison of measured planar System Sensitivity with Monte Carlo results. All parameters have been measured at distance of 10 cm from collimator.

Parameter	Radioisotope	Main peak [keV]	Experimental [cps/MBq]	Simulated [cps/MBq]
Sensitivity	^{99m}Tc	140.5	88.0 ± 4.4	89.4 ± 0.5
Sensitivity	^{177}Lu	$113.0 + 208.0$	19.5 ± 1.0	20.6 ± 0.4

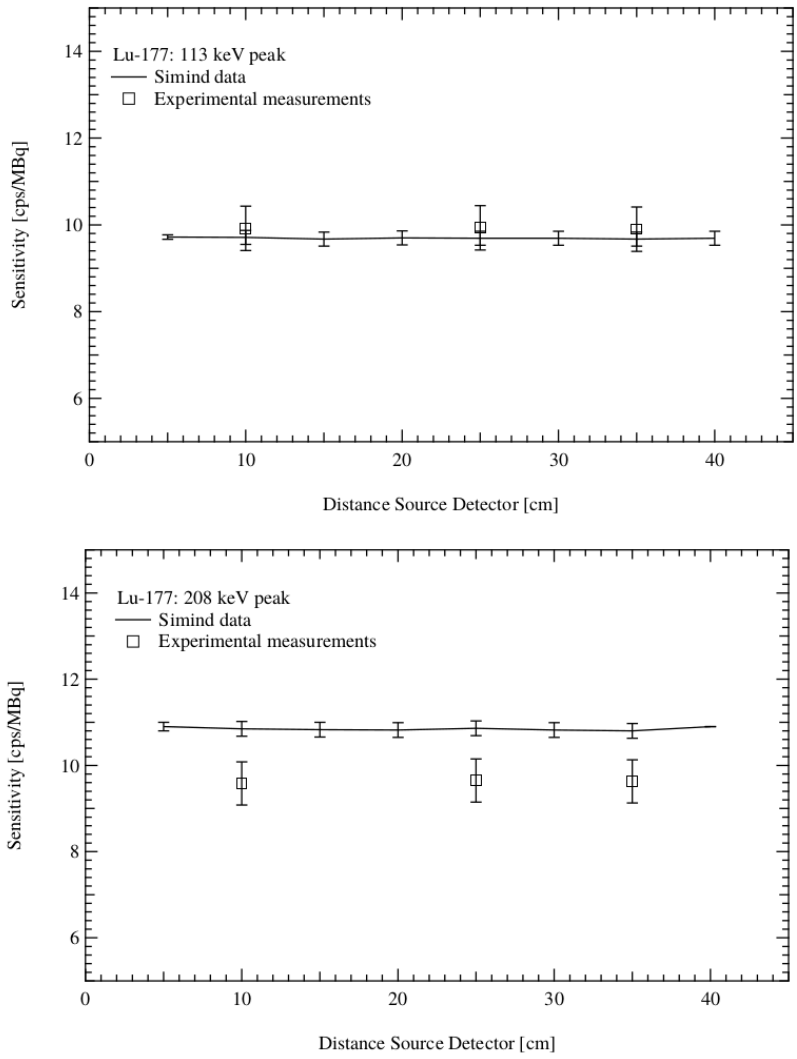

Figure 6.4: Plot of sensitivity as function of distance between source and detector for ^{177}Lu: 113 keV peak (top), 208 keV peak (bottom).

centre. Figures 6.6a) and 6.6b) show transverse and coronal slices of the reconstructed Jaszczak phantom, respectively, together with VOI type 1. Figures 6.6c) and 6.6d) show transverse and coronal slices of the reconstructed Jaszczak phantom, respectively, together with VOI type 2. Figure 6.7 shows the transverse slices of the reconstructed Jaszczak phantom, without and with spheres, both for ^{99m}Tc and ^{177}Lu.

The errors associated with results take into account:

- the Poisson distribution of the counts;
- errors in the evaluation of phantom volume;
- error in activity evaluation through the calibrator (standard deviation of the measurement of the syringe samples, but also the systematic error of the calibrator itself);

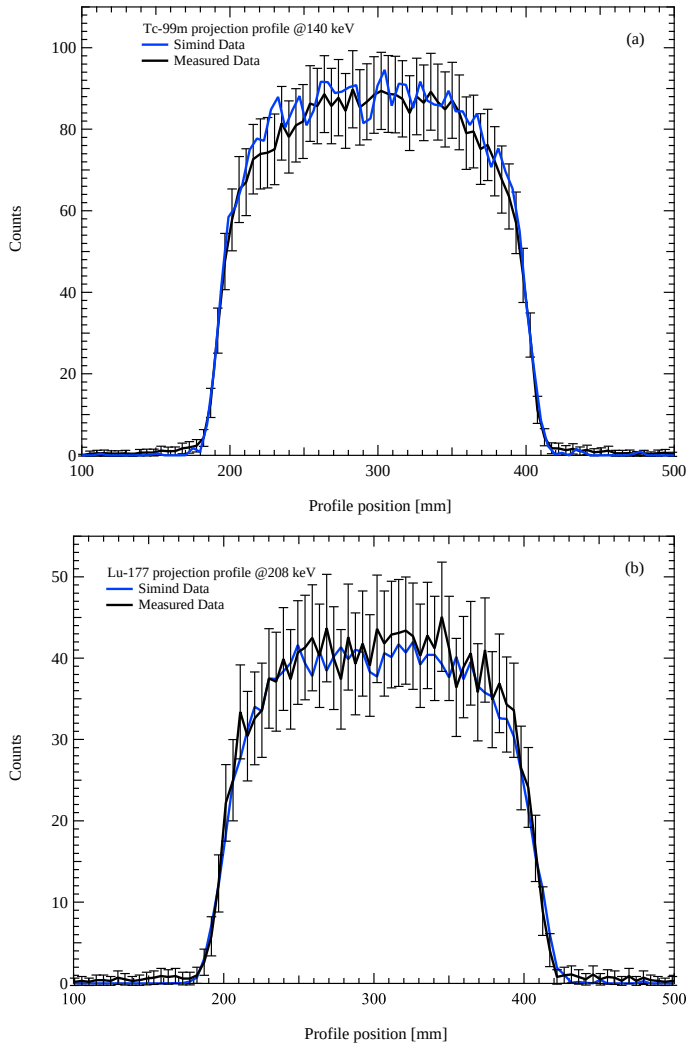

Figure 6.5: Horizontal profiles obtained by drawing a line on a cylinder projection at three different positions and calculating the mean value for each profile coordinate for ^{99m}Tc (left) and ^{177}Lu (right).

- the standard deviation of the VOIs volume values;
- error in time interval evaluation.

The ^{99m}Tc calculated CF value for the type 1 VOI was 110.1 ± 5.5 cps/MBq for experimental data while for SIMIND data the calculated value was 107.3 ± 0.3 cps/MBq. The CF value calculated for the type 2 VOI were 111.8 ± 5.6 cps/MBq and 113.8 ± 0.5 cps/MBq respectively for experimental and simulated data. In Figure 6.8, the RC experimental values for ^{99m}Tc are compared with the RC values obtained by using Monte Carlo simulation and reconstructed by CASToR software. To partially compensates for the CDR, a 2D Gaussian distribution has been used in the reconstruction process of the simulated data. The Gaussian FWHM has been chosen calculating the average distance of radioactive distribution inside the Jaszczak phantom from the collimator face, and selecting the corresponding FWHM value from Figure 6.2 (top).

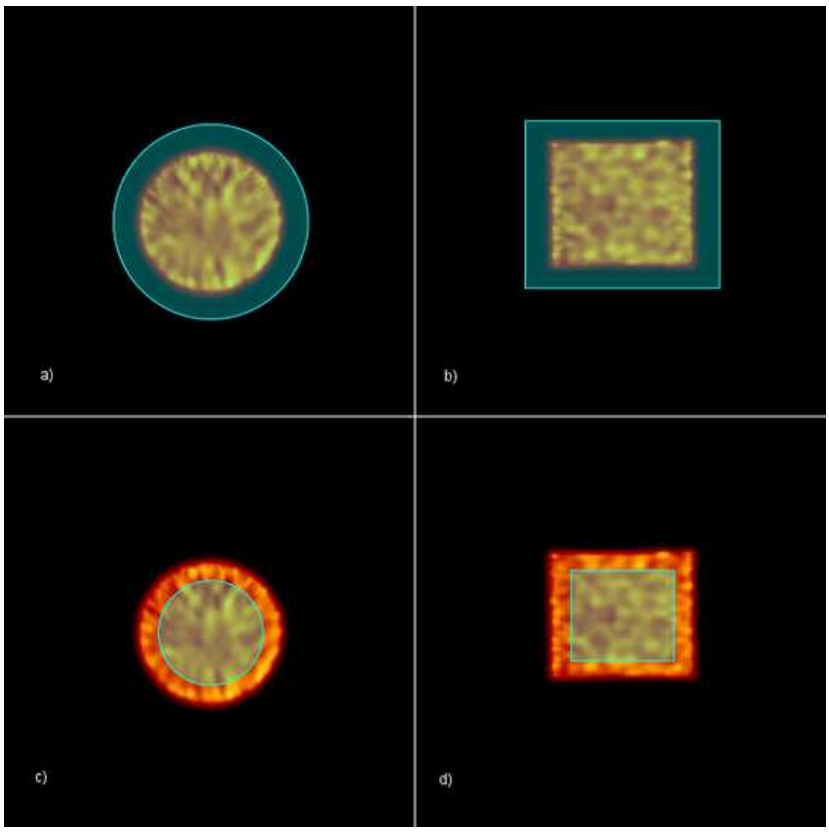

Figure 6.6: Transverse (a) and coronal (b) slices of the reconstructed Jaszczak phantom together with VOI type 1. Transverse (c) and coronal (d) slices of the reconstructed Jaszczak phantom together with VOI type 2.

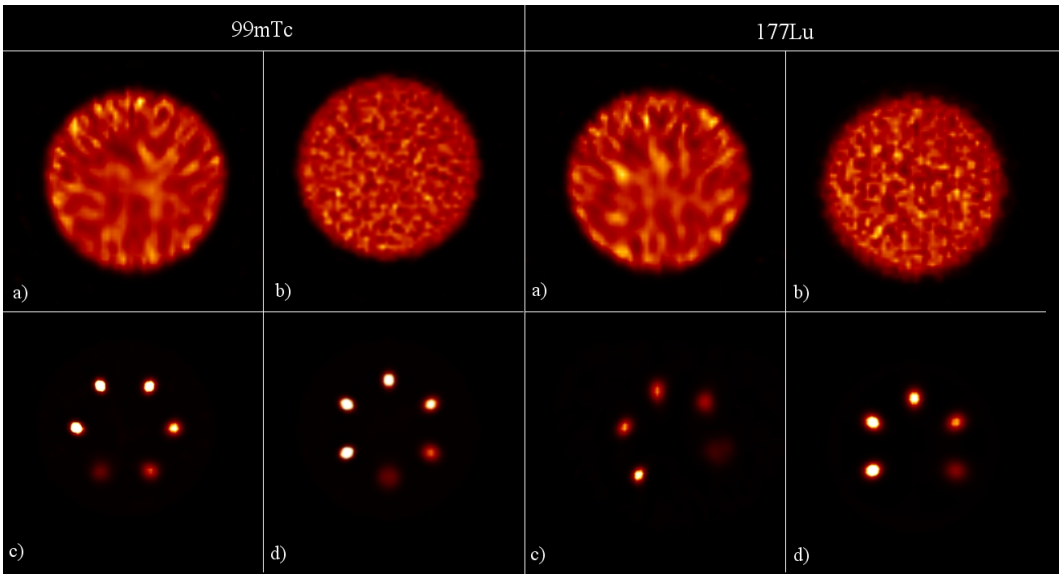

Figure 6.7: Transverse slices of the reconstructed Jaszczak phantom, without and with spheres, both for ^{99m}Tc and ^{177}Lu.

Jentzen et al. [[62]] suggest to fit the RC data with a sigmoid curve, that is a function of the sphere diameter D:

$$RC = \frac{a}{1 + b \cdot e^{-c \cdot D}} \tag{6.3}$$

and the fitting curve is the dashed line on the plot. The χ^2_r value of fit procedure was 0.9.

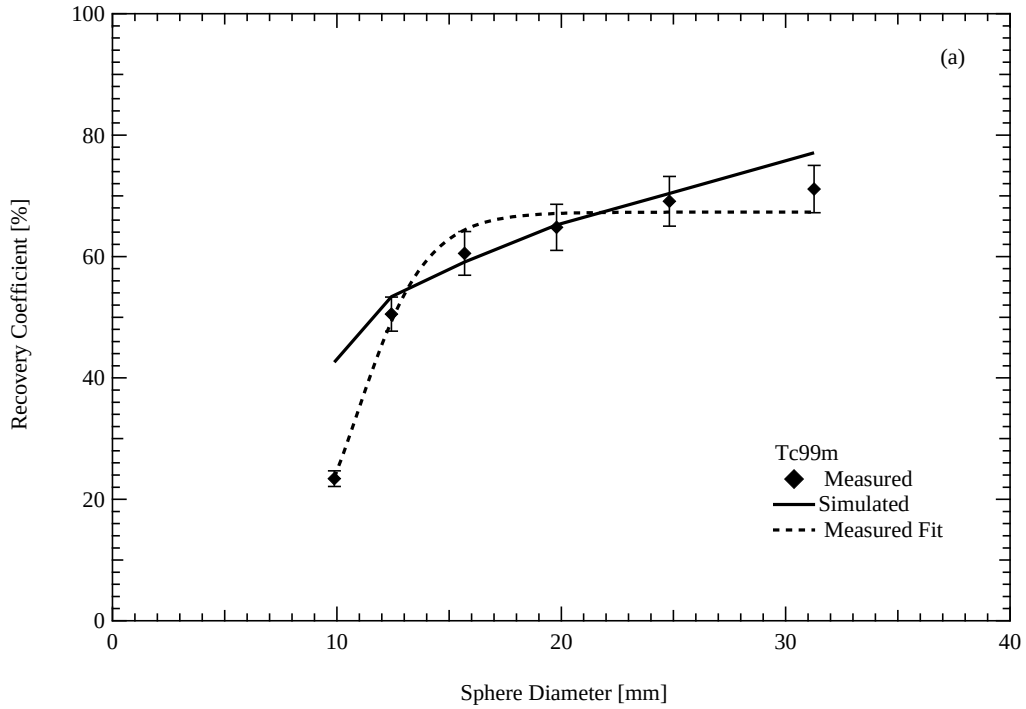

Figure 6.8: Transverse slices of the reconstructed Jaszczak phantom, without and with spheres, both for ^{99m}Tc and ^{177}Lu.

In order to obtain the CF factor for ^{177}Lu, the previous procedure has been repeated and allowed us to calculate the $CF = 18.3 \pm 1.0$ cps/MBq for type 1 VOI, while the $CF = 18.6 \pm 1.0$ cps/MBq for type 2 VOI. The same uniformity phantom acquisitions have been repeated with SIMIND, in order to find CF for lutetium; it is important to underline that CASToR can reconstruct studies taking into account only one peak at time. So, two different values for CF (one for the peak at 113 keV and one for the peak at 208 keV) have been obtained. Usually, 208 keV peak is routinely used for dosimetry studies because of the low scattering/down scattering contribution, but the patient acquisition protocol for ^{177}Lu used in Ferrara Hospital collects and reconstructs the data of both 113 keV and 208 keV peaks, so the calculated $CF = 20.4 \pm 0.7$ cps/MBq for the type 1 VOI, while the $CF = 21.4 \pm 1.3$ cps/MBq for type 2 VOI. The RC coefficients have been evaluated from 1.4 ml to 26 ml, using spheres filled with lutetium and the experimental and simulated data are in Figure 6.9 with the fitting curve as dashed line. The χ^2_r r value of fit procedure was 0.17.

6.4.3 Discussion

The FWHM and FWTM values of the system spatial resolution for the experimental and simulated capillary planar images show a good agreement. The FWHM percentage difference is of 6% for ^{99m}Tc, while the FWHM percentage differences are 3.4% for 113 keV peak and

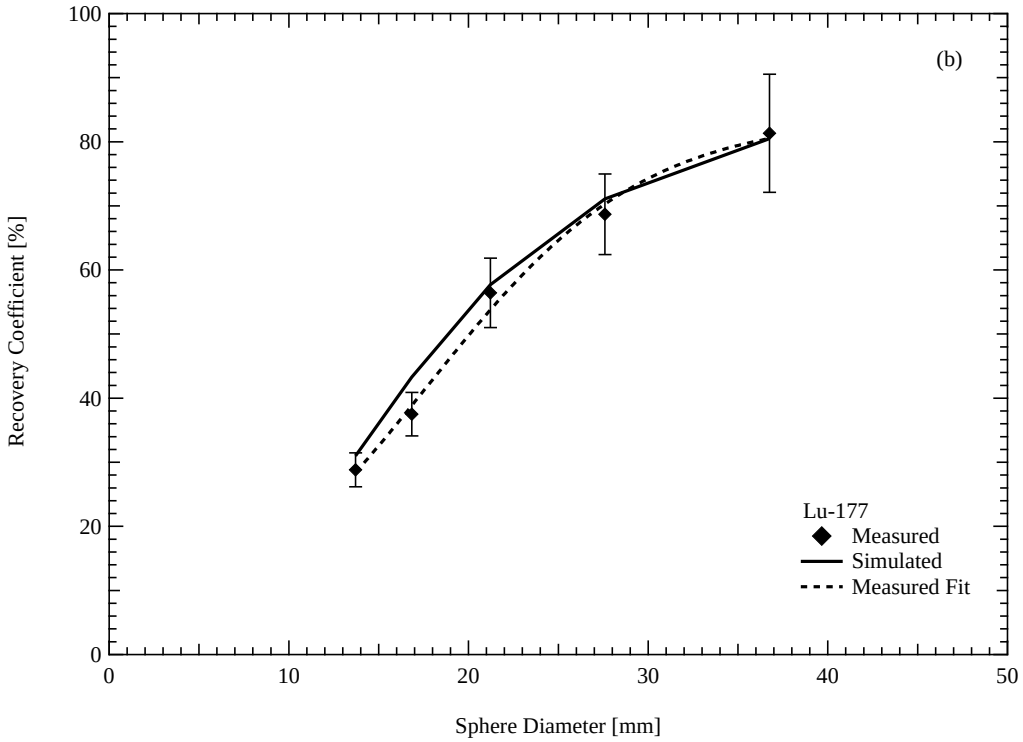

Figure 6.9: Transverse slices of the reconstructed Jaszczak phantom, without and with spheres, both for ^{99m}Tc and ^{177}Lu.

-5% for 208 keV peak of ^{177}Lu. The results in this study correspond to the findings by Toossi et al. [[63]] for ^{99m}Tc. They reported values of $8.4 \pm 0.1\ mm$ and $7.8 \pm 0.1\ mm$ for measured and simulated FWHM, respectively. For the 208 keV peak of 177 Lu, Ramonaheng et al. [[64]] reported a value of $11.5 \pm 0.35\ mm$ for measured value, in agreement with the findings in this study.

The results obtained for the system sensitivity acquired in planar imaging show an excellent agreement with the simulated data except for the 208 keV peak of ^{177}Lu. Here, the value calculated using the MC simulation is 13.6% higher than the experimentally measured value. A possible explanation of this difference is how the energy resolution is modelled in SIMIND [[65]]. Starting from the measured energy spectrum acquired during the sensitivity measurement, it was calculated by fitting procedure the energy resolution for the 140.5 keV peak of 99m Tc, and for the 56.1 keV, 113 keV and 208 keV peaks of ^{177}Lu. Figure 6.10 shows the measured energy resolution as a function of peak energy, the curve calculated by the $1/\sqrt{E}$ model and the curve fitting with the Hakimabad model [[**?**]]. Comparing the energy resolution values for the ^{177}Lu predicted by the model $1/\sqrt{E}$ with the experimental ones, the plot shows in the experimental energy resolution a decrease of 1% for the 113 keV peak and an increase of

1% for the 208 keV peak respect to the values predicted by the $1/\sqrt{E}$ model. Consequent of this change in energy resolution, it is expected an increase in counts under the 113 keV peak and a decrease in counts under the 208 keV peak. To estimate the variation, we simulated with SIMIND two acquisitions, on a Petri disk, with a fixed energy resolution: for the first simulation the energy resolution was that measured at 113 keV peak, for the second simulation the energy resolution was that measured at 208 keV. Analysing the simulated spectra and calculating the area under the peaks, it was possible to estimate an increase of 4% events recorded at the 113 keV PW and a decrease of 5% events at the 208 keV PW. Then, the results given in table 8, for the ^{177}Lu simulated sensitivity, will change from 9.7 cps/MBq to 10.1 cps/MBq for the 113 keV peak and from 10.9 cps/MBq to 10.36 cps/MBq for the 208 keV peak. The remaining difference respect to the measured values could be due to the uncertainty on ^{177}Lu activity.

Ramonaheng et al. [[64]] have reported for the 208 keV peak of ^{177}Lu the experimental and MC (SIMIND) simulated value of 10.0 ± 0.3 cps/MBq and 10.3 cps/MBq, respectively. Both values compare well with the results in this study.

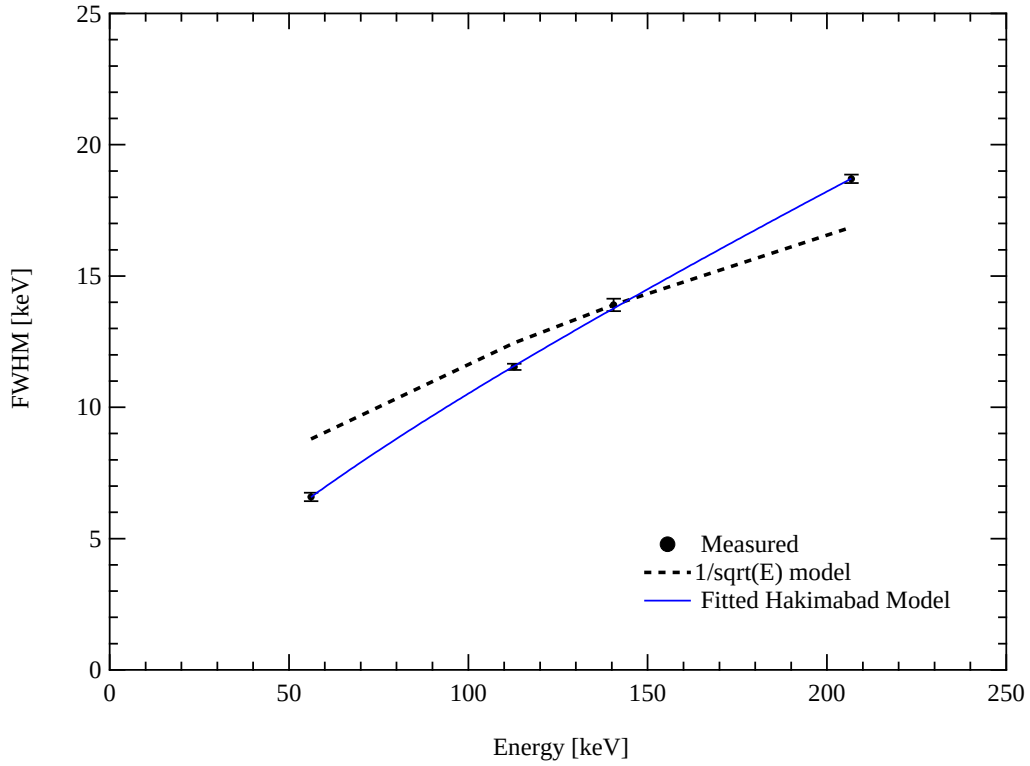

Figure 6.10: Transverse slices of the reconstructed Jaszczak phantom, without and with spheres, both for ^{99m}Tc and ^{177}Lu.

The parameters acquired in tomographic mode, CF and RC, require a further step to be calculated: tomographic reconstruction using appropriate software. Usually, an iterative

reconstruction algorithm is used for SPECT reconstruction that allows to include the following three contributions in the projection operator: the collimator response function, the contribution of scatter and the contribution of tissue attenuation. Thus, the parameters calculated from the reconstructed images depend on how correct the estimate of the three contributions is.

As it was observed by Zhao et al. [[66]] CF value calculated by a tomographic study is higher than that determined by planar scan. Additionally, the same authors stated that the scatter correction evaluated by DEW or TEW method could introduce error in the calculation of CF value, and the error depends on source distribution inside the phantom or the patient. Peters et al. [[67]] reported for ^{99m}Tc an experimental value for CF of 112 cps/MBq for a Symbia Intevo 6 in very good agreement with our result.

To estimate the RC curve using the simulated data with SIMIND, we have calculated an average gamma camera spatial resolution averaged over the activity distribution. In fact, the software CASTOR at the moment allows inclusion of a Gaussian collimator response function not dependent on the distance. For ^{99m}Tc the selected FWHM was 11.1 mm, while for ^{177}Lu the average values were 21.4 mm and 22.5 mm for 113 and 208 peak, respectively. Simulated RC for ^{99m}Tc agrees well with the experimental value, but the maximum value of RC is nearly of 70% for a sphere diameter of 31.6 mm. Zeintl et al. [[32]] reported a value of 80% for the same sphere diameter. By increasing the number of iterations, it is possible to obtain better RC values. Simulated RC for ^{177}Lu are in excellent agreement with the experimental one, the maximum value of RC being 80% for a sphere diameter of 37 mm. Sanders et al. [[33]] report a maximum RC value of 78% for a sphere diameter of 31.6 mm. Zeintl et al. [[32]] have analysed the change in RC values as a function of background-sphere ratio for 16 ml sphere. The RC value changes starting from 76% to 78% if the background-sphere ratio is less than 10%. If this result were still valid for the smaller spheres, the curves calculated in this study would not be different from those obtained with a constant background-sphere ratio less than 10%.

6.5 Conclusions

In this study, we have verified a modelled Symbia Intevo Excel by comparing the system resolution and the system planar sensitivity both for ^{99m}Tc and ^{177}Lu. Then, we have validate the the calibration factor (CF) and the recovery coefficient (RC) derived for a Monte Carlo

(MC) modelled gamma camera by comparing results from physical measurements with the gamma camera to simulations with SIMIND for the isotope-collimator combinations ^{99m}Tc-LEHR, ^{177}Lu-MELP. Results show that appropriate corrections like attenuation, scatter and collimator detector response are essential when activity quantification is needed. Additionally, the results suggest to optimise the OSEM iterative reconstruction in terms of iterations and subsets for quantitative SPECT imaging with therapeutic radionuclides, even if the combination of iterations and subset used in this study is defined in the standard clinical protocol for internal therapy with ^{177}Lu. Overall, it has been shown that SIMIND is a useful tool to simulate gamma cameras, using several radionuclides for different purpose both in the diagnostic and therapeutic fields.

Chapter 7

Neuroendocrine Tumors and Targeted Radionuclide Therapy

Neuroendocrine tumors (NETs) are relatively rare and heterogeneous tumor type arising from the diffuse neuroendocrine system [[15], [16]], whose incidence has increased in the last years also thanks to the improvement of diagnostic techniques and to the deep knowledge of the pathology [[17], [18], [19]]. Peptide Receptor Radionuclide Therapy (PRRT), introduced more than 20 years ago, represents an important option approach that have expanded considerably. Since the majority of NETs show an abundance of the somatostatin receptors, PRRT uses radiolabeled somatostatin analogues to target the somatostatin receptors on neuroendocrine tumor cell surfaces [[20]]. For what concerns the radioisotopes interested in the treatments, ^{177}Lu is an attractive radionuclide for several reasons: the possibility of labelling of biomolecules (used for tumor targeting), its favorable decay characteristics, its concentrated energy deposition, low energy beta emissions, its half-life and its two main gamma rays emitted (whose energies lead to imaging). Recent advances in MRT have led to a new somatostatin analogue, the DOTA-DPhe1-Tyr3 - octreotide, better known as DOTATOC, which has shown to have high affinity for somatostatin receptors.

PRRT may be prescribed either using fixed activity or personalized activity based on the results of dosimetry. The fixed activity administration regimen does not consider for the individual differences in bio-distribution and resulting toxicities are neglected. On the contrary, it has been demonstrated that individualized treatment protocols have the potential to maximize the absorbed doses delivered to disease sites and to improve treatment outcome

[[71], [20]]. An accurate knowledge of radiation absorbed doses could help in planning a specific therapeutic regimen and might also help in predicting those patients who would benefit the most from treatment and in identifying patients with unfavorable dosimetry [[72], [73]]. Moreover, dosimetry is gaining increasing importance as also established by the European Union Regulation that requires an individualized dose calculation for nuclear medicine treatments [[74]].

Kidneys and bone marrow (BM) toxicities are the dose limiting factor in PRRT [[75]]. All the radiopharmaceuticals used for PRRT have shown high renal activity concentration [[76]] highlighting the necessity to monitor potential toxicity to the kidneys especially for ^{90}Y-treatment [[77]]. For the majority of protocols, the maximum accepted dose to the kidneys is 23 Gy when PRRT is administered as 3 or 4 fractions at intervals of 8-10 weeks [[78]]. Bodei et al. [[79]] have reported a limit of 28 Gy for biological effective dose (BED) for patients with risk factors, such as hypertension and diabetes, while patients with no risk factors might have a renal BED threshold of 40 Gy. BM toxicity results from irradiation of haematopoietic tissue, and a maximum absorbed dose of 2 Gy to the BM is generally accepted. Among the different existing methodologies for calculating the BM dose, a large number of studies agree in addressing the lumbar vertebrae imaging method as a solid procedure for absorbed dose evaluation [[80], [81], [82]]. Avoiding both kidney and BM toxicities is of highly importance in particular for patients whose life expectancy is relatively long [[79], [83]].

Even though an accurate knowledge of the absorbed dose to organs at risk would allow a more precise therapy, several treatment plans still involve the administration to the patient of a standard activity. The awareness of the administered activity is not an adequate predictor of the absorbed dose to tumor lesions and organs at risk. This circumstance is due to the inter-patient variability in the pharmaceuticals' uptake and retention.

The phase II study (FENET 2016) routinely applied at University Hospital S. Anna (Ferrara, Italy) aims at improving tumor responses by using different radionuclides in combination. Treatment protocol relies on either five PRRT cycles with ^{177}Lu-DOTATOC (MONO) or a sequence of ^{177}Lu interspersed with ^{90}Y-DOTATOC (DUO) administrations spaced two months apart.

In this chapter is reported the study of tumors and organ-at-risk (OAR) dosimetry, focusing on OARs and tumors kinetics and to the differences between the two different radiolabeled peptides, in patients treated with PRRT using a simplified but patient-tailored dosimetric approach.

7.1 Protocols and Patients

The FENET 2016 is a phase II perspective experimental protocol approved by AIFA (EUDRACT code number 2016-005129-35). The protocol includes patients affected by various forms of NET (gastroenteropancreatic, bronchopulmonary, etc.) having measurable lesions according to the RECIST 1.1 criteria via CT imaging and high somatostatin receptors expression of tumor lesions evaluated through 68Ga-DOTATOC PET/CT study.

The treatment is based on a first therapeutic level consisting of five PRRT cycles, one every two months, followed by a potential second therapeutic level of at most three PRRT cycles. The choice of the therapeutic approach depends on the clinical assessment and on the tumor lesion dimensions. Two therapeutic schemes can be used on the first level. The first scheme, named MONO PRRT, consists in five administrations of ^{177}Lu-DOTATOC with an activity per cycle ranging from 3.7 to 5.55 GBq. The second scheme, named DUO PRRT, consists in three administrations of ^{177}Lu-DOTATOC at the 1st, 3rd and 5th cycle with an activity per cycle ranging from 3.7 to 5.55 GBq, interspersed with two administrations of ^{90}Y-DOTATOC with an activity per cycle ranging from 1.85 to 2.77 GBq.

In order to guarantee a positive balance in terms of benefit (response) and risk (toxicity), a dosimetric assessment for each patient will be performed at 1st and 5th cycle. Figure 7.1 resumes the therapeutic scheme used for PRRT at first therapeutic level.

The optional second therapeutic level can consist in three administrations of ^{177}Lu-DOTATOC with an activity per cycle ranging from 3.7 to 5.55 GBq.

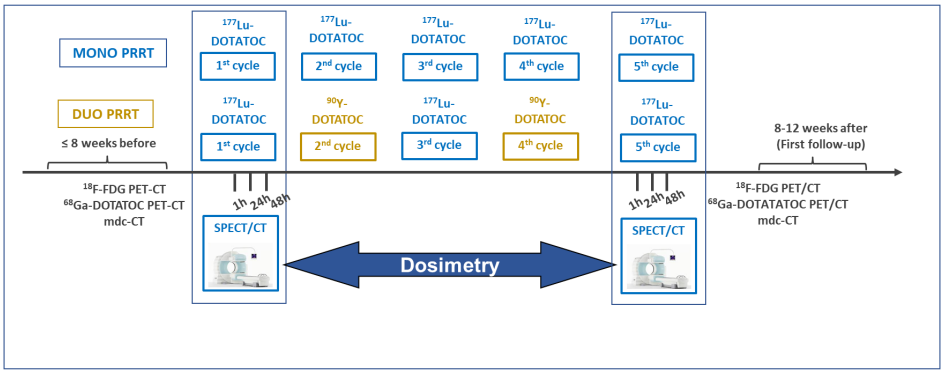

Figure 7.1: Therapeutic scheme used for PRRT in FENET protocol.

Eighty (80) (50 male and 30 female; $60 \pm 13[25-84]$ years of age) patients with metastasized NETs were enrolled in the study from July 2018 to February 2020. All patients received five cycles (MONO or DUO PRRT) with a mean injected activity of $4.9\,GBq$ (range: $3.5-6.5$) and $2.9\,GBq$ (range: $2.2-4.7$) for ^{177}Lu and ^{90}Y respectively. The administered activities at the 1^{st} cycle were chosen based on the patient's status and on the experience reported by the clinicians, while the subsequent administration were also guided by the results of dosimetry.

The administration of the radiopharmaceutical was executed via peripheral intravenous injection. In order to obtain adequate hydration and to protect kidneys during the radiopharmaceutical excretion, all patients were administered with arginine. Both during the administration of the radiopharmaceutical and for the following 48 hours, the patients were hospitalized in isolation rooms. All the procedures and the staff training were performed according to the radioprotection regulations.

7.2 Tumors and Organs At Risk Dosimetry

The gamma camera was properly calibrated to determine the fundamental parameters for dosimetry, such as the Calibration Factor (CF) and the Recovery Coefficient (RC). Procedure and results are presented in Chapter 6

The individual patient dose estimations in this study were determined according to the MIRD scheme [[84], [49], [85]]. To determine the time-activity curves in tumors and OARs, serial SPECT/CT images (Siemens Symbia Intevo T Series gamma camera, MELP collimator,

peak at 113 keV and 208 keV; 15% energy window; 64 projections, 30s/view, 128x128 matrix). Three SPECT/CT acquisitions have been performed on both 1st and the 5th cycle on every patient undergoing PRRT, respectively at 1, 24 and 48 h after the radiopharmaceutical administration. The acquired images were then corrected for the Collimator Detector Response (CDR), for the scatter contribution applying the TEW and the DEW methods [[86]] presented in Chapter4. SPECT/CT data were reconstructed at the Symbia.net workflow station, using the Siemens Flash 3D OSEM iterative reconstruction software, which applies scatter and attenuation correction.

Dosimetry was performed for every patient on the OARs (kidneys and BM) and on one, two or three representative tumor lesions selected by the nuclear medicine physician. Every reconstructed SPECT image was registered with the corresponding CT scan and processed via the MIM® workstation. An automated workflow allows to contour the volume of interest (VOI) of tumors, kidneys and bone segments on sequential and co-registered images using a non-rigid registration algorithm (Figure 7.2). Specifically, kidneys and L2-L4 lumbar vertebrae for bone marrow were contoured on the CT reconstructed images. Tumors were contoured with a percentage threshold of the maximum activity, the threshold being evaluated case-by-case depending on the concentration of the activity.

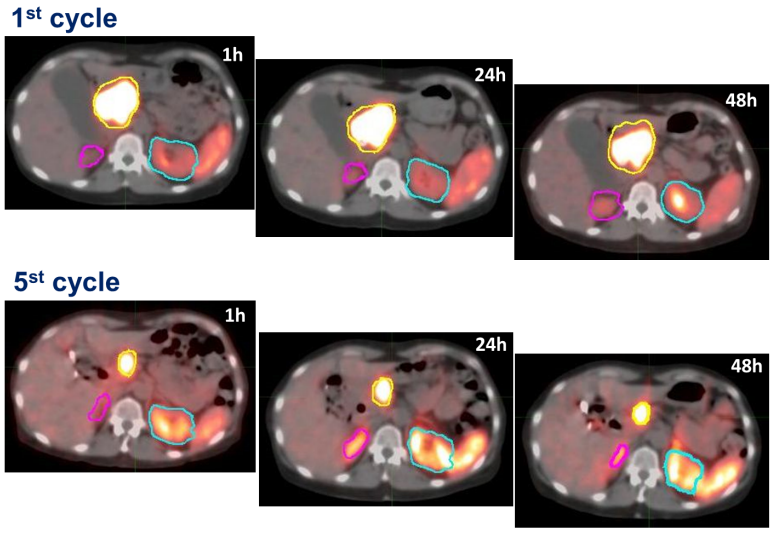

Figure 7.2: Therapeutic scheme used for PRRT in FENET protocol.

The software allows to obtain a complete report of the data correlating volume, total counts and counts per ml in function of acquisition time, for each selected VOI. The contouring of tumors and OARs allowed the evaluation of the deposited activity at the three different times

(1, 24 and 48 h) post-injection [[85]]. Recovery coefficients were applied to the VOIs in order to correct for the partial volume effect.

Through the activity-time curve, the residence times and the absorbed organ and tumor doses were obtained exploiting the software OLINDA/EXM v2.2[[87]], using the standard organ masses included in the software and the personalized organ masses obtained from the CT scans [[87]]. Particularly, mean absorbed tumor doses were estimated by using the unit density sphere module of OLINDA/EXM.

For BM dosimetry, the patient's BM was delineated on the trabecular section of the L2-L4 lumbar vertebrae, and the corresponding mass was calculated by scaling the reference man value with the volumes:

$$m_{L2-L4}^{patient} = m_{L2-L4}^{ref.man} \times \frac{V_{L2-L4}^{patient}}{V_{L2-L4}^{ref.man}} \tag{7.1}$$

The time integrated activity was calculated from the fit of the data obtained from the contouring at 1, 24 and 48 h, in order to obtain the absorbed dose to the BM, assuming the bone marrow mass in L2-L4 as representative of 6.7% of the total bone marrow mass and using the S-value for the bone marrow tabulated in MIRD Pamphlet no. 11 [[81], [82], [88]]:

$$D_{RM} = \frac{\tilde{A}_{L2-L4}}{0.067} \times S(RM \leftarrow RM) \times \frac{V_{L2-L4}^{ref.man}}{V_{L2-L4}^{patient}} \tag{7.2}$$

Since SPECT/CT studies were acquired only at the 1st and 5th cycle, at the 2nd, 3rd and 4th cycles in MONO PRRT (those involving the sole ^{177}Lu-DOTATOC) dosimetric evaluation was performed by scaling the Absorbed Dose/Administered Activity for the actual administered activity. For the intermediate cycles of DUO PRRT (those involving ^{90}Y-DOTATOC administration at the 2nd and 4th cycle), the SPECT image counts were also rescaled to correct for the difference in half-life between the two isotopes. Specifically, since the pharmaceutical vector (DOTATOC) is the same, we assumed that the biodistribution of ^{90}Y was the same as ^{177}Lu. This means that we based our evaluation for ^{90}Y for the 2nd administration cycle dosimetry on the ^{177}Lu imaging data of the 1st administration cycle. Activity values assessed by the image quantification with ^{177}Lu at 1h, 24h and 48h were scaled by the different administered activity and by the different half-life of the isotope, thus maintaining the biological uptake and washout unvaried. Then, we exploited OLINDA for the

absorbed dose calculation.

Moreover, the Biological Effective Doses (BED) were evaluated for the OARs according to the formula:

$$BED = \sum_i D_i + \frac{\beta}{\alpha} \frac{T_{1/2}^{rep}}{T_{1/2}^{rep} + T_{1/2}^{eff}} \sum_i D_i^2 \tag{7.3}$$

where D is the absorbed dose, μ is the exponential repair rate constant, and λ is the effective clearance rate. α and β are the tissue specific coefficients for radiation damage with α proportional to dose and β proportional to dose squared [[89]].

The absorbed dose errors were evaluated starting with the poisson statistical error associated to the counts in the selected VOI. This was propagated with the error associated to the dose calibrator and with the error associated to the evaluation of the CF. Since the contouring operation was performed by the same operator, no error was associated to the definition of the VOI.

The comparison of dosimetric results between MONO and DUO PRRT and between 1st and 5th cycles were performed. The variations of these comparisons were statistically evaluated by using bilateral t-test for two dependent means with a significance level of 0.95.

7.2.1 Three Time Points Dosimetry

The three-points dosimetry evaluation was implemented for practical and organizational reasons, such as guaranteeing two administration sessions per week for a large number of patients and managing with the presence of several patients coming from afar.

Since the first 5 patients underwent 5 SPECT/CT studies each (1, 24, 48, 72 and 96 h), in order to guarantee a correct dosimetric evaluation despite the reduced number of imaging acquisitions we compared the evaluation of absorbed dose to kidneys, bone marrow and tomors with 5 and 3 time points. Figure 7.3 shows a comparison between the mono- or bi-exponential fits using 5 or 3 time points.

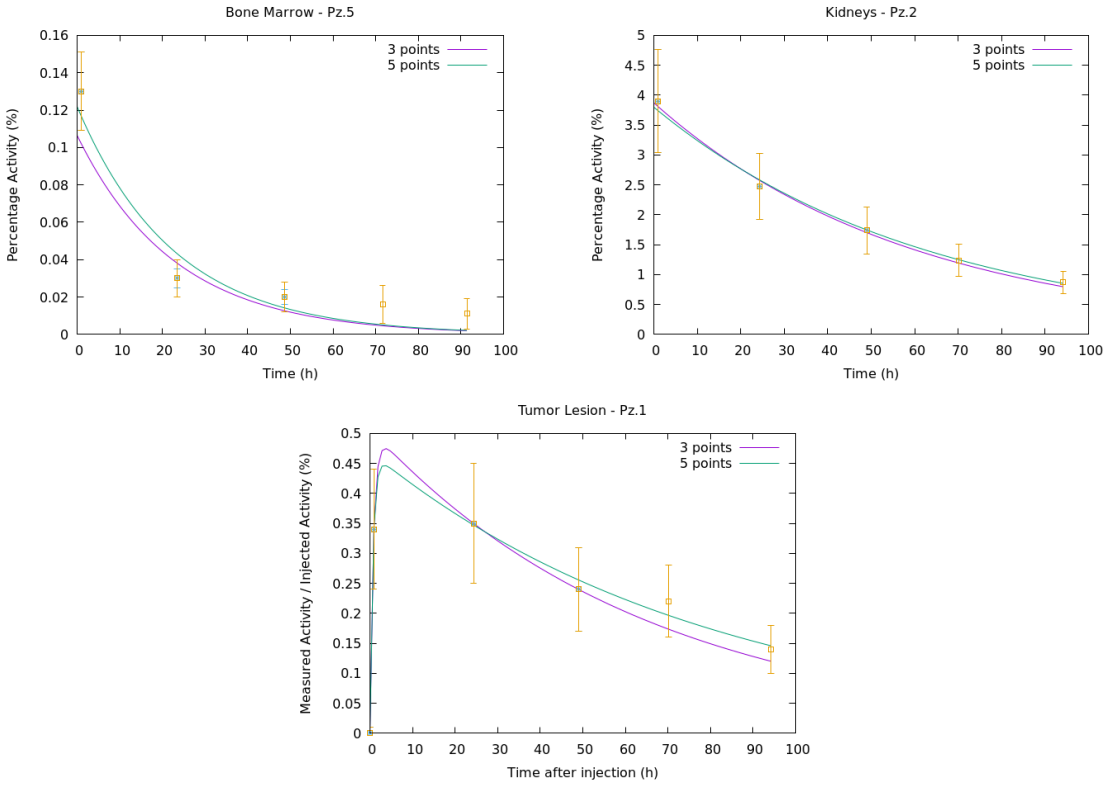

Figure 7.3: Examples of 5 and 3 time points fit comparison for kidneys (top left), bone marrow (top right) and tumor lesion (bottom).

Results showed a difference in the evaluation of absorbed dose between −8% and +4% for kidneys, −16% and +9% for bone marrow, −12% and +7% for tumors, in comparison to percent errors associated to absorbed dose evaluation we obtained ranging between 20% and 25%. Since the difference between the evaluation with 5 and 3 time points proved being smaller than the uncertainty, we considered the 3 time points dosimetry to be reasonably acceptable given the logistical necessities required by the therapy.

7.3 Results

Among the 80 patients that underwent PRRT with ^{177}Lu- and ^{90}Y-DOTATOC, 69 patients completed the treatment and were included in the dosimetric evaluation. The number of patients underwent to MONO and DUO PRRT were 30 and 39 respectively. Detailed information about the number of dosimetric calculation performed with MONO and DUO PRRT for each cycle are given in Table 7.1.

The results of the dosimetric studies, i.e. the mean half-lives and the mean absorbed doses

Table 7.1: Number of dosimetric studies performed for MONO and DUO PRRT.

	n. of dosimetric studies MONO PRRT		n. of dosimetric studies DUO PRRT		
	1^{st} cycle	$5^{th}cycle$	1^{st} cycle	$2^{nd}cycle$	$5^{th}cycle$
Kidneys	38	38	29	29	29
Bone Marrow	32	33	22	22	22
Tumor lesions	36	34	29	29	27

(AD) per administered activities of all 80 patients are presented in Table 7.2 for 1st and 5th cycles respectively.

Table 7.2: Comparison of dosimetric results (mean ± SD) between 1st and 5th cycles.

	Mean effective half-life (h)		Mean AD per administered activity (Gy/GBq)	
	1^{st} cycle	$5^{th}cycle$	1^{st} cycle	$5^{th}cycle$
Kidneys	43.1 ± 15.4	44.8 ± 15.5	0.6 ± 0.2	0.6 ± 0.3
Bone Marrow	17.6 ± 6.2	17.7 ± 6.5	0.02 ± 0.01	0.02 ± 0.01
Tumor lesions	81.1 ± 25.7	81.7 ± 28.7	2.5 ± 1.6	1.5 ± 1.1

7.3.1 Organs At Risk Dosimetry

In most of the patients, the kinetics for kidneys and BM showed a similar behavior. An example of time-activity curves is shown in Figure 7.4.

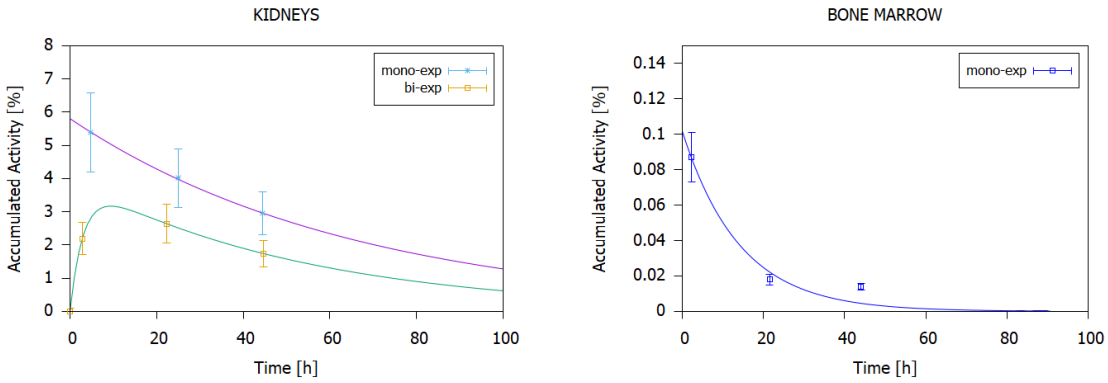

Figure 7.4: Examples of time-activity curves for kidneys and BM.

For the kidneys, in most of the patients a first fast washout followed by a slower decrease was found. For this reason, renal uptake curves were fitted to mono-exponential functions, resulting in a longer mean half-life of 43.9 ± 15.4 hours. In few cases a maximum uptake between the 1 and 24 h followed by a fast washout was observed; in these cases, a bi-exponential fit functions were used. The BM uptake curves showed the same trend for all patients: a fast washout was observed and a monoexponential fit functions was used, resulting in mean half-live of

17.7 ± 6.3 hours.

The mean ADs per administered activities obtained for kidneys and BM are reported for the 1st and 5th cycles for MONO PRRT and for the 1st, 2nd and 5th cycles for DUO PRRT (Figure 7.5).

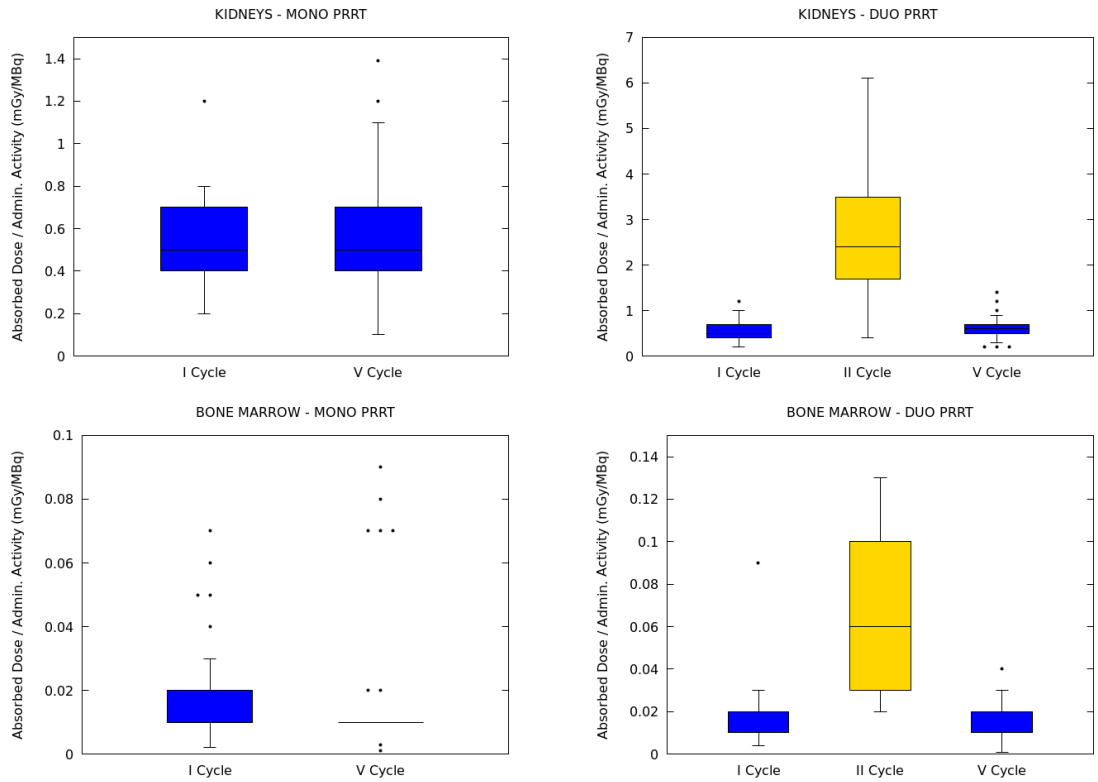

Figure 7.5: Mean absorbed doses per administered activities obtained for kidneys and BM for MONO and DUO PRRT.

The median AD to kidneys per cycle was 2.7 Gy (range 0.8 - 6.3 Gy) for the 1st cycle (^{177}Lu), 7.6 Gy (range 1.2 - 18.9 Gy) for the 2nd cycle (^{90}Y, only for the DUO PRRT protocol) and 2.7 Gy (range 0.7 - 7.2 Gy) for the 5th cycle (^{177}Lu) calculated from a total of 67, 29 and 67 cycles respectively. These data correspond to a median AD per administered activity of 0.5 Gy/GBq (range 0.2 - 1.2 Gy/GBq) for the 1st cycle (^{177}Lu), 2.5 Gy/GBq (range 0.4 - 6.1 Gy/GBq) for the 2nd cycle (^{90}Y, only for the DUO PRRT protocol) and 0.5 Gy/GBq (range 0.1 - 1.4 Gy/GBq) for the 5th cycle (^{177}Lu) respectively.

The median AD to BM per cycle was 0.50 Gy (range 0.02 – 0.20 Gy) for the 1st cycle (^{177}Lu), 0.13 Gy (range 0.06 – 0.42 Gy) for the 2nd cycle (^{90}Y, only for the DUO PRRT protocol) and 0.53 Gy (range 0.01 – 0.34 Gy) for the 5th cycle (^{177}Lu) calculated from a total of 55, 22 and

55 cycles respectively. These data correspond to a median AD per administered activity of 0.010 Gy/GBq (range 0.003 – 0.070 Gy/GBq) for the 1st cycle (^{177}Lu), 0.05 Gy/GBq (range 0.02 – 0.13 Gy/GBq) for the 2nd cycle (^{90}Y, only for the DUO PRRT protocol) and 0.010 Gy/GBq (range 0.001 – 0.090 Gy/GBq) for the 5th cycle (^{177}Lu) respectively.

The mean AD per single administration calculated for ^{90}Y are approximately five times higher than those for ^{177}Lu, specifically with a mean factor of 4.9 for kidneys (median 5.3, range 2.2 - 6.2) and with a mean factor of 4.4 for bone marrow (median 4.5, range 2.0 - 8.0).

In order to further compare the effect of ^{177}Lu and ^{90}Y, BED results per cycle were also compared. Specifically, BED was calculated for the 1st, 2nd and 5th administration cycles. In Figure 7.6, boxplots showing the BED calculated for kidneys and bone marrow divided by radioisotope (^{177}Lu for 1st and 5th cycle, ^{90}Y for 2nd cycle) are displayed.

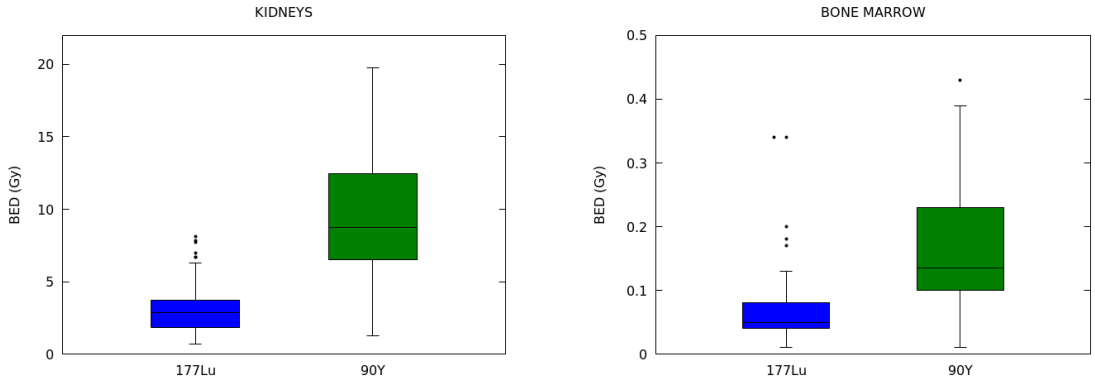

Figure 7.6: BED ^{177}Lu and ^{90}Y.

The BED per single administration calculated for ^{90}Y are approximately five times higher than those for ^{177}Lu, specifically with a mean factor of 4.6 for kidneys (median 4.3, range 2.5 - 6.2) and with a mean factor of 4.1 for bone marrow (median 3.9, range 1.8 - 7.1).

The results show no trend towards higher or lower values with increased treatment cycle number for the overall group of both MONO and DUO PRRT, but rather a clear difference among patients. There are no appreciable differences in the ADs per administered activities to kidneys and BM between the 1st and 5th cycles for both MONO and DUO PRRT. The variations in mean effective half-life and AD between 1st and 5th cycles are not statistically significant (p-value = 0.44 for kidneys, p-value = 0.76 for BM) for both kidneys and BM.

In 10 cases, all of them regarding patients undergoing the DUO PRRT protocol, the total absorbed doses to kidneys exceeded the threshold reported in literature of 28 Gy (23 Gy for patients with risk factors). None of these resulted in increased renal toxicity according to clinical evaluations run by the nuclear medicine physician. No cases exceeding the total AD of 2 Gy to bone marrow were reported. The results of ADs for kidneys and BM obtained with MONO PRRT and DUO PRRT are reported in Figure 7.7.

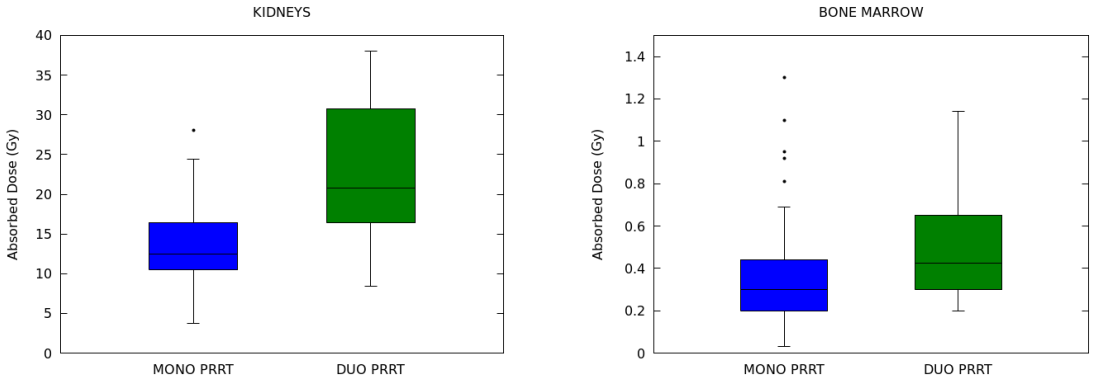

Figure 7.7: Mean absorbed doses obtained for kidneys and BM for MONO and DUO PRRT.

The mean increase in the AD to kidneys and BM is respectively 76% and 28% when using DUO with respect to MONO PRRT. The variations in AD between MONO and DUO PRRT are statistically significant for kidneys (p-value < 0.001) but not for BM (p-value $= 0.13$).

As shown in Figure 7.8, the median BED referred to all treatment cycles was 13.2 Gy (range 1.3 - 31.9 Gy) and 0.30 Gy (range 0.10 - 0.97 Gy) for kidneys and BM respectively. The wide range was due to both inter- and intra-patient variability. Figure 7.9 shows the correlation between BED and AD for kidneys and BM.

The AD and BED values of BM were approximately equal, while for kidneys the median extra contribution to the BED from the AD increases with increasing absorbed dose and was 1.30 Gy (range 0.1 - 12.2 Gy).

Considering a maximum tolerated absorbed dose of 23 Gy to the kidneys or 2 Gy to the BM, the dose-limiting organ was the kidney in 15% of the patients. With a maximum tolerated BED of 38 Gy to the kidney or an absorbed dose of 2 Gy to the BM, the kidney was the

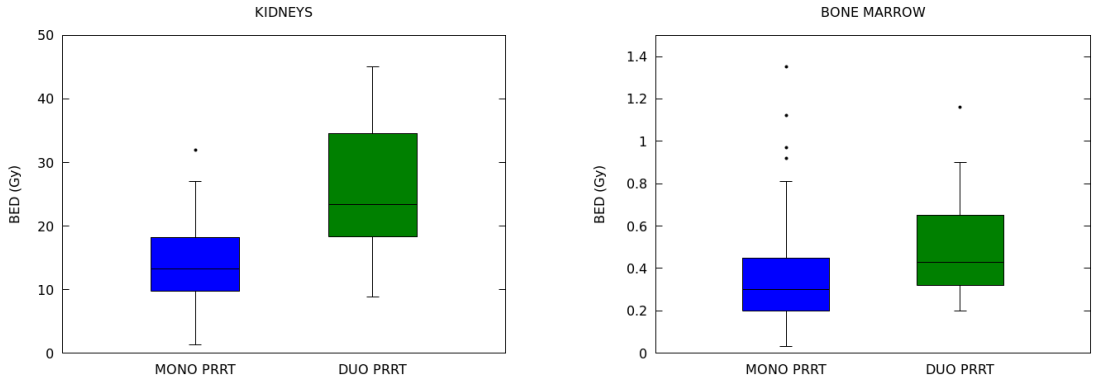

Figure 7.8: BED obtained for kidneys and BM for MONO and DUO PRRT.

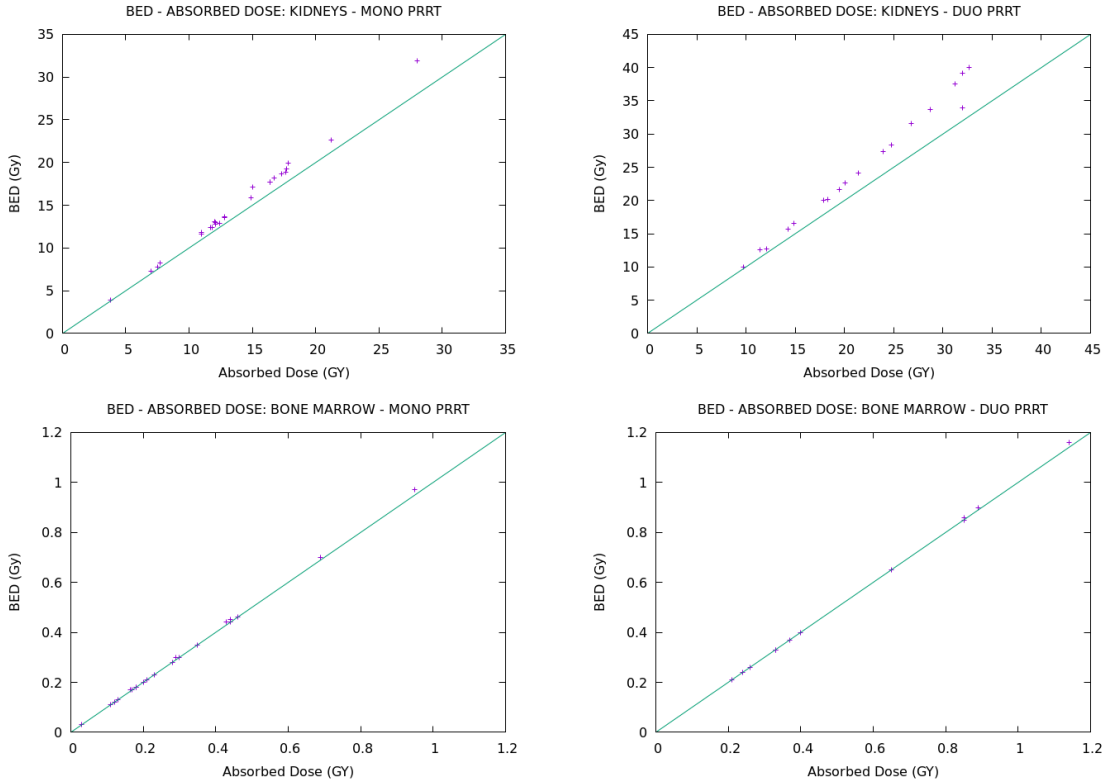

Figure 7.9: Correlation between BED and AD for kidneys and BM.

dose-limiting organ in 9% of the patients.

7.3.2 Tumor Dosimetry

Tumor dosimetry was performed in a total number of 48 tumor lesions. The kinetics results of tumor lesions for 1st and 5th cycles are given in Table 7.2. The washout from tumor lesions was different to that of the OARs, as is summarized in Table 7.2.

Differences were found for the uptake in metastases, as it depends on the localization, types of metastases and tumor volumes. An example of time-activity curves is shown in Figure 7.10.

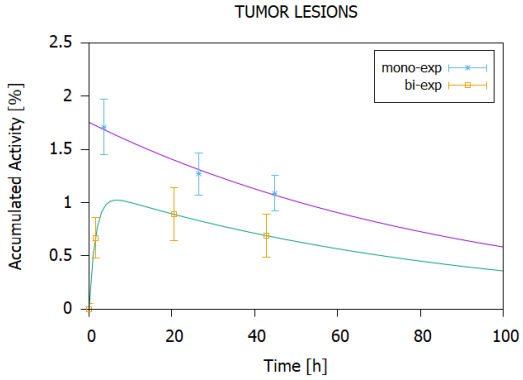

Figure 7.10: Examples of time-activity curves for tumor lesions.

Most frequently, the uptake curve showed a rapid increase between 1 and 24 hour followed by a slower washout. The time-activity curves of tumor lesions were fitted to biexponential functions.

The variations in mean effective half-life and AD per administered activities between 1st and 5th cycles are not statistically significant (p-value = 0.77) for tumor lesions.

The mean absorbed cumulative tumor dose for all tumor lesions was $79.0 \pm 57.4\,Gy$ with a mean absorbed dose of $48.0 \pm 29.2\,Gy$ for MONO PRRT and $117.6 \pm 60.8\,Gy/GBq$ for DUO PRRT respectively. Figures 7.11 and 7.12 report the differences in ADs and ADs per administered activities between MONO and DUO PRRT.

The mean AD to tumors per cycle was $11.9 \pm 7.6\,Gy$ for the 1st cycle (^{177}Lu), $39.9 \pm 21.8\,Gy$ for the 2nd cycle (^{90}Y, only for the DUO PRRT protocol) and $7.6 \pm 5.6\,Gy$ for the 5th cycle (^{177}Lu) calculated from a total of 65, 29 and 61 cycles respectively. These data correspond to a mean AD per administered activity of $2.5 \pm 1.6\,Gy/GBq$ for the 1st cycle (^{177}Lu), $14.1 \pm 7.5\,Gy/GBq$ for the 2nd cycle (^{90}Y, only for the DUO PRRT protocol) and 1.5 ± 1.1 $,Gy/GBq$ for the 5th cycle (^{177}Lu) respectively. The variations in AD between MONO and DUO PRRT are statistically significant (p-value < 0.001) for tumors.

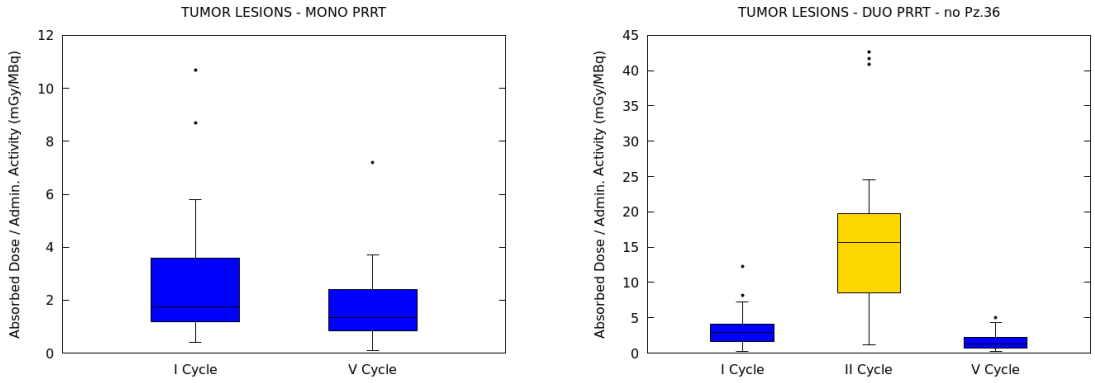

Figure 7.11: Mean absorbed doses per administered activities obtained for tumor lesions for MONO and DUO PRRT.

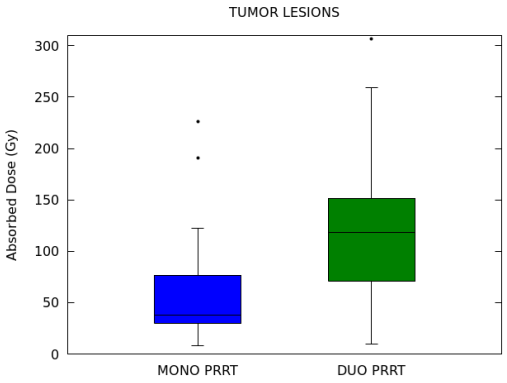

Figure 7.12: Mean absorbed doses obtained for tumor lesions for MONO and DUO PRRT.

A comparison between the results obtained for ^{177}Lu in this study and others known from literature is presented in Table 7.3.

Table 7.3: Comparison of dosimetric results (mean ± SD and/or [min - max]) between the results in absorbed dose per administered activity for ^{177}Lu between this study and data from literature.

	Kidneys (Gy/GBq)	Bone Marrow (Gy/GBq)	Tumors (Gy/GBq)
Forrer 2009 [[80]]	-	0.034 ± 0.030	-
Kairemo 2013 [[90]]	1.15 [$0.54 - 2.16$]	< 0.07	0.02 ± 0.01
Del Prete 2017 [[72]]	0.55 ± 0.20	0.046 ± 0.033	4.2 ± 2.9
Marin 2018 [[91]]	0.78 ± 0.35	0.028 ± 0.010	-
Santoro 2018 [[92]]	0.43 ± 0.13	0.04 ± 0.02	-
Del Prete 2019 [[73]]	0.54 [$0.24 - 4.25$]	0.035 [$0.004 - 0.216$]	4.4 [$0.1 - 32.0$]
This study	0.6 ± 0.2 [$0.1 - 1.4$]	0.02 ± 0.01 [$0.001 - 0.090$]	2.2 ± 1.6 [$0.1 - 9.4$]

7.4 Discussion and Conclusions

In the present study, we have retrospectively analyzed data on dosimetry after ^{177}Lu-DOTATOC and ^{90}Y-DOTATOC PRRT individualized treatment protocols, with the aim of

maximizing the absorbed dose to tumor tissue without overcoming the maximum tolerable dose to risk organs.

Nowadays, ^{177}Lu-DOTATATE/DOTATOC and ^{90}Y-DOTATOC are certainly the most clinically used radiopeptides in treatments of NENs. ^{90}Y is particularly suitable for radionuclide therapy, but not for imaging. Reported experiences with ^{90}Y-DOTATOC yielded favorable results particularly in larger tumors [[69]], while the major concern is related to the high renal dose delivered [[70]]. The physical properties of ^{177}Lu offer some advantages with respect to ^{90}Y: it is suitable for both imaging and therapy [[75]] and it may reasonably exert a more favorable effect on small tumors (<2 cm) and micrometastases. All studies agree in reporting absorbed dose to OARs lower for ^{177}Lu as compared with ^{90}Y.

Dosimetry in PRRT usually would require multiple post-therapy SPECT/CT scans, but often data collection has to be stopped on the second or third day after therapy for logistic reasons. The protocol used in this study is based on dosimetry performed using three time-points (i.e. SPECT/CT scans at 1, 24 and 48h after treatment). Our experience demonstrated that this simplified approach represents a feasible tool for faster therapy management and a viable method to improve the patient's comfort. However, the limited number of SPECT/CT acquisition over the time used in the proposed protocol could affect the accuracy of the time-activity curve determination, especially for sites having a longer washout for which the late time point (i.e. 72 or 96 h) acquisition could be relevant. Another limitation of this study lies in the fragmentation of the workflow followed for the dosimetric purposes, which could increase the possibility of inducing errors and is time consuming with a great effort of resources. Moreover, further investigation could be directed to the intercomparison of the used methodology with systems used in other centres of with approved software.
Despite the discussed limitations and the large variation reported in the literature on average absorbed doses for OARs and tumors due to differences in methodology as well as patients' characteristics, the average absorbed doses calculated by our simplified but personalized methodology is well within the range of published data by other groups, as reported in Table 7.3. According to our experience, the large interindividual variations and the need to effectively treat patients with different disease status, histological tumor types and treatment history suggest to recommend an individualized dosimetric approach.

Chapter 8

Dose Calculation with Direct Monte Carlo Radiation Transport

Monte Carlo simulation is an essential tool in emission tomography to assist in the design of new medical imaging devices, assess new implementations of image reconstruction algorithms and/or scatter correction techniques, and optimize scan protocols. Specifically, in this chapter the direct Monte Carlo radiation transport approach was used to perform image-based dose calculations at voxel level.

Dedicated Monte Carlo codes have been developed for Positron Emission Tomography (PET) and for Single Photon Emission Computerized Tomography (SPECT). Accurate and versatile simulation codes such as EGS4 [[53]], MCNP [[54]], and GEANT4 [[93]] have been written for high energy physics. They all include well-validated physics models, geometry modeling tools, and efficient visualization utilities. However, these packages are quite complex and necessitate a steep learning curve.

GATE [[94]], the GEANT4 Application for Tomographic Emission, encapsulates the GEANT4 libraries in order to achieve a modular, versatile, scripted simulation toolkit adapted to the field of nuclear medicine. In particular, GATE provides the capability for modeling time-dependent phenomena such as detector movements or source decay kinetics, thus allowing the simulation of time curves under realistic acquisition conditions.

8.1 GATE

GATE was developed within the OpenGATE Collaboration with the objective to provide the academic community with a free software, general-purpose, GEANT4-based simulation platform for emission tomography.

GATE combines the GEANT4 simulation toolkit of validated physics models with geometry description, visualization and 3D rendering tools with features specific to emission tomography. It consists of several hundred C++ classes. Mechanisms used to manage time, geometry, and radioactive sources form a core layer of C++ classes close to the GEANT4 kernel (see Figure 8.1). An application layer allows for the implementation of user classes derived from the core layer classes, such as building specific geometrical volume shapes and specifying operations on these volumes. Since the application layer implements all appropriate features, the use of GATE does not require C++ programming: a dedicated scripting mechanism that extends the native command interpreter of GEANT4 makes it possible to perform and to control Monte Carlo simulations of realistic setups.

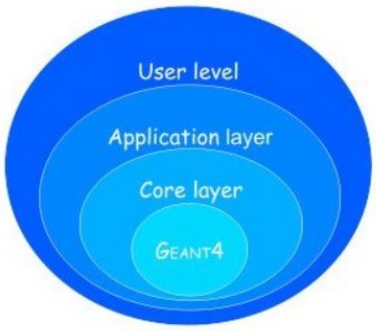

Figure 8.1: Structure of GATE.

An innovative feature of GATE is its capability to synchronize all time-dependent components in order to allow a coherent description of the acquisition process. The acquisition is subdivided into a number of time-steps during which the elements of the geometry are considered to be at rest. Decay times are generated within these time-steps so that the number of events decreases exponentially from time-step to time-step and decreases also inside each time-step according to the decay kinetics of each radioisotope. This allows for the modeling of time-dependent processes such as count rates, random coincidences, or detector dead-time on an event-by-event basis.

8.2 Implementation

Simulations were performed with GATE version 8.2, which is based on Monte Carlo code GEANT4 version 10.05 patch.01. GEANT standard physics list emlivermore was used for this study, which is designed for any applications required higher accuracy of electrons, hadrons and ion tracking without magnetic field. Range cuts were set to 0.1 mm for gamma particles, electrons and positrons inside the phantom and to 10 mm outside the phantom.

The DoseActor was used to score at the voxel level, and associated uncertainties were calculated in each scoring voxel with the DoseActor UncertaintyEDep. The scoring matrix volume was defined with the dimensions of the input phantom matrix. GATE was run with a Mersenne Twister random number generator.

Out of the 80 patients of the FENET 2016 protocol studied with the OLINDA/EXM software, 10 patients with hepatic tumors were selected for a comparison with image-based calculation. Specifically, the aim was the calculation of absorbed dose to kidneys and tumors for the first administration cycle, thus only for the ^{177}Lu-DOTATOC administration.

8.3 GATE Code Validation

The GATE code was validated by deriving different dosimetry parameters, according to the Medical Internal Radiation Dose (MIRD) committee definitions [[48]]:

- the specific absorbed fraction (SAF) $\Phi(k \leftarrow h)$ (kg^{-1}), that is the ratio between the absorbed fraction $\phi(k \leftarrow h)$ (defined in Chapter 5 as the ratio between the energy E_0 emitted in source region h and the absorbed energy E in target region k) and the mass of the target organ m_k:

$$\Phi(k \leftarrow h) = \frac{\phi(k \leftarrow h)}{m_k} \tag{8.1}$$

- the S-value ($Gy(Bq \cdot s)^{-1}$), that is the mean absorbed dose to the target k per unit of cumulated activity in the source region h:

$$S(k \leftarrow h) = \sum_i \Delta_i \Phi(k \leftarrow h) \tag{8.2}$$

where $\Delta_i = n_i E_i$ with E_i is the energy emitted for radiation type i with probability n_i.

SAFs were evaluated for monoenergetic photons and electrons of 50 keV, 100 keV, 500 keV and 1 MeV. S-values were also calculated for ^{177}Lu, and for these simulation runs the radioisotope's beta, gamma, X-ray and Auger electron emissions were taken into account. All nuclear data used in the simulation runs were taken from ICRP 107 [[96]].

The male and female adult reference voxel models from ICRP Publication 110 [[95]] were used for the validation simulations. Their voxel matrixes were used both as scoring volumes and as attenuation map and activity matrix sources for the validation runs. Each voxel was labelled in order to associate it to a specific tissue, which in turn was associated to a material with its atomic composition. In Figure 8.2 the male and female adult reference voxel models are shown, and their characteristics are presented in TableFigure 8.1 .

Table 8.1: The ICRP110 male and female phantoms characteristics [[95]].

Property	Male	Female
Height (m)	1.76	1.63
Mass (kg)	73.0	60.0
Number of columns	254	299
Number of rows	127	137
Number of slices	222	348
Slice thickness (mm)	8.0	4.84
Voxel in-plane resolution (mm)	2.137	1.775

All the 141 tissues or organs described in ICRP publication 110 were taken into account during the computations. SAFs for monoenergetic photons and electrons were evaluated for 3 different source organs (liver, lungs and thyroid) and for 1 target organ (lungs), thus considering one case of self-irradiation and two cases of cross-irradiation. S-values for ^{177}Lu were calculated for 1 organ (kidneys) considered as both source and target, thus only for the self-irradiation component. The characteristics of the organs considered in these simulation runs are listed in Table 8.2

SAFs for monoenergetic photons and electrons were then compared with those obtained by

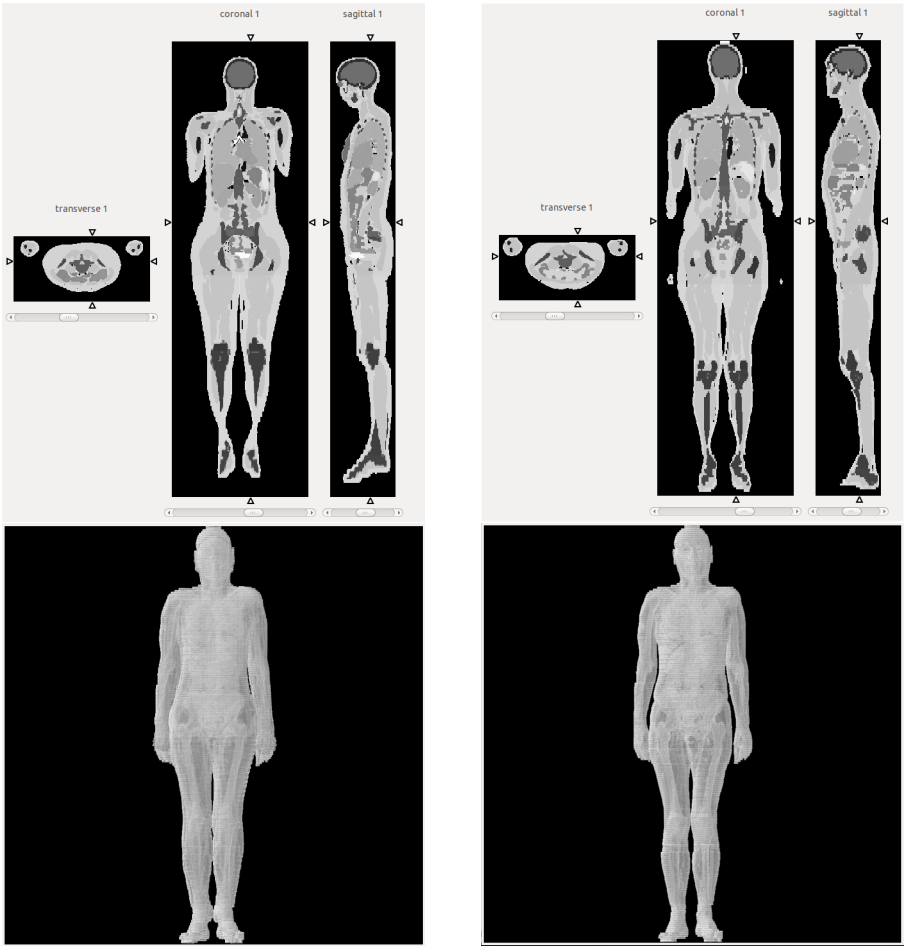

Figure 8.2: The male and female adult reference voxel models. Top row: female (left) and male (right) phantoms transverse, coronal and saggital views. Bottom row: 3D rendering of the female (left) and male (right) phantoms.

Table 8.2: List of ICRP110 organs (male and female) selected for the comparison [[95]].

Organ	IDs	Mass (g)	
		Male	Female
Kidneys	89, 90, 91, 92, 93, 94	310.04	275.00
Liver	95	1800.00	1400.00
Lungs	96, 97, 98, 99	1208.43	950.00
Thyroid	132	19.99	17.00

Hadid *et al* [[97]] using MCNPX and EGSnrc for both adult male and female computational phantoms, and with those obtained by Villoing *et al* [[98]] using MCNPX and GATE for the only female phantom. Results are presented in Tables 8.3 and 8.4 for the female phantom and in Tables 8.5 and 8.6 for the male phantom.

^{177}Lu S-values were compared with those tabulated in OpenDose: Open-Access Resource for Nuclear Medicine Dosimetry [[99]]. Results are presented in Table 8.7.

100 million of primaries were systematically simulated for each source-target couple to ensure acceptable uncertainties (relative uncertainty $< 0.5\%$ in case of self-absorption).

Table 8.3: SAFs for electrons: female phantom. Comparison of results from this work with data published in Hadid *et al* [[97]] and with Villoing *et al* [[98]].

Lungs ← Liver SAFs (kg^{-1})					
	Hadid *et al*		Villoing *et al*		This work
E(MeV)	MCNPX	EGSnrc	MCNPX	GATE	GATE
0.05	8.18×10^{-05}	7.75×10^{-05}	8.01×10^{-05}	8.04×10^{-05}	7.99×10^{-05}
0.10	2.69×10^{-04}	2.62×10^{-04}	2.61×10^{-04}	2.57×10^{-04}	2.60×10^{-04}
0.50	2.67×10^{-03}	2.65×10^{-03}	2.66×10^{-03}	2.59×10^{-03}	2.60×10^{-03}
1.00	5.55×10^{-03}	5.52×10^{-03}	5.54×10^{-03}	5.54×10^{-03}	5.56×10^{-03}
Lungs ← Lungs SAFs (kg^{-1})					
	Hadid *et al*		Villoing *et al*		This work
E(MeV)	MCNPX	EGSnrc	MCNPX	GATE	GATE
0.05	$1.05 \times 10^{+00}$	$1.05 \times 10^{+00}$	$1.05 \times 10^{+00}$	$1.05 \times 10^{+00}$	$1.04 \times 10^{+00}$
0.10	$1.05 \times 10^{+00}$	$1.05 \times 10^{+00}$	$1.05 \times 10^{+00}$	$1.05 \times 10^{+00}$	$1.04 \times 10^{+00}$
0.50	9.99×10^{-01}	9.95×10^{-01}	$1.02 \times 10^{+00}$	$1.02 \times 10^{+00}$	$1.00 \times 10^{+00}$
1.00	9.42×10^{-01}	9.35×10^{-01}	9.82×10^{-01}	9.82×10^{-01}	$9.80 \times 10^{+00}$
Lungs ← Thyroid SAFs (kg^{-1})					
	Hadid *et al*		Villoing *et al*		This work
E(MeV)	MCNPX	EGSnrc	MCNPX	GATE	GATE
0.05	2.18×10^{-06}	2.17×10^{-06}	2.45×10^{-06}	1.94×10^{-06}	2.07×10^{-06}
0.10	6.11×10^{-06}	6.41×10^{-06}	6.77×10^{-06}	6.26×10^{-06}	6.36×10^{-06}
0.50	3.23×10^{-05}	3.22×10^{-05}	3.23×10^{-05}	3.20×10^{-05}	3.30×10^{-05}
1.00	6.02×10^{-05}	6.04×10^{-05}	5.98×10^{-05}	5.93×10^{-05}	5.97×10^{-05}

Table 8.4: SAFs for photons: female phantom. Comparison of results from this work with data published in Hadid *et al* [[97]] and with Villoing *et al* [[98]].

Lungs ← Liver SAFs (kg^{-1})					
	Hadid *et al*		Villoing *et al*		This work
E(MeV)	MCNPX	EGSnrc	MCNPX	GATE	GATE
0.05	2.41×10^{-02}	2.50×10^{-02}	2.48×10^{-02}	2.44×10^{-02}	2.39×10^{-02}
0.10	1.64×10^{-02}	1.75×10^{-02}	1.74×10^{-02}	1.76×10^{-02}	1.70×10^{-02}
0.50	1.49×10^{-02}	1.50×10^{-02}	1.50×10^{-02}	1.50×10^{-02}	1.48×10^{-02}
1.00	1.38×10^{-02}	1.38×10^{-02}	1.38×10^{-02}	1.39×10^{-02}	1.36×10^{-02}
Lungs ← Lungs SAFs (kg^{-1})					
	Hadid *et al*		Villoing *et al*		This work
E(MeV)	MCNPX	EGSnrc	MCNPX	GATE	GATE
0.05	1.26×10^{-01}	1.26×10^{-01}	1.38×10^{-01}	1.34×10^{-01}	1.30×10^{-01}
0.10	7.13×10^{-02}	7.06×10^{-02}	7.80×10^{-02}	7.66×10^{-02}	7.56×10^{-02}
0.50	6.95×10^{-02}	6.84×10^{-02}	7.70×10^{-02}	7.68×10^{-02}	7.48×10^{-02}
1.00	6.19×10^{-02}	6.08×10^{-02}	6.89×10^{-02}	6.82×10^{-02}	6.67×10^{-02}
Lungs ← Thyroid SAFs (kg^{-1})					
	Hadid *et al*		Villoing *et al*		This work
E(MeV)	MCNPX	EGSnrc	MCNPX	GATE	GATE
0.05	2.51×10^{-02}	2.55×10^{-02}	2.51×10^{-02}	2.46×10^{-02}	2.50×10^{-02}
0.10	1.80×10^{-02}	1.81×10^{-02}	1.80×10^{-02}	1.77×10^{-02}	1.80×10^{-02}
0.50	1.60×10^{-02}	1.61×10^{-02}	1.61×10^{-02}	1.62×10^{-02}	1.59×10^{-02}
1.00	1.47×10^{-02}	1.48×10^{-02}	1.48×10^{-02}	1.50×10^{-02}	1.46×10^{-02}

Table 8.5: SAFs for electrons: male phantom. Comparison of results from this work with data published in Hadid *et al* [[97]].

Lungs ← Liver SAFs (kg^{-1})			
	Hadid *et al*		This work
E(MeV)	MCNPX	EGSnrc	GATE
0.05	3.98×10^{-05}	3.55×10^{-05}	3.70×10^{-05}
0.10	1.27×10^{-04}	1.29×10^{-04}	1.30×10^{-04}
0.50	1.35×10^{-03}	1.38×10^{-03}	1.36×10^{-03}
1.00	3.23×10^{-03}	3.25×10^{-03}	3.22×10^{-03}
Lungs ← Lungs SAFs (kg^{-1})			
	Hadid *et al*		This work
E(MeV)	MCNPX	EGSnrc	GATE
0.05	8.26×10^{-01}	8.31×10^{-01}	8.30×10^{-01}
0.10	8.23×10^{-01}	8.28×10^{-01}	8.24×10^{-01}
0.50	7.80×10^{-01}	7.80×10^{-01}	7.78×10^{-01}
1.00	7.29×10^{-01}	7.26×10^{-01}	7.30×10^{-01}
Lungs ← Thyroid SAFs (kg^{-1})			
	Hadid *et al*		This work
E(MeV)	MCNPX	EGSnrc	GATE
0.05	1.72×10^{-06}	1.42×10^{-06}	1.70×10^{-06}
0.10	5.47×10^{-06}	6.06×10^{-06}	5.65×10^{-06}
0.50	2.91×10^{-05}	2.92×10^{-05}	3.01×10^{-05}
1.00	5.40×10^{-05}	5.33×10^{-05}	5.37×10^{-05}

Table 8.6: SAFs for photons: male phantom. Comparison of results from this work with data published in Hadid *et al* [[97]].

Lungs ← Liver SAFs (kg^{-1})			
	Hadid *et al*		This work
E(MeV)	MCNPX	EGSnrc	GATE
0.05	2.20×10^{-02}	2.25×10^{-02}	2.21×10^{-02}
0.10	1.61×10^{-02}	1.62×10^{-02}	1.64×10^{-02}
0.50	1.35×10^{-02}	1.36×10^{-02}	1.35×10^{-02}
1.00	1.24×10^{-02}	1.25×10^{-02}	1.23×10^{-02}
Lungs ← Lungs SAFs (kg^{-1})			
	Hadid *et al*		This work
E(MeV)	MCNPX	EGSnrc	GATE
0.05	1.06×10^{-01}	1.05×10^{-01}	1.02×10^{-01}
0.10	6.08×10^{-02}	5.98×10^{-02}	6.01×10^{-01}
0.50	5.86×10^{-02}	5.72×10^{-02}	5.75×10^{-01}
1.00	5.22×10^{-02}	5.10×10^{-02}	5.10×10^{-01}
Lungs ← Thyroid SAFs (kg^{-1})			
	Hadid *et al*		This work
E(MeV)	MCNPX	EGSnrc	GATE
0.05	2.19×10^{-02}	2.20×10^{-02}	2.17×10^{-02}
0.10	1.63×10^{-02}	1.64×10^{-02}	1.60×10^{-02}
0.50	1.47×10^{-02}	1.47×10^{-02}	1.45×10^{-02}
1.00	1.35×10^{-02}	1.35×10^{-02}	1.35×10^{-02}

Table 8.7: ^{177}Lu S-values: female and male phantoms. Comparison of results from this work with data published in OpenDose [[99]].

Kidneys ← Kidneys S-values (kg^{-1})			
Female		Male	
OpenDose	This work	OpenDose	This work
8.72×10^{-05}	8.75×10^{-05}	7.72×10^{-05}	7.69×10^{-05}

Results obtained in this work show a perfect agreement with values published in both Hadid *et al* [[97]] and with Villoing *et al* [[98]], thus validating the GATE code.

8.4 Comparison with OLINDA/EXM Patients Dosimetry Results

The validated GATE code was exploited with ^{177}Lu to reproduce the kidneys absorbed dose calculated with OLINDA/EXM with those obtained with the Monte Carlo code. For this purpose, 10 patients were selected.

The OLINDA/EXM results were considered as a basis for comparison of the mean absorbed dose evaluation at the organ level [[100], [87]]. Since the calculation of absorbed dose to kidneys with OLINDA/EXM was performed by considering only the self-absorption induced by the activity accumulated inside the kidneys, as presented in Chapter 7, the same assumption was therefore made for this use of the code with GATE, thus considering only the self-irradiation of the kidneys. Dose calculations were performed for the first cycle of every patient taking into account the three SPECT/CT studies at 1h, 24h and 48h after the administration of ^{177}Lu.

Left and right kidney were considered as a single organ and the total dose was computed by collecting all the voxels of interest in a single region. Since OLINDA/EXM uses the MIRD formalism with S-values at organ level, in order to reproduce the same results the same assumptions were considered thus uniformly distributing the total activity evaluated for each time point among the voxels composing left and right kidney with a range option. The total number of events is produced in a one second duration simulation in order to obtain dose results per second. These data were both collected in a text file and saved in a raw data file with the same voxel matrix as that of the phantom voxel model. Thus, the resulting

Table 8.8: Kidneys data of the 10 patients. Volumes and activity at the three different time points after the ^{177}Lu-DOTATOC administration.

Patient	Volume (ml)	1h Activity (MBq)	24h Activity (MBq)	48h Activity (MBq)
1	387.4	230.6 ± 27.8	230.1 ± 27.8	171.0 ± 20.8
2	339.8	167.3 ± 20.2	83.7 ± 10.1	59.4 ± 7.2
3	428.0	168.3 ± 19.7	124.5 ± 15.0	96.9 ± 11.7
4	446.0	230.1 ± 27.8	169.0 ± 20.4	117.3 ± 14.2
5	401.3	270.2 ± 32.6	168.5 ± 20.4	114.8 ± 13.9
6	338.0	125.7 ± 15.2	133.3 ± 16.1	97.1 ± 11.7
7	308.0	118.3 ± 14.3	112.6 ± 13.6	82.5 ± 9.9
8	486.7	258.5 ± 31.2	136.7 ± 16.5	78.1 ± 9.4
9	293.0	113.3 ± 13.7	95.5 ± 11.5	76.3 ± 9.2
10	483.0	204.1 ± 24.7	152.2 ± 18.4	103.3 ± 12.5

Table 8.9: Absorbed dose results to kidneys obtained with GATE and the ICRP110 male and female phantoms for the 10 patients compared with those obtained with OLINDA/EXM and ratios between the two.

Patient	OLINDA/EXM Dose (Gy)	GATE Dose (Gy)	Ratio GATE/OLINDA
1	6.3 ± 1.5	6.6 ± 1.9	1.05
2	2.1 ± 0.5	2.2 ± 0.8	1.05
3	3.1 ± 0.8	3.0 ± 0.9	0.97
4	3.2 ± 0.8	3.3 ± 1.3	1.03
5	2.9 ± 0.7	3.0 ± 1.0	1.03
6	3.0 ± 0.7	3.1 ± 1.1	1.03
7	2.9 ± 0.7	2.8 ± 0.9	0.97
8	1.6 ± 0.3	1.7 ± 0.7	1.06
9	3.8 ± 0.9	4.0 ± 1.6	1.05
10	2.8 ± 0.7	2.7 ± 0.8	0.96

dose values and the raw data images can be interpreted as dose-rate values and images. In Table 8.8, the total volumes and activities of the kidneys of the 10 patients selected for the comparison are presented.

The resulting dose rates obtained for each acquisition time point (1h, 24h and 48h after the administration) were plotted as a function of time. Dose-rate curves were fitted via mono- or bi-exponential fit curves depending on the specific uptake of the organ or tumor. The integral from t=0 to infinite of the curves determined the absorbed dose to the kidneys.
Finally, since the female and male reference phantoms have kidneys mass of 275 g (261.9 ml volume) and 310 g (295.3 ml volume) respectively, dose results were scaled basing on the actual mass of patients kidneys. Specifically, the dose contribution by β were scaled linearly with the mass, while the γ contribution was scaled with the cube root of the organ mass as described by Stabin in the OLINDA functioning [[87]]. Absorbed dose results obtained with GATE compared to those obtained with OLINDA/EXM are shown in Figure 8.3 and Table 8.9.

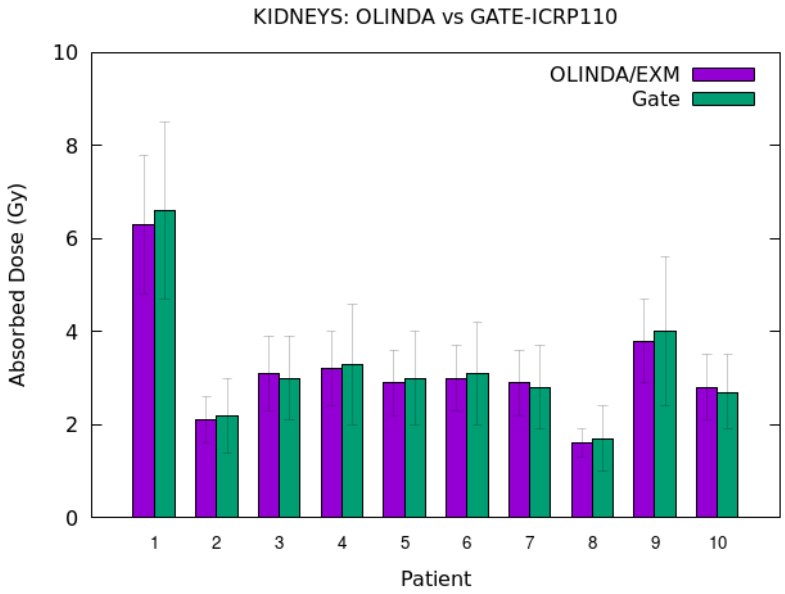

Figure 8.3: Absorbed dose to kidneys obtained with GATE and ICRP 110 phantoms compared with those obtained with OLINDA/EXM.

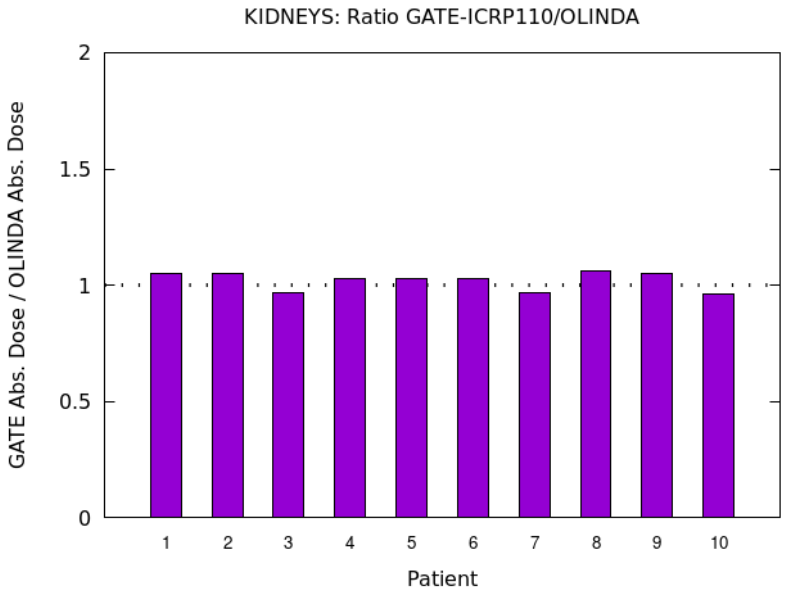

Figure 8.4: Ratios between the absorbed dose to kidneys obtained with GATE using the ICRP 110 phantoms and those obtained with OLINDA/EXM.

As presented in Table 8.9 and Figures 8.3 and 8.4, dose values are in a good agreement with those obtained with the OLINDA/EXM. Even though the ratios between GATE and OLINDA results range from 0.90 to 1.19 ($mean \pm SD = 1.05 \pm 0.09$), absorbed doses to kidneys for all patients are compatible within the associated error.

Thus, using the GATE code for radiation transportation and absorbed dose calculation by imposing the same assumptions as those used in the study of the previous chapter (self-irradiation only, uniform activity distribution, computed dose as average over the whole target

organ) the same results were obtained.

8.5 Image-based Patient Dosimetry Results

The GATE Monte Carlo code validated with the male and female adult reference voxel models was used for the calculation of absorbed dose to kidneys and tumor lesions based on the CT and SPECT images, thus to perform image-based dosimetry. For this purpose, the reconstructed CT images of each time point were used as the attenuation map and as the scoring voxels matrix, while the SPECT images as the activity source voxel maps. Thus, not only the activity inside the VOI of the kidneys and the tumors were taken into account for the calculation, but rather the whole activity distribution inside the 3D images.

The SPECT/CT images acquired at 1h, 24h and 48h after the ^{177}Lu-DOTATOC administration are images of the patients torso, approximately ranging from the pelvis to the upper chest (see Figure 8.5). The implicit assumption is thus that the activity distributions outside this patients portion give a negligible contribution to the absorbed dose evaluation for kidneys and tumor lesions.

As a preliminary procedure for the calculation, the CT and SPECT Dicom images were converted into Analyze file format images composed of header plus raw data files. For the attenuation map, the Hounsfield Unit (HU) values of the CT images were converted into density values, hence into a material composition. For the activity map, the counts in each voxel of the SPECT images were linearly converted into activity values via the CF of the Symbia Intevo gamma camera.

Table 8.10 shows the volumes of the 10 tumor lesions considered together with the accumulated activities at 1h, 24h and 48h after the ^{177}Lu-DOTATOC administration. Data regarding kidneys are shown in Table 8.8.

The same scoring procedure used for the validation with the ICRP reference voxel phantoms was performed for each time point thus obtaining dose-rate voxel matrices for the 1h, 24h

Table 8.10: Tumors data of the 10 patients. Volumes and activity at the three different time points after the ^{177}Lu-DOTATOC administration.

Patient	Volume (ml)	1h Activity (MBq)	24h Activity (MBq)	48h Activity (MBq)
1	18	17.3 ± 3.5	20.2 ± 4.1	14.4 ± 2.9
2	111	120.2 ± 16.0	135.4 ± 18.0	104.4 ± 13.9
3	76	65.1 ± 10.3	95.3 ± 15.5	83.6 ± 13.2
4	26	10.1 ± 1.9	7.9 ± 1.5	5.9 ± 1.1
5	18	18.2 ± 2.6	20.3 ± 2.9	16.0 ± 2.3
6	29	41.5 ± 5.5	42.2 ± 5.6	34.9 ± 4.6
7	27	15.6 ± 2.8	23.1 ± 4.2	16.9 ± 3.1
8	5	0.68 ± 0.07	0.55 ± 0.05	0.48 ± 0.04
9	16	38.8 ± 5.8	63.1 ± 9.4	45.8 ± 6.9
10	5	0.07 ± 0.01	0.10 ± 0.02	0.08 ± 0.02

Table 8.11: Absorbed dose results to kidneys and tumors obtained with GATE and the SPECT/CT images for the 10 patients compared with those obtained with OLINDA/EXM.

	Kidneys Dose (Gy)			Tumors Dose (Gy)		
Patient	OLINDA	GATE	Ratio GATE/OLINDA	OLINDA	GATE	Ratio GATE/OLINDA
1	6.3 ± 1.5	8.1 ± 2.7	1.29	7.8 ± 1.9	8.3 ± 2.9	1.06
2	2.1 ± 0.5	3.2 ± 1.0	1.52	14.0 ± 2.7	12.0 ± 3.4	0.86
3	3.1 ± 0.8	3.6 ± 1.0	1.16	13.4 ± 2.8	15.7 ± 3.7	1.17
4	3.2 ± 0.8	4.0 ± 1.4	1.25	3.6 ± 0.8	2.9 ± 0.8	0.81
5	2.9 ± 0.7	3.6 ± 1.0	1.24	10.8 ± 2.2	4.2 ± 1.2	0.39
6	3.0 ± 0.7	3.7 ± 1.1	1.23	7.9 ± 2.0	9.0 ± 3.1	1.14
7	2.9 ± 0.7	4.1 ± 1.5	1.41	9.0 ± 2.1	7.4 ± 2.3	0.82
8	1.6 ± 0.3	2.1 ± 0.6	1.31	2.6 ± 0.7	2.8 ± 0.7	1.08
9	3.8 ± 0.9	3.9 ± 1.7	1.03	29.5 ± 6.1	20.3 ± 4.1	0.69
10	2.8 ± 0.7	2.7 ± 0.7	0.96	9.1 ± 2.2	12.4 ± 3.1	1.36

and 48h studies. The resulting raw data files were imported into the 3D Slicer software together with the RT Structures representing the contour over the CT map of tumor lesions and kidneys [[101]]. Figure 8.5 shows an example of tumor lesion and kidneys contour. In this way, the same volumes as those used for the calculation with OLINDA/EXM were taken into account for the absorbed dose evaluation. Finally, the dose-rate values were plotted as a function of time and fitted via mono- or bi-exponential curves and then integrated from t=0 to infinite to determine the absorbed dose to the kidneys and tumor lesions.

The comparison of the results obtained with the image-based Monte Carlo and those obtained with OLINDA/EXM are presented in Table 8.11 and shown in Figure 8.6. Figure 8.7 shows the ratios between absorbed dose to kidneys (top) and to tumors (bottom) obtained with GATE using the SPECT/CT images of the patients and those obtained with OLINDA/EXM.

As presented in Table 8.11 and Figures 8.6 and 8.7, absorbed dose to kidneys calculated with GATE and the SPECT/CT images of the patients result higher on average than those calculated with OLINDA/EXM (ratios range from 0.96 to 1.52, $mean \pm SD = 1.24 \pm 0.17$).

Figure 8.5: Patient 9 CT and SPECT images imported into 3D Slicer with the RT structures of kidneys (yellow, top) and the tumor (red, bottom).

On the other hand, relative differences in the calculation of absorbed dose to tumors have a various behavior, with ratios ranging from 0.39 to 1.36 ($mean \pm SD = 0.94 \pm 0.28$).

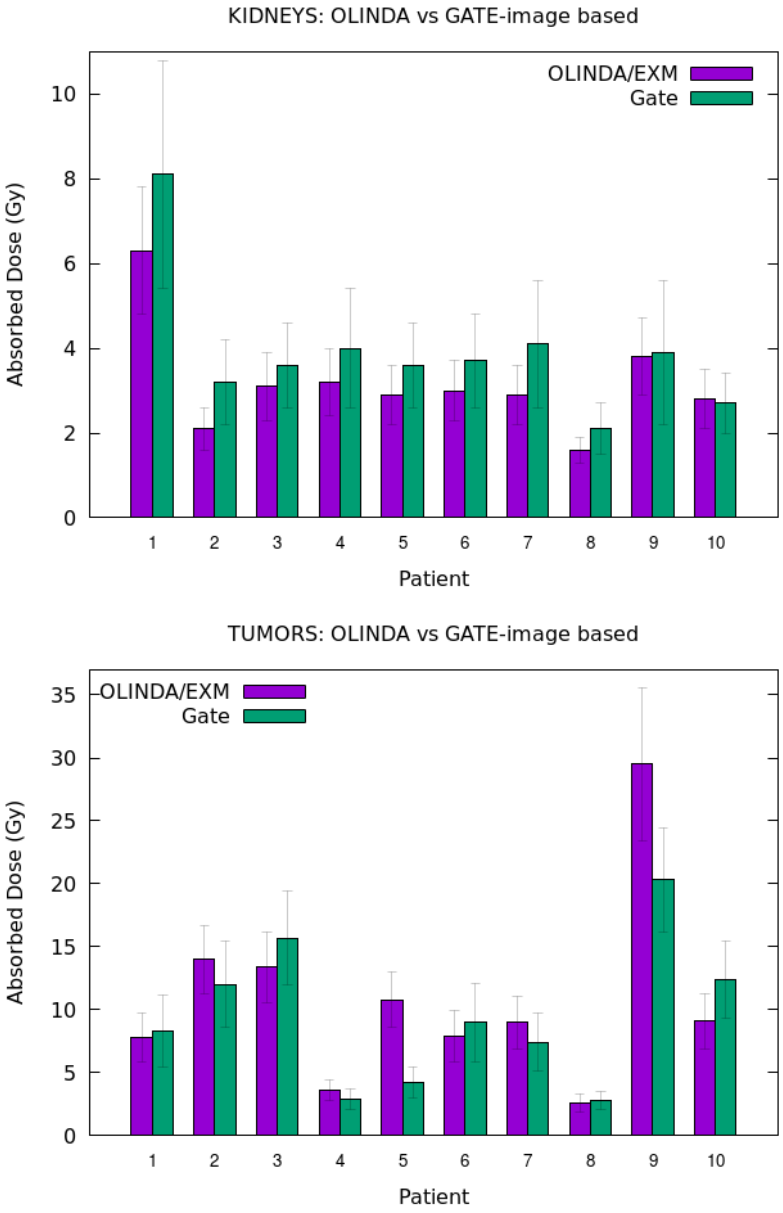

Figure 8.6: Absorbed dose to kidneys (top) and to tumors (bottom) obtained with GATE using the SPECT/CT images of the patients and those obtained with OLINDA/EXM.

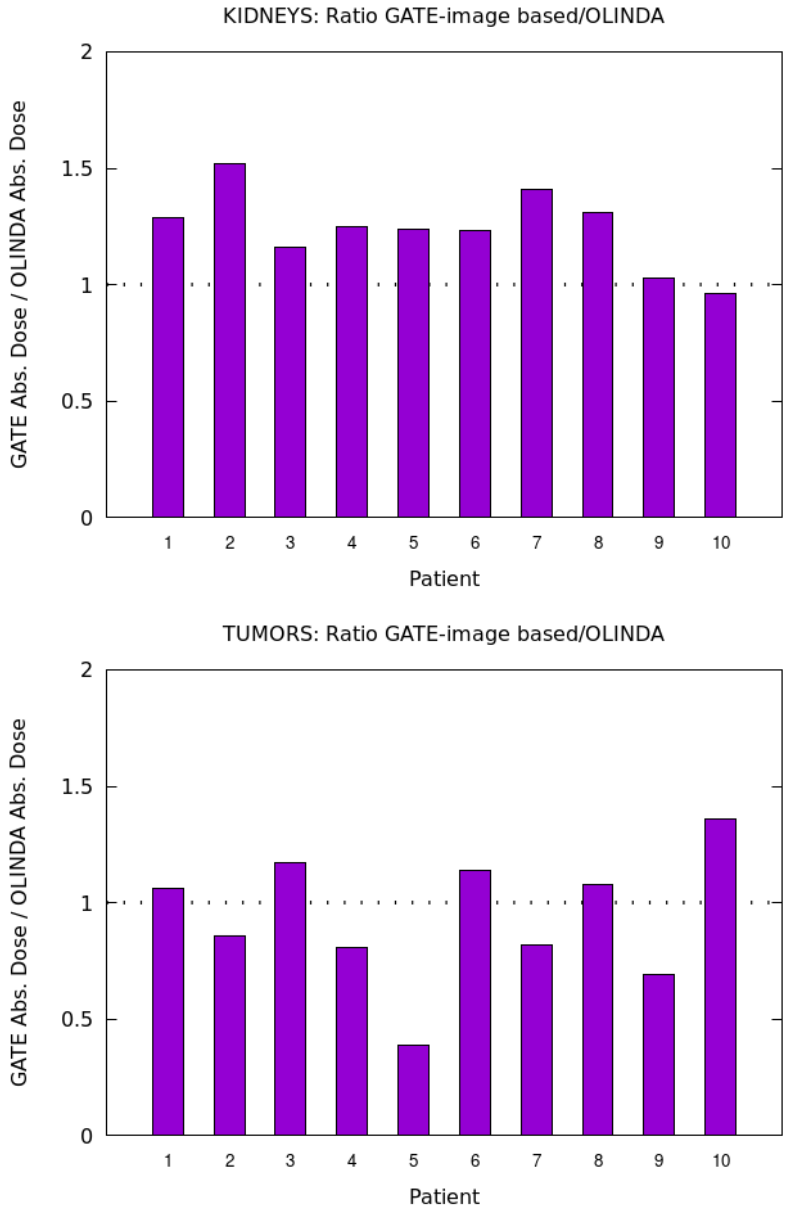

Figure 8.7: Ratios between absorbed dose to kidneys (top) and to tumors (bottom) obtained with GATE using the SPECT/CT images of the patients and those obtained with OLINDA/EXM.

8.6 Conclusions

A Monte Carlo code for the calculation of absorbed dose to target tissues from user-defined activity distributions in source tissues was implemented with GATE. The code was validated with the use of the ICRP110 male and female computational phantoms by deriving the specific absorbed fractions (SAFs) for monoenergetic photons and electrons ($50\,keV$, $100\,keV$, $500\,keV$, $1\,MeV$) for some target-source organ couples. Results were then compared with those published in Hadid *et al* [[97]] and with Villoing *et al* [[98]]. A perfect agreement was found, thus validating the GATE code.

The GATE code was then used for two different purposes. First, using the same assumptions made by the MIRD S-values determined at an organ level (i.e.: uniform activity distribution in the source organ, absorbed dose is an average over the whole target organ, see 5.1.3) and the assumptions used in OLINDA/EXM for our evaluation of absorbed dose to patients undergoing PRRT (i.e.: only self-irradiation for organs and tumors, see 7), the GATE code was used on 10 patients' data to reproduce the same kidneys dosimetry at the organ level. Results are in perfect agreement, with differences under 5%.

Then, the GATE code was used to perform patient-specific dosimetry for both kidneys and tumors. By exploiting the SPECT and CT acquisitions of the 10 patients, absorbed dose was assessed via image-based calculations. CT scans were used as attenuation maps, and SPECT images as activity distributions.
The comparison between the values obtained with GATE and those obtained with OLINDA/EXM shows differences, with ratios between the absorbed dose values (GATE/OLINDA) ranging from 0.96 to 1.52 for kidneys, and from 0.39 to 1.36 for tumors. The variabilities in the dose calculation could be due to several contributions. Firstly, while OLINDA/EXM uses standard human phantoms, the use of the reconstructed CT scans of the patients as attenuation map allows to take into account the specific morphology of the patients organs. Secondly, OLINDA/EXM is based on the organ-level MIRD schema therefore assumes a homogeneous activity distribution inside the source organ (see 5.1.3), whereas the use of the reconstructed SPECT images of the patients allow to consider the actual activity distribution inside the source organ. Particularly for tumors, differences are substantial in some patients: a further approximation in the OLINDA calculation is introduced by the sphere model, i.e. considering

tumors as spheres of homogeneous activity distribution. Finally, while the dose calculation with OLINDA requires the contouring of specific VOIs to use as source tissues thus considers only a portion of the activity distribution surrounding the target organ, simulations performed with the patients images take in consideration all the activity distribution inside the field of view of the SPECT images.

Since the image-based absorbed dose calculation at voxel level takes into account factors that are neglected by the evaluation at the organ level, it could be considered being more precise and more preferable for a clinical use. Disadvantages that have to be taken into account and that could restrain its application in a dosimetry procedure routine, though, are the time-consuming and CPU-intensive computations required.
Next chapter will show a comparison of the results obtained with both OLINDA/EXM and the GATE code with two commercial softwares that implement the voxel S-values (VSV) approach. As discussed in Chapter 5, the voxel S-value approach offers a convenient and rapid tool for voxel-scale dosimetry and avoids the need to perform CPU-intensive calculations. It imposes less restraints that the organ-level dosimetry but cannot take into account for inhomogeneities in the attenuation map.

Chapter 9

Dose Calculation with Voxel S values

The image data of the 10 patients studied with GATE Monte Carlo were used for the calculation with the voxel S values method. For this purpose, two softwares were taken into account for the calculation: PLANET®Dose (version 3.1.1) from DOSIsoft company and MIM SurePlan^{TM}MRT (version 6.9.3) from MIM Software company.

9.1 PlanetDose

The Planet®Dose software provides pre & post-implementation dosimetry, estimation of time-integrated activity. It offers a complete integration of oncology features (PLANET Onco), with versatile solutions for the whole clinical workflow.

For the dose calculation of ^{177}Lu, it provides multi-time points elastic registration, automatic deformable propagation of VOI across times, residence time calculation, dose computation based on voxel-level analysis, Voxel S-Values (VSVs) dose kernel convolution algorithm

VSVs were generated using the MC radiation transport code MCNPX (ORNL), using the mesh tally card. The rectangular mesh tally is used to compute the absorbed dose to each voxel by building a regularly spaced mesh. The source is defined as a voxel, in which the particle emission location and emission angle are randomly sampled. Particles are tracked in the targeted material (reported at $1.04 g\,cm^{-3}$ by the International Commission on Radiation

Units and Measurements [[103]], and the deposited energy is recorded in each voxel defined by rectangular mesh tally. The average absorbed dose per simulated particle is calculated in $MeV\,cm^{-3}$ and then converted to $mGy\,MBq^{-1}\,s^{-1}$ to be used as a VSV kernel. For electron transport, the Integrated TIGER Series mode, which provides better energy binning than the MCNP default mode, is used [[104]], and an electron cutoff energy of 10 keV is applied. The radionuclide decay schemes used were those published by Eckerman and Endo [[105]].

These VSVs can thus be used for dose calculation following the MIRD schema: for a given target voxel ($voxel_k$), its average absorbed dose is calculated as the summed contribution from all N voxels ($voxel_h$), with each contribution given as the product of time-integrated activity and the voxel-to-voxel S value:

$$\overline{D} = \sum_{h=0}^{N} \tilde{A}_{voxel_h} \cdot S(voxel_k \leftarrow voxel_h) \tag{9.1}$$

Equation 9.1 is implemented as a discrete convolution using a fast Hartley transform. The VSV matrix, computed for given radionuclide and voxel dimensions, is used as a kernel to convolve the cumulated activity map and obtain the average absorbed dose for each voxel of the cumulated activity map.

9.1.1 Calculation

Rigid registration was used to align the 1h SPECT and CT studies. The 24h and 48h SPECT and CT studies were then registered based on the 1h studies. In order to maintain the same volumes for the dose evaluation, the RT contour structures performed for kidneys and tumor lesions in the FENET study were imported. Figure 9.1 shows the contours of left and right kidney and a tumor lesion.

The dose-rate values calculated by the software were then plotted as a function of time and fitted via mono- or bi-exponential fit in order to calculate the absorbed dose as the integral of the fitting curve as shown in Figure 9.1.

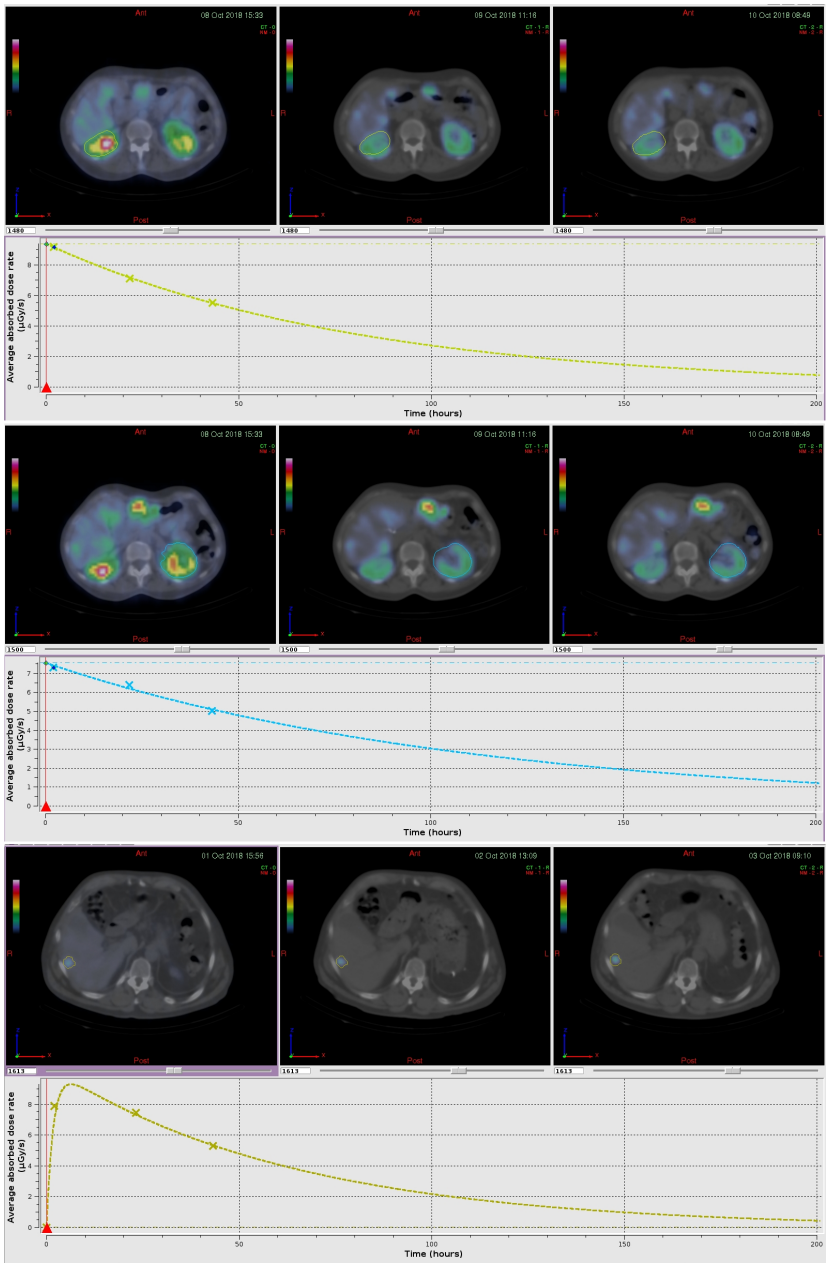

Figure 9.1: PlanetDose: right kidney (top), left kidney (middle) and tumor lesion (bottom) contours displayed on the transverse views of the coregistered SPECT/CT studies at 1h, 24h and 48h. The dose-rates as a function of time for each are also displayed below each VOI.

9.2 MIM SurePlan

MIM SurePlan MRT performs voxel-based absorbed dose calculation using the patient's own anatomy and calculates dose using the voxel s-value (VSV) schema in MIRD Pamphlet No. 17 [[51]]. Tools for ^{177}Lu approved therapies are available for clinical use and tools for other radionuclide therapies are available for research use.

The area under curve (AUC) calculation method in MIM SurePlan MRT provides a voxel-by-voxel curve fitting and integration. Curve fitting is performed by minimizing the squared differences between the curve from the user selected function and the observed data points. The time-integrated activity values generated from the AUC method are then used for the calculation of absorbed dose.

The physical density map is created from a CT scan using a method that is similar to generating an attenuation map from a CT. A bi-linear fit formula is applied that maps HU values from the CT scan to physical density values.

The Voxel S value convolution (VSV) method for dose calculation in MIM SurePlan MRT is an approach based on the schema in MIRD Pamphlet 17 for nonuniform distribution of radioactivity. MIRD Pamphlet 17 has applied Monte Carlo methods for radionuclide sources in water to calculate dose deposited in 3x3x3 mm target voxels surrounding a uniform source of the radionuclide in the central voxel. MIM SurePlan MRT VSV kernels [[106]] include ^{177}Lu which was derived in-house from Monte Carlo simulations with MCNP 6.2 [[107]].

Rather than creating a new Monte Carlo kernel for the voxel size of each image, the SPECT image is resampled to the size of the kernel (3x3x3 mm voxels) using trilinear interpolation. Specifically, the intensity value at (x,y,z) is approximated by taking each of the eight closest data points and multiplying its intensity value by a weight that is based on the distance in each dimension from (x,y,z), then summing the weighted intensity values. The intensity value at each new voxel grid location is then computed by performing trilinear interpolation at the corresponding location in the original image.

9.2.1 Calculations

Similarly to the procedure performed with PlanetDose, rigid registration was used to align the 1h SPECT and CT studies and the 24h and 48h SPECT and CT studies were then registered based on the 1h studies. The RT contour structures were then imported. Figure 9.2 shows the contours of left and right kidney and a tumor lesion.

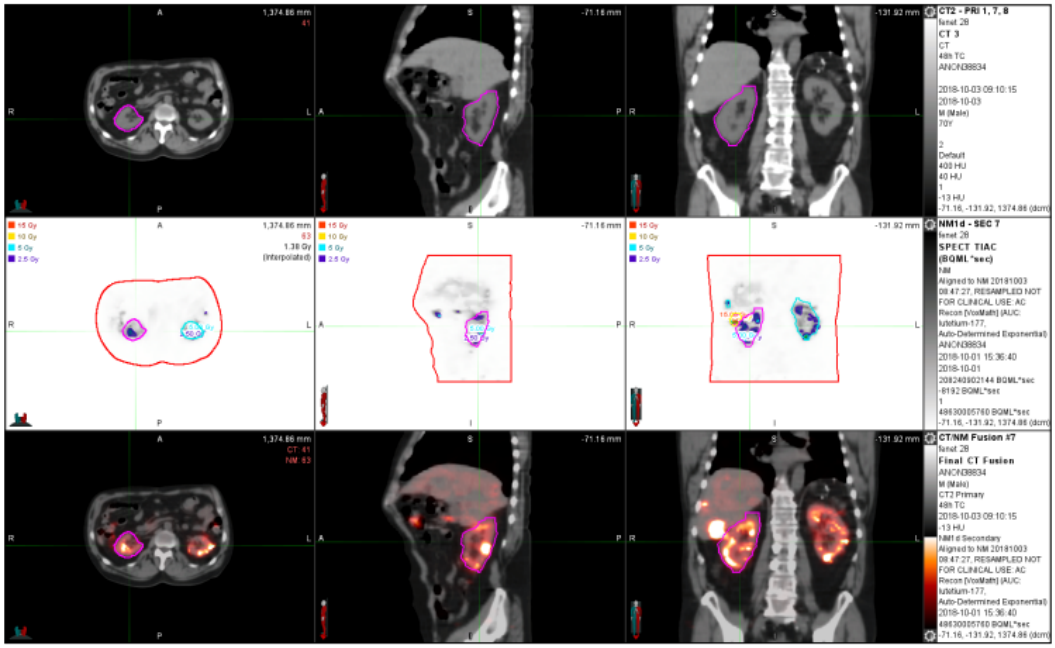

Figure 9.2: PlanetDose: top row

Table 9.1: Dose results obtained with PlanetDose and MIM SurePlan MRT compared with the OLINDA/EXM results.

	Kidneys (Gy)			Tumors (Gy)		
Patient	OLINDA/EXM	Planet	MIM	OLINDA/EXM	Planet	MIM
1	6.3 ± 1.5	9.4	7.2 ± 2.7	7.8 ± 1.9	9.8	6.1 ± 2.3
2	2.1 ± 0.5	3.1	3.0 ± 1.1	14.0 ± 2.7	16.1	11.1 ± 2.5
3	3.1 ± 0.8	4.5	3.0 ± 1.2	13.4 ± 2.8	17.7	16.0 ± 3.5
4	3.2 ± 0.8	5.3	3.7 ± 1.3	3.6 ± 0.8	1.2	2.7 ± 1.4
5	2.9 ± 0.7	2.7	4.1 ± 1.5	10.8 ± 2.2	1.8	4.5 ± 1.6
6	3.0 ± 0.7	5.6	3.7 ± 1.6	7.9 ± 2.0	9.4	9.2 ± 2.4
7	2.9 ± 0.7	5.7	3.8 ± 1.2	9.0 ± 2.1	8.6	4.3 ± 1.7
8	1.6 ± 0.3	2.6	2.2 ± 0.9	2.6 ± 0.7	3.4	2.7 ± 1.2
9	3.8 ± 0.9	5.6	3.5 ± 1.7	29.5 ± 6.1	21.2	17.9 ± 3.0
10	2.8 ± 0.7	3.1	2.4 ± 0.8	9.1 ± 2.2	14.2	11.2 ± 2.7

9.3 Results

The results of the dose calculation are shown in Table 9.1 and Figure 9.3. Table 9.2 and Figure 9.4 show the ratios between the absorbed doses calculated with PlanetDose and those calculated with OLINDA/EXM, and the ratios between the absorbed doses calculated with MIM and those calculated with OLINDA/EXM.

Errors associated to the absorbed dose to kidneys and tumors were provided by the MIM software calculation but not by the PlanetDose software. No errors are then associated to the absorbed dose values calculated with PlanetDose and displayed hereafter.

Table 9.2: Ratios between dose results obtained with PlanetDose and OLINDA/EXM and between MIM SurePlan MRT and OLINDA/EXM.

	Kidneys (Gy)		Tumors (Gy)	
Patient	Ratio Planet/OLINDA	Ratio MIM/OLINDA	Ratio Planet/OLINDA	Ratio MIM/OLINDA
1	1.49	1.14	1.26	0.78
2	1.48	1.43	1.15	0.79
3	1.45	0.97	1.32	1.19
4	1.66	1.16	0.33	0.75
5	0.93	1.41	0.17	0.42
6	1.87	1.23	1.19	1.16
7	1.97	1.31	0.96	0.48
8	1.63	1.38	1.31	1.04
9	1.47	0.92	0.72	0.61
10	1.11	0.86	1.56	1.23

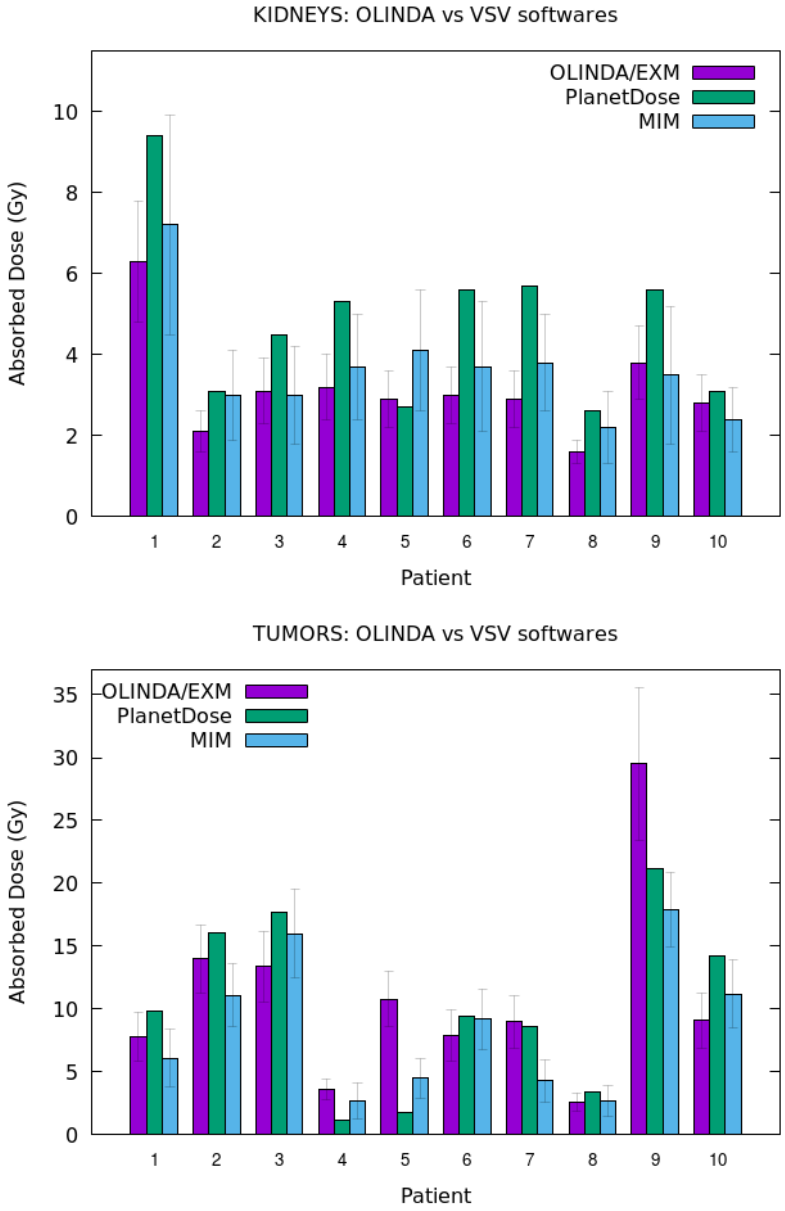

Figure 9.3: Absorbed dose to kidneys (top) and to tumors (bottom) obtained with PlanetDose and MIM compared with those obtained with OLINDA/EXM.

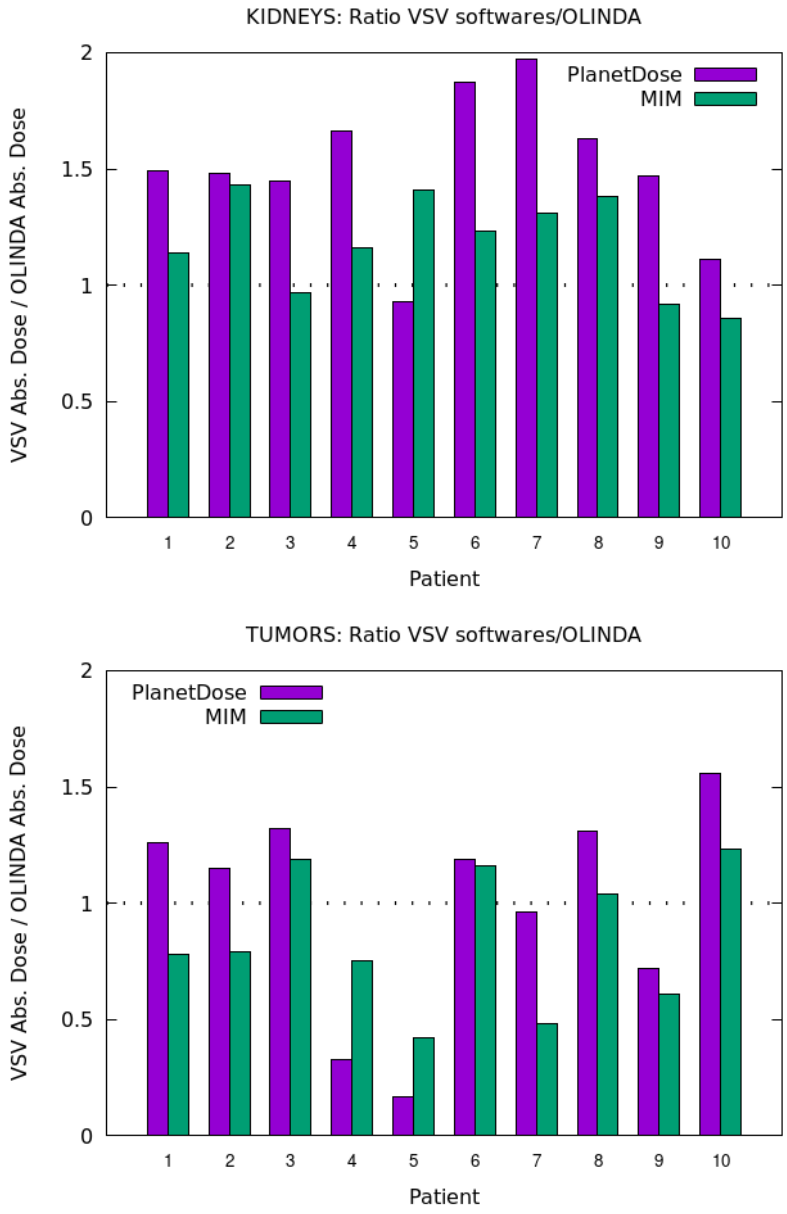

Figure 9.4: Ratios between absorbed dose to kidneys (top) and to tumors (bottom) obtained with PlanetDose and OLINDA/EXM and between MIM and OLINDA/EXM.

As presented in Tables 9.1 and 9.2 and Figures 9.3 and 9.4, absorbed dose to kidneys calculated with PlanetDose or MIM and the SPECT/CT images of the patients result higher on average than those calculated with OLINDA/EXM, with ratios ranging from 0.93 to 1.97 ($mean \pm SD = 1.50 \pm 0.31$), and from 0.86 to 1.43 $mean \pm SD = 1.18 \pm 0.21$, respectively. Likewise the calculations with GATE, relative differences in the calculation of absorbed dose to tumors have a various behavior, with ratios ranging from 0.17 to 1.56 ($mean \pm SD = 1.00 \pm 0.45$) for PlanetDose and ranging from 0.42 to 1.23 ($mean \pm SD = 0.85 \pm 0.30$) for MIM. The variabilities in the absorbed dose calculations between the two softwares could be due to their different methods in assessing the S-values.

Table 9.3: Ratios between absorbed dose results obtained with PlanetDose and MIM SurePlan MRT compared with the GATE results [8.11].

	Kidneys (Gy)		Tumors (Gy)	
Patient	Ratio Planet/GATE	Ratio MIM/GATE	Ratio Planet/GATE	Ratio MIM/GATE
1	1.16	0.89	1.18	0.73
2	0.97	0.94	1.34	0.93
3	1.25	0.83	1.13	1.02
4	1.33	0.93	0.41	0.93
5	0.75	1.14	0.43	1.07
6	1.51	1.00	1.04	1.02
7	1.39	0.93	1.16	0.58
8	1.24	1.05	1.21	0.96
9	1.44	0.90	1.04	0.88
10	1.15	0.89	1.15	0.90

Finally, the dose results obtained with MIM and PlanetDose were compared to those obtained with the GATE Monte Carlo code using the SPECT/CT images of the patients. Results are displayed in Figure 9.5. Table 9.3 and Figure 9.6 show the ratios between the absorbed doses obtained with the two calculation methods.

Absorbed dose to kidneys calculated with PlanetDose result higher on average than those calculated with GATE (ratios ranges from 0.75 to 1.51, $mean \pm SD = 1.22 \pm 0.23$) but their values result all compatible, except for patient 6, to those calculated with GATE within the associated errors. Absorbed dose to kidneys calculated with MIM result all compatible within the associated errors to those calculated with GATE (ratios range from 0.83 to 1.14, $mean \pm SD = 0.95 \pm 0.09$).

Absorbed dose to tumors have a various behavior when comparing GATE results with those obtained with voxel S-values softwares. Ratios range from 0.41 to 1.34, $mean \pm SD = 1.01 \pm 0.32$ for PlanetDose and range from 0.58 to 1.07, $mean \pm SD = 0.90 \pm 0.15$ for MIM. All absorbed dose measurements to tumors calculated with GATE and MIM are compatible within the associated errors.

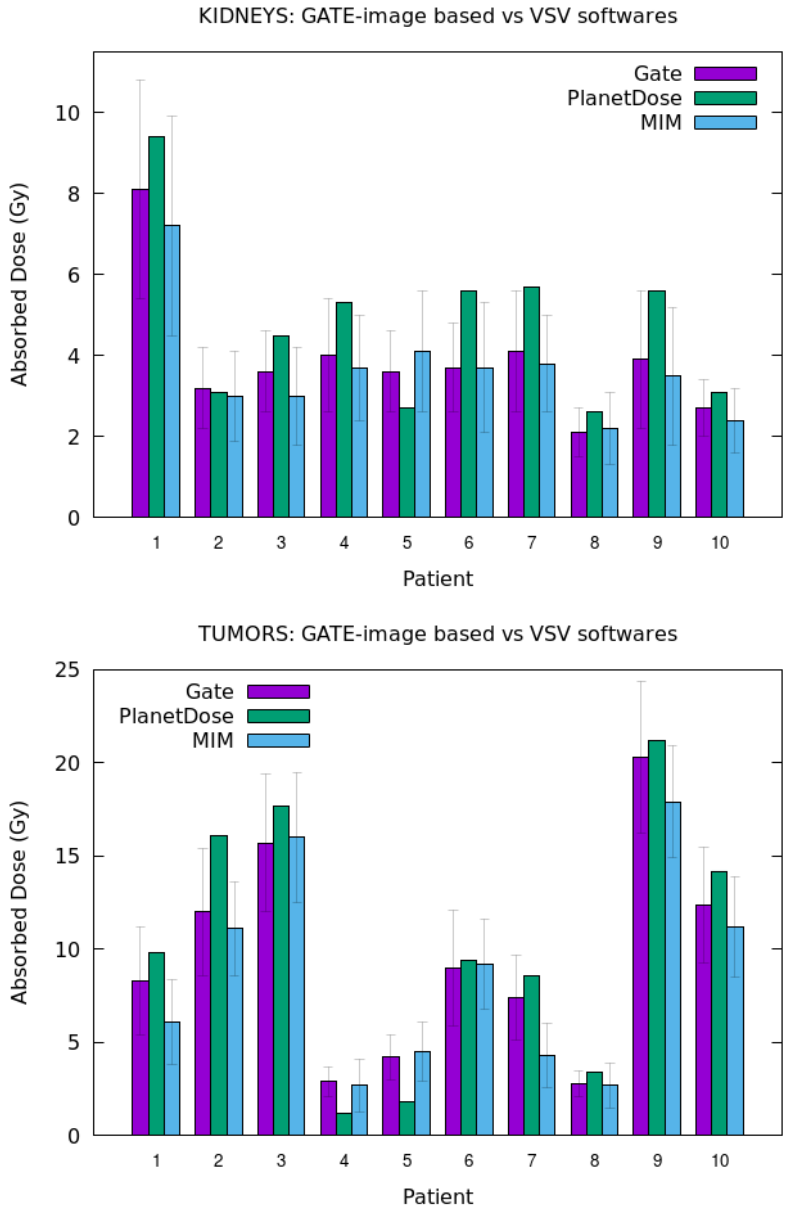

Figure 9.5: Absorbed dose to kidneys (top) and to tumors (bottom) obtained with PlanetDose and MIM compared with those obtained with GATE [8.11].

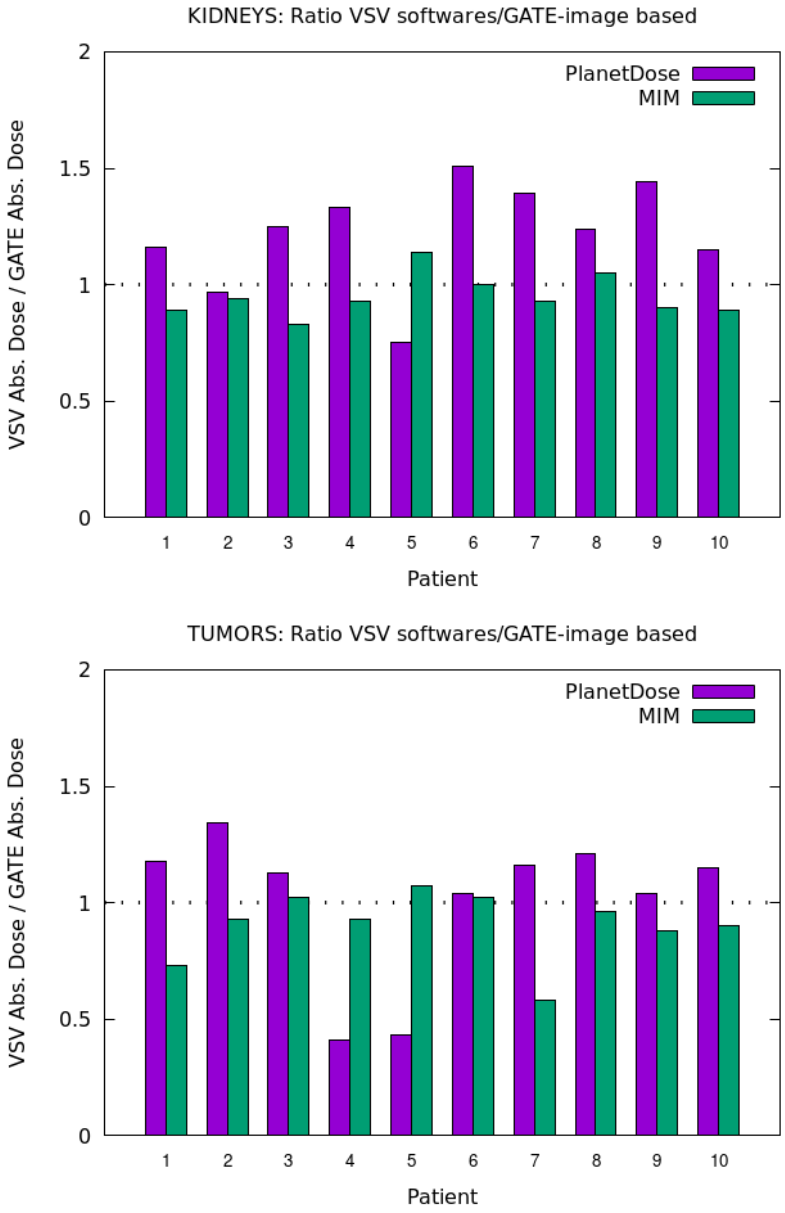

Figure 9.6: Ratios between absorbed dose to kidneys (top) and to tumors (bottom) obtained with PlanetDose and GATE and between MIM and GATE [8.11].

9.4 Conclusions

Two commercial softwares, PLANET®Dose (version 3.1.1) from DOSIsoft company and MIM SurePlan^{TM}MRT (version 6.9.3) from MIM Software company, were exploited for the absorbed dose calculation with the voxel S-values convolution (VSV) method. SPECT and CT images of 10 selected patients were used for the purpose, in order to compare absorbed dose evaluation for kidneys and tumors with the results obtained using OLINDA/EXM 7 and the GATE code 8.

Absorbed dose to kidneys calculated with VSV have a generally good agreement with those calculated with GATE, resulting all compatible within the associated errors except for one case. Ratios between the results obtained range from 0.75 to 1.51 for PlanetDose/GATE, and from 0.83 to 1.14 for MIM/GATE.
Absorbed dose to tumors have instead a more various behaviour, with ratios PlanetDose/GATE ranging from 0.41 to 1.34 and MIM/GATE 0.58 to 1.07.
All absorbed dose measurements calculated with PlanetDose are all compatible with those calculated with MIM.

The variabilities in the absorbed dose results are due to several contributions, and the different assumptions made in the calculation play an important part in these differences. The comparison between the results obtained with PlanetDose, MIM and GATE using the same CT and SPECT images show how the calculation itself plays an important role in these differences, namely the code used for the radiation transport and the energy deposition as well as the method for the assessment of the S-values.

Conclusions

The evaluation of the imparted dose to organs and tumors is a crucial step in the treatment planning for patients undergoing TRT. This is a particularly difficult task, though, since it relies on the knowledge of patients morphological information and of the specific distribution of the activity. Moreover, the evaluation of the deposited energy in the target organs and tumors can not be detected directly and depends entirely on the use of transportation and energy deposition simulations. For all these reasons, the necessity to have a reliable computed simulation tool is highlighted in the nuclear medicine framework.

SPECT imaging devices used in nuclear medicine introduce considerable errors in the activity evaluation inside the patients body. For the purpose of guaranteeing the best achievable image quality and a correct activity evaluation, the best parameters for reconstruction and correction of SPECT-CT studies have been experimentally examined for ^{99m}Tc and ^{177}Lu radioisotopes with a Siemens Symbia Intevo Excel gamma camera. Results obtained are in a good agreement with data from the Symbia Intevo data sheet. As an additional tool, the SIMIND Monte Carlo code was exploited to reproduce the gamma camera parameters. Results obtained are in a good agreement with the experimental values, proving SIMIND to be an useful tool to simulate gamma cameras, using several radionuclides for different medical purposes and treatments.

Dosimetric evaluations have been performed on 80 patients enrolled in the FENET 2016 phase II perspective study. The protocol includes patients affected by various forms of NET and is based on five PRRT cycles consisting in five administrations of ^{177}Lu-DOTATOC or hree administrations of ^{177}Lu-DOTATOC interspersed with two administrations of 90Y-DOTATOC. The administered activities at the 1st cycle were chosen based on the patient's status and on the experience reported by the clinicians, while the subsequent administration were also guided by the results of dosimetry. Absorbed dose was assessed for tumors and organs at risk, that is

for kidneys and tumor lesions. Results show a high inter-patient variability in the absorbed dose per administered activity for organs at risk and particularly for tumors. Results of absorbed dose per administered activity with ^{177}Lu-DOTATOC resulted in $0.6 \pm 0.2\,Gy/GBq$ $[0.1 - 1.4\,Gy/GBq]$ for kidneys, $0.02 \pm 0.01\,Gy/GBq$ $[0.001 - 0.090\,Gy/GBq]$ for bone marrow and $2.2 \pm 1.6\,Gy/GBq$ $[0.1 - 9.4\,Gy/GBq]$ for tumors. Values obtained for both organs at risk and tumors are in good agreement with data known from literature.

Dose assessment within the FENET 2016 study was performed with OLINDA/EXM, a software that exploits standard human male and female phantoms for the calculation. In order to accomplish the COUNCIL DIRECTIVE 2013/59/EURATOM of the European Union, that fixes the need for individual and personalized dosimetry for patients treated with radionuclides, the study for a patient-tailored dosimetry was pursued with the use of voxel dosimetry. A Monte Carlo code was developed with GATE in order to evaluate the absorbed dose to kidneys and tumors starting from the SPECT and CT three-dimensional images acquired on the patients. Ten patients from the FENET 2016 study were selected for the dose calculation to kidneys and tumors with the Monte Carlo code. The code was preliminarly used with the ICRP110 male and female standard human phantoms in order to validate its proper calculation. Final results were studied with the CT and SPECT images acquired after the first administration cycle of ^{177}Lu-DOTATOC. Dose results obtained for kidneys are higher than those obtained withe OLINDA/EXM, with ratios between the values obtained with GATE and those obtained with OLINDA ranging from 1.03 to 1.52, with only one case of lower dose with a ratio of 0.96 (total, $mean \pm SD = 1.24 \pm 0.17$). On the other hand, absorbed dose to tumors have a various behavior, with ratios ranging from 0.39 to 1.36 ($mean \pm SD = 0.94 \pm 0.28$).

A further comparison was performed with two softwares based on the voxel S-values approach. PLANET®Dose from DOSIsoft company and MIM SurePlan^{TM} MRT from MIM Software company were used with the CT and SPECT images from the same ten patients studied with GATE Monte Carlo. The assessment of absorbed dose consists in the convolution of Monte Carlo calculated S-values with the activity map in order to obtain the average absorbed dose for each voxel of the cumulated activity map. Kidneys and tumors were considered for the calculation of absorbed dose. When compared with the results obtained with GATE, the absorbed dose to kidneys calculated with PlanetDose resulted higher on average (ratios ranges from 0.75 to 1.51, $mean \pm SD = 1.22 \pm 0.23$). Absorbed dose to kidneys

calculated with MIM result all compatible within the associated errors to those calculated with GATE (ratios MIM/OLINDA range from 0.83 to 1.14, $mean \pm SD = 0.95 \pm 0.09$). Absorbed dose to tumors have a various behavior when comparing GATE results with those obtained with voxel S-values softwares, with ratios ranging from 0.41 to 1.34 ($mean \pm SD = 1.01 \pm 0.32$) for PlanetDose and from 0.58 to 1.07 ($mean \pm SD = 0.90 \pm 0.15$) for MIM. All absorbed dose measurements to tumors calculated with GATE and MIM are compatible within the associated errors.

The variabilities in the absorbed dose results are due to several contributions, and the different assumptions made in the calculation play an important part in these differences. The attenuation map and the activity distribution exploited for the calculation are the primary factors, as underlined in the comparison between the results obtained with OLINDA/EXM and GATE. Nevertheless, the comparison between the results obtained with PlanetDose, MIM and GATE using the same CT and SPECT images show how the calculation itself plays an important role in these differences, namely the code used for the radiation transport and the energy deposition as well as the method for the assessment of the S-values.
When considering the different absorbed dose calculation methods for clinical use, one should also take into account the feasibility of the method as a part of the clinical procedure, such as the complexity of the workflow, the required calculation time, the need for powerful processors. With respect to the consolidated OLINDA/EXM workflow, the GATE code provides absorbed dose calculations that take into account patient-specific features neglected in the first method. It is, though, highly time-consuming and requires intensive CPU computations. VSV softwares seem to be a good compromise, since they impose assumptions for the absorbed dose calculations that are less restrictive with respect to the S-values at the organ level and, even though negligent of some informations with respect to the direct Monte Carlo calculations, they do not require CPU-intensive and time-consuming calculations.

The methods and the results presented in this work underline the importance of Monte Carlo simulations in Nuclear Medicine, that are a powerful tool in the pursuit of fully personalized treatment and dosimetry for patients undergoing MRT. Even though further calculations are necessary to establish the viability of the Monte Carlo code developed with GATE as a tool for clinical dosimetry, a patient-specific dose evaluation is crucial for the personalization of the treatment, both in monitoring the efficacy of the therapy and the toxicity to organs at

risk, in planning a specific therapeutic regimen and in predicting those patients who would benefit the most from treatment.

Final aim of the work is having a tool (SIMIND) able to simulate accurately the activity distribution inside the patient body, in order to calculate the dose imparted to each organ from the reconstructed activity distribution and finally to compare the imparted dose with the dose calculated from the true distribution (GATE) so as to implement patient-specific dosimetry.

Future perspectives of the work will be the implementation of a homemade code for voxel-dosimetry using the VSV approach, so as to overcome the limits of the organ-level dosimetry evaluation and the time-consuming requirements of Monte Carlo direct calculations.

Bibliography

[1] IAEA, Radiation biology, Internal Atomic Energy Agency, 2010.

[2] Bailey D, Humm J, Todd-Pokropek A, van Aswegen A, Nuclear medicine physics, IAEA, 2014.

[3] Mozumder A, Hatano Y, Charged Particle and Photon Interactions with Matter: Chemical, Physicochemical, and Biological Consequences with Applications, CRC Press: Boca Raton, FL, USA, 2004.

[4] Kraft G, Radiobiology of Heavy Charged Particles, GSI-Preprint 96-60, 1996.

[5] Hendee WR, Medical radiation physics: roentgenology, nuclear medicine and ultrasound, Chicago, Year Book Medical Publishers, p 115, 1979.

[6] MIT OpenCourseWare - 22.101 Applied Nuclear Physics, 2006.

[7] Terato H, Ide H, Clustered DNA damage induced by heavy ion particles. Biol Sci Space, 18(4):206-15, 2004.

[8] Durante M, Paganetti H, Nuclear physics in particle therapy: a review. Reports on Progress in Physics, 79(9), p.096702, 2016.

[9] 1990 Recommendations of the International Commission on Radiological Protection, The International Commission on Radiological Protection, ICRP Publication 60, Pergamon Press, Oxford, 1991.

[10] Quantities and Units in Radiation Protection Dosimetry, The International Commission on Radiation Units and Measurements, ICRU Report 51, ICRU, Bethesda, 1993.

[11] Kassis A, Therapeutic Radionuclides: Biophysical and Radiobiologic Principles. Seminars in nuclear medicine, 38. 358-66, 2008.

[12] Shakil AS, Rais AA, Pharmacokinetics, Reference Module in Biomedical Sciences, Elsevier, 2018.

[13] Bé MM, Duchemin B, Lamé J, Morillon C, Piton F, Browne E, Chechev V, Helmer R, Schönfeld E, Table de Radionucléides vol. 1. Commissariat à l'Énergie Atomique, DAMRI/LPRI BP 52, F-91193 Gif-sur-Yvette Cedex, France, 1999.

[14] http://www.nucleide.org/, Laboratoire National Henri Becquerel, Nuclear Data Table.

[15] Oronsky B, Ma PC, Morgensztern D, Carter CA. Nothing But NET: A Review of Neuroendocrine Tumors and Carcinomas. Neoplasia, 19(12):991-1002, 2017.

[16] Cives M, Strosberg JR. Gastroenteropancreatic Neuroendocrine Tumors. CA Cancer J Clin, 68(6):471-487, 2018.

[17] Modlin IM, Lye KD, Kidd M. A 5-decade analysis of 13,715 carcinoid tumors. Cancer, 97:934-959, 2003.

[18] Yao JC, Hassan M, Phan A, et al. One hundred years after "carcinoid": epidemiology of and prognostic factors for neuroendocrine tumors in 35,825 cases in the United States. J Clin Oncol, 26(18):3063-72, 2008.

[19] Teunissen JJ, Kwekkeboom DJ, Valkema R et al. Nuclear Medicine Techniques for the imaging and treatment of neuroendocrine tumors. Endocr Relate Cancer, 18 (suppl. 1): S 27-51, 2011.

[20] Hardiansyah D, Maass C, Attarwala AA et al. The role of patient-based treatment planning in peptide receptor radionuclide therapy. Eur J Nucl Med Mol Imaging, 43(5):871-880, 2016.

[21] Anger HO, Scintillation Camera, Review of Scientific Instruments, 29, 27–33, 1958.

[22] Bushberg JT, Seibert JA, Leidholdt EM Jr., Boone JM, The Essential Physics of Medical Imaging, Lippincott Williams Wilkins, 2011.

[23] Cherry SR, Sorenson JA, Phelps ME, Physics in nuclear medicine, Elsevier Health Sciences, 2012.

[24] https://www.healthcare.siemens.com/molecular-imaging/xspect/symbiaintevoexcel

[25] Vickery A, Jørgensen T, de Nijs R, NEMA NU-1 2007 based and independent quality control software for gamma cameras and SPECT. Journal of Physics: Conference Series, 2011.

[26] Ljungberg M, Strand SE, King MA, Monte Carlo calculations in nuclear medicine: Applications in diagnostic imaging, CRC Press, 2012.

[27] Kak AC, Slaney M, Principles of computerized tomographic imaging, IEEE press, 1988.

[28] Liu S, Famcombe TH, Collimator-detector response compensation in quantitative spect reconstruction. In: 2007 IEEE Nuclear Science Symposium Conference Record: 27 October - 3 November 2007; Hawaii, pp. 19–327, IEEE Nuclear Science, 2007.

[29] Dewaraja YK, Frey EC, Sgouros G, Brill AB, Roberson P, Zanzonico PB, Ljungberg M. MIRD pamphlet No. 23: quantitative SPECT for patient-specific 3-dimensional dosimetry in internal radionuclide therapy. J Nucl Med., 53(8):1310-25, 2012.

[30] Bruyant PP, Analytic and iterative reconstruction algorithms in SPECT, Journal of Nuclear Medicine 43 (10), 1343-1358, 2002.

[31] Hudson HM, Larkin RS, Accelerated image reconstruction using ordered subsets of projection data, IEEE transactions on medical imaging 13 (4) 601-609, 1994.

[32] Zeintl J, Vija AH, Yahil A, Hornegger J, Kuwert T, Quantitative accuracy of clinical 99mtc spect/ct using ordered-subset expectation maximization with 3-dimensional resolution recovery, attenuation, and scatter correction, Journal of Nuclear Medicine 51 (6) 921-928, 2010.

[33] Sanders J, Kuwert T, Hornegger J, Ritt P, Quantitative spect/ct imaging of 177 lu with in vivo validation in patients undergoing peptide receptor radionuclide therapy, Molecular Imaging and Biology 17 (4), 585-593. 2015.

[34] Grassi E, Fioroni F, Ferri V, Mezzenga E et al., Quantitative comparison between the commercial software stratos R by philips and a homemade software for voxel-dosimetry in radiopeptide therapy, Physica Medica: European Journal of Medical Physics 31 (1), 72-79, 2015.

[35] Vija AH, Hawman EG, Engdahl JC, Analysis of a spect osem reconstruction method with 3d beam modeling and optional attenuation correction: phantom studies, in: Nuclear

Science Symposium Conference Record, 2003 IEEE, Vol. 4, IEEE, pp. 2662-2666, 2003.

[36] Hawman E, Vija, AH, Daffach R, Manjit R, Flash 3D TM Technology Optimizing SPECT Quality and Accuracy, 2022.

[37] Bailey DL, Willowson KP, Quantitative SPECT/CT: SPECT joins PET as a quantitative imaging modality. Eur J Nucl Med Mol Imaging, ;41(SUPPL. 1):17–25, 2014.

[38] Ritt P, Vija AH, Hornegger J, Kuwert T. Absolute quantification in SPECT. Eur J Nucl Med Mol Imaging, 38(SUPPL. 1):69–77, 2011.

[39] Seret A, Nguyen D, Bernard C. Quantitative capabilities of four state-of-the-art SPECT-CT cameras. EJNMMI Res, 2(1):45, 2012.

[40] Erlandsson K, Buvat I, Pretorius PH, Thomas BA, Hutton BF. A review of partial volume correction techniques for emission tomography and their applications in neurology, cardiology and oncology. Phys Med Biol, 57(21): R119–59, 2012.

[41] Ritt P, Sanders J, Kuwert T, SPECT/CT technology. Clin Transl Imaging 2, 445–457, 2014.

[42] Du Y, Tsui BM, Frey EC, Model-based compensation for quantitative 123I brain SPECT imaging. Phys Med Biol 51:1269–1282, 2006.

[43] Se Young C, Fessler JA, Dewaraja YK, Correction for collimator-detector response in SPECT using point spread function template. IEEE Trans Med Imaging 32:295–305, 2013.

[44] Chang LT, A method for attenuation correction in radionuclide computed tomography. Nucl Sci IEEE Trans, 25:638–43, 1978.

[45] Zaidi H, Hasegawa B, Determination of the attenuation map in emission tomography. J Nucl Med, 44:291–315, 2003.

[46] Jaszczak RJ, Greer KL, Floyd CE et al., Improved SPECT quantification using compensation for scattered photons, J. Nucl. Med. 25, 893–900, 1984.

[47] Hippeläinen E, Tenhunen M, Mäenpää H, Sohlberg A, Quantitative accuracy of (177)Lu SPECT reconstruction using different compensation methods: phantom and patient studies. EJNMMI Res, 6(1):16, 2016.

[48] Loevinger R, Budinger TF, Watson EE, MIRD primer for absorbed dose calculations, Society of Nuclear Medicine, 1988.

[49] Bolch WE, Eckerman KF, Sgouros G, Thomas SR. MIRD pamphlet No. 21: a generalized schema for radiopharmaceutical dosimetry–standardization of nomenclature. J Nucl Med, 50(3):477-84, 2009.

[50] Snyder WS, Ford MR, Warner GG, Watson SB, MIRD Pamphlet 11: S, Absorbed Dose per Unit Cumulated Activity for Selected Radionuclides and Organs, 1975.

[51] Bolch WE, Bouchet LG, Robertson JS, Wessels BW, Siegel JA et al., MIRD pamphlet No. 17: the dosimetry of nonuniform activity distributions–radionuclide S values at the voxel level. Medical Internal Radiation Dose Committee. J Nucl Med, 40(1):11S-36S, 1999.

[52] Cristy M, Mathematical phantoms representing children of various ages for use in estimates of internal dose. Oak Ridge, TN: Oak Ridge National Laboratory, ORNL/NUREG/TM-367, 1980.

[53] Nelson WR, Rogers DWO, Structure and Operation of the EGS4 Code System. In: Jenkins T.M., Nelson W.R., Rindi A. (eds) Monte Carlo Transport of Electrons and Photons. Ettore Majorana International Science Series, vol 38, Springer, Boston, MA, 1988.

[54] Briesmeister JF, MCNP: a general Monte N-particle transport code, version 4C Technical Report No LA-12709-M, Los Alamos, NM: Los Alamos National Laboratory, 2000.

[55] Zaidi H, Relevance of accurate monte carlo modeling in nuclear medical imaging. Med Phys 26, 574–608, 1999.

[56] Ljungberg M, The simind monte carlo program. In: M. Ljungberg, M.A.K. S.E. Strand (ed.) Monte Carlo Calculations in Nuclear Medicine: Applications in Diagnostic Imaging, 2nd edn., pp. 111–128. CRC Press, Boca Raton, 2012.

[57] Ljungberg M, Celler A, Konijnenberg MW, Eckerman KF, Dewaraja YK, Sjögreen-Gleisner K, Mird pamphlet no. 26: Joint eanm/mird guidelines for quantitative 177lu spect applied for dosimetry of radiopharmaceutical therapy. J Nucl Med 57, 151–162, 2016.

[58] Ljungberg M, Absolute quantitation of spect studies. Semin Nucl Med 48, 348–358, 2018.

[59] Pacilio M, Cassano B, Pellegrini R, Di Castro E, Zorzi A, De Vincentis G et al., Gamma

camera calibrations for the italian multicentre study for lesion dosimetry in 223ra therapy of bone metastases. Phys Medica 41, 117–23, 2017.

[60] Merlin T, Stute S, Benoit D, Bert J, Carlier T, Comtat C, Filipovic M, Lamare F, Visvikis D, Castor: a generic data organization and processing code framework for multi-modal and multi-dimensional tomographic reconstruction. Phys Med Bio 63, 151–162, 2018.

[61] Frey EC, Tsui BMW, Collimator-Detector Response Compensation in SPECT. In: Zaidi H, editor. Quantitative Analysis in Nuclear Medicine Imaging. 1st ed. New York: Springer, p. 141–166, 2006.

[62] Jentzen W, Weise R, Kupferschläger J, Freudenberg L, Brandau W, Bares R et al., Iodine-124 PET dosimetry in differentiated thyroid cancer: recovery coefficient in 2D and 3D modes for PET(/CT) systems. Eur J Nucl Med Mol Imaging, 35:611–623, 2008.

[63] Toossi MTb, Islamian PJ, Momennezhad M, Ljungberg M, Naseri SH, SIMIND Monte Carlo simulation of a single photon emission CT. Journal of Medical Physics, 35(1):42–47, 2010.

[64] Ramonaheng K, van Staden JA, du Raan H, Validation of a Monte Carlo modelled gamma camera for Lutetium-177 imaging. Appl Radiat Isot, 163:109200, 2020.

[65] Morphis M, van Staden JA, du Raan H, Ljungberg M, Modelling of energy-dependent spectral resolution for SPECT Monte Carlo simulations using SIMIND. Heliyon, 7:e06097, 2021.

[**?**] Hakimabad HM, Panjeh H, Vejdani-Noghreiyan A, Nonlinear response function of a 3x3 in. NaI scintillation detector. Asian J Exp Sci, 21:233–237, 2007.

[66] Zhao W, Esquinas PL, Hou X, Uribe CF, Gonzalez M, Beauregard J, et al, Determination of gamma camera calibration factors for quantitation of therapeutic radioisotopes. EIJNMMI Physics, 5:1–16, 2018.

[67] Peters SMB, van der Werf NR, Segbergs M, van Velden FHP, Wierts R, Blokland KJAK et al., Towards standardization of absolute SPECT/CT quantification: a multi-center and multivendor phantom study. EJNMMI Physics, 6:1–14, 2019.

[68] Bodei L, Kidd M, Baum RP, Modlin IM. PRRT, Defining the paradigm shift to achieve standardization and individualization. J Nucl Med, 55(11):1753-6, 2014.

[69] Gupta SK, Singla S, Thakral P, Bal CS, Dosimetric analyses of kidneys, liver, spleen, pituitary gland, and neuroendocrine tumors of patients treated with 177Lu-DOTATATE. Clin Nucl Med, 38(3):188-94, 2013.

[70] Cremonesi M, Ferrari M, Bodei L et al., Dosimetry in Peptide radionuclide receptor therapy: a review. J Nucl Med, 47(9):1467-75, 2006.

[71] Sandström M, Garske-Román U, Granberg D et al., Individualized dosimetry of kidney and bone marrow in patients undergoing 177Lu-DOTA-octreotate treatment. J Nucl Med, 54(1):33-41, 2013.

[72] Del Prete M, Buteau FA, Beauregard JM, Personalized 177Lu-octreotate peptide receptor radionuclide therapy of neuroendocrine tumours: a simulation study. Eur J Nucl Med Mol Imaging, 44(9):1490-1500, 2017.

[73] Del Prete M, Buteau FA, Arsenault F et al, Personalized 177Lu-octreotate peptide receptor radionuclide therapy of neuroendocrine tumours: initial results from the P-PRRT trial. Eur J Nucl Med Mol Imaging, 46(3):728-742, 2019.

[74] European Council Directive 2013/59/Euratom on basic safety standards for protection against the dangers arising from exposure to ionising radiation and repealing Directives 89/618/Euratom, 90/641/Euratom, 96/29/Euratom, 97/43/Euratom and 2003/122/ Euratom. Official Journal of the European Union, L13:1–17, 2014.

[75] Wehrmann C, Senftleben S, Zachert C et al, Results of individual patient dosimetry in peptide receptor radionuclide therapy with 177Lu DOTA-TATE and 177Lu DOTA-NOC. Cancer Biother Radiopharm, 22(3):406-16, 2007.

[76] Svensson J, Berg G, Wängberg B et al, Renal function affects absorbed dose to the kidneys and haematological toxicity during 177Lu-DOTATATE treatment. Eur J Nucl Med Mol Imaging, 42(6):947-55, 2015.

[77] Guerriero F, Ferrari ME, Botta F et al., Kidney dosimetry in 177Lu and 90Y peptide receptor radionuclide therapy: influence of image timing, time-activity integration method, and risk factors. Biomed Res Int, 2013:935351, 2013.

[78] Ilan E, Sandström M, Wassberg C et al., Dose response of pancreatic neuroendocrine tumors treated with peptide receptor radionuclide therapy using 177Lu-DOTATATE. J

Nucl Med, 56(2):177-82, 2015.

[79] Bodei L, Cremonesi M, Ferrari M et al., Long-term evaluation of renal toxicity after peptide receptor radionuclide therapy with 90Y-DOTATOC and 177Lu-DOTATATE: the role of associated risk factors. Eur J Nucl Med Mol Imaging, 35(10):1847-56, 2008.

[80] Forrer F, Krenning EP, Kooij PP et al., Bone marrow dosimetry in peptide receptor radionuclide therapy with [177Lu-DOTA(0),Tyr(3)]octreotate. Eur J Nucl Med Mol Imaging, 36(7):1138-46, 2009.

[81] Shen S, Meredith RF, Duan J et al., Improved prediction of myelotoxicity using a patient-specific imaging dose estimate for non-marrow-targeting (90)Y-antibody therapy. J Nucl Med, 43(9):1245-53, 2002.

[82] Ferrer L, Kraeber-Bodéré F, Bodet-Milin C et al., Three methods assessing bone marrow dosimetry in lymphoma patients treated with radioimmunotherapy. Cancer, 116(4 Suppl):1093-100, 2010.

[83] Strigari L, Konijnenberg M, Chiesa C et al., The evidence base for the use of internal dosimetry in the clinical practice of molecular radiotherapy. Eur J Nucl Med Mol Imaging, 41:1976–1988, 2014.

[84] Siegel JA, Thomas SR, Stubbs JB et al., MIRD pamphlet no. 16: techniques for quantitative radiopharmaceutical biodistribution data acquisition and analysis for use in human radiation dose estimates. J Nucl Med, 37S-61S, 1999.

[85] Dewaraja YK, Frey EC, Sgouros G et al., MIRD pamphlet no. 23: quantitative SPECT for patient-specific 3-dimensional dosimetry in internal radionuclide therapy. J Nucl Med, 1310-1325, 2012.

[86] Ljungberg M, Celler A, Konijnenberg MW et al., MIRD pamphlet no. 26: joint EANM/MIRD guidelines for quantitative 177Lu SPECT applied for dosimetry of radiopharmaceutical therapy. J Nucl Med, 57(1):151–62, 2016.

[87] Stabin MG, Farmer A, OLINDA/EXM 2.0: The new generation dosimetry modeling code. J Nucl Med, 53 (supplement 1) 585, 2012.

[88] Feller PA, Sodd VJ, Kereiakes JG, Using the S tables of MIRD Pamphlet 11. J Nucl Med, 18:747, 1977.

[89] Baechler S, Hobbs RF, Prideaux AR et al., Extension of the biological effective dose to the MIRD schema and possible implications in radionuclide therapy dosimetry. Med. Phys, 35:1123-1134, 2008.

[90] Kairemo K, Kangasmäki A, 4D SPECT/CT acquisition for 3D dose calculation and dose planning in (177)Lu-peptide receptor radionuclide therapy: applications for clinical routine. Recent Results Cancer Res, 194:537-50, 2013.

[91] Marin G, Vanderlinden B, Karfis I et al., A dosimetry procedure for organs-at-risk in 177Lu peptide receptor radionuclide therapy of patients with neuroendocrine tumours. Phys Med, 56:41-49, 2018.

[92] Santoro L, Mora-Ramirez E, Trauchessec D, Chouaf S, Eustache P, Pouget JP, Kotzki PO, Bardiès M, Deshayes E, Implementation of patient dosimetry in the clinical practice after targeted radiotherapy using [177Lu-[DOTA0, Tyr3]-octreotate. EJNMMI Res, 8:103, 2018.

[93] Agostinelli S et al, GEANT4 - a simulation toolkit, Nuclear Instruments and Methods in Physics Research A, vol. 506, no. 3, pp. 250–303, 2003.

[94] Rowedder B, Kuang Y, GATE Monte Carlo Simulation in a Cloud Computing Environment. Medical Physics. 40. 206, 2013.

[95] Menzel HG, Clement C, DeLuca P, ICRP Publication 110. Realistic reference phantoms: an ICRP/ICRU joint effort. A report of adult reference computational phantoms. Ann ICRP, 39(2):1-164, Erratum 165, 2009.

[96] ICRP 2008 Nuclear Decay for Dosimetric Calculations, ICRP Publication vol 107, Oxford: Elsevier, 2008.

[97] Hadid L, Desbrée A, Schlattl H, Franck D, Blanchardon E, Zankl M, Application of the ICRP/ICRU reference computational phantoms to internal dosimetry: calculation of specific absorbed fractions of energy for photons and electrons Phys. Med. Biol. 55 3631–41, 2010.

[98] Villoing D, Marcatili S, Garcia MP, Bardiès M, Internal dosimetry with the Monte Carlo code GATE: validation using the ICRP/ICRU female reference computational model. Phys Med Biol 62:1885 –1904, 2017.

[99] Chauvin M, Borys D, Botta F, Bzowski P, Dabin J, Denis-Bacelar AM et al., OpenDose: Open-Access Resource for Nuclear Medicine Dosimetry. J Nucl Med 61(10), 1514 - 1519, 2020.

[100] Stabin MG, Siegel JA. Physical models and dose factors for use in internal dose assessment. Health Phys., 85(3):294-310, 2003.

[101] Fedorov A, Beichel R, Kalpathy-Cramer J, Finet J, Fillion-Robin JC, Pujol S et al., 3D Slicer as an Image Computing Platform for the Quantitative Imaging Network. Magnetic Resonance Imaging, 30(9):1323-41, 2012.

[102] Dieudonné A, Hobbs RF, Bolch WE, Sgouros G, Gardin I, Fine-resolution voxel S values for constructing absorbed dose distributions at variable voxel size. Journal of Nuclear Medicine, 51(10), 1600-1607, 2010.

[103] International Commission on Radiation Units and Measurements. Photon, Electron, Proton and Neutron Interaction Data for Body Tissues. Report 46. Bethesda, MD: ICRU, 1992.

[104] Reynaert N, Palmans H, Thierens H, Jeraj R, Parameter dependence of the MCNP electron transport in determining dose distributions. Med Phys, 29:2446–2454, 2002.

[105] Eckerman KF, Endo A, MIRD: Radionuclide Data and Decay Scheme. 2nd ed. Reston, VA: The Society of Nuclear Medicine, 2008.

[106] Lanconelli N, Pacilio M, Lo Meo S et al., A free database of radionuclide voxel S values for the dosimetry of nonuniform activity distributions. Physics in Medicine and Biology, 57:517-533, 2012.

[107] Werner CJ, MCNP Users Manual - Code Version 6.2. Los Alamos National Laboratory, report LA-UR-17-29981, 2017.